

Variability in wave impacts
An experimental investigation

van Meerkerk, M.

DOI

[10.4233/uuid:5a09d025-9980-44de-b01f-dd09bbc36354](https://doi.org/10.4233/uuid:5a09d025-9980-44de-b01f-dd09bbc36354)

Publication date

2021

Document Version

Final published version

Citation (APA)

van Meerkerk, M. (2021). *Variability in wave impacts: An experimental investigation*. [Dissertation (TU Delft), Delft University of Technology]. <https://doi.org/10.4233/uuid:5a09d025-9980-44de-b01f-dd09bbc36354>

Important note

To cite this publication, please use the final published version (if applicable).
Please check the document version above.

Copyright

Other than for strictly personal use, it is not permitted to download, forward or distribute the text or part of it, without the consent of the author(s) and/or copyright holder(s), unless the work is under an open content license such as Creative Commons.

Takedown policy

Please contact us and provide details if you believe this document breaches copyrights.
We will remove access to the work immediately and investigate your claim.

The background features a stylized illustration of ocean waves in shades of blue and grey. A small boat is visible in the distance, and a large, faint outline of a structure, possibly a ship's hull or a wave impact zone, is positioned in the upper left. The overall aesthetic is clean and technical.

VARIABILITY IN WAVE IMPACTS

AN EXPERIMENTAL INVESTIGATION

MIKE VAN MEERKERK

VARIABILITY IN WAVE IMPACTS

MIKE VAN MEERKERK

VARIABILITY IN WAVE IMPACTS

An Experimental Investigation

PROEFSCHRIFT

ter verkrijging van de graad van doctor
aan de Technische Universiteit Delft,
op gezag van de Rector Magnificus Prof.dr.ir. T.H.J.J. van der Hagen,
voorzitter van het College voor Promoties,
in het openbaar te verdedigen op donderdag 24 juni 2021 om 12:30 uur

door

Mike VAN MEERKERK
Werktuigkundig ingenieur
Technische Universiteit Delft, Delft, Nederland
geboren te Den Haag, Nederland.

Dit proefschrift is goedgekeurd door de promotoren.

Samenstelling promotiecommissie:

Rector Magnificus,	Voorzitter
Prof.dr.ir. C. Poelma,	Technische Universiteit Delft, promotor
Prof.dr.ir. J. Westerweel,	Technische Universiteit Delft, promotor

Onafhankelijke leden:

Prof.dr. F. Dias,	University College Dublin, Ireland
Prof.dr. R.M. van der Meer,	Universiteit Twente
Prof.dr.ir N.G. Deen,	Technische Universiteit Eindhoven
Prof.dr.ir. W.S.J. Uijtewaai,	Technische Universiteit Delft
Prof.dr.ir. S. Kenjereš,	Technische Universiteit Delft

This research is supported by the Netherlands Organisation for Scientific Research (NWO) Domain Applied and Engineering Sciences in the public-private research program Slicing of Liquefied Natural Gas (SLING) in the project *Variability* with project number 14909 P14-10 - project 2.



Cover design by: Luka van Dien

Printed by: GildePrint - Enschede

Copyright © 2021 by M. van Meerkerk, all rights reserved
ISBN 978-94-6384-226-6

An electronic version of this dissertation is available at
<http://repository.tudelft.nl/>.

CONTENTS

1	INTRODUCTION	1
1.1	Background	2
1.2	Wave impacts	3
1.2.1	Wave impact classification	4
1.2.2	Scaling of wave impacts	5
1.2.3	Instabilities in sloshing	6
1.3	SLING project	7
1.3.1	The atmosphere	8
1.4	Objectives and scope of the research	9
1.5	Outline of the thesis	9
2	SCANNING STEREO-PLIF METHOD FOR FREE SURFACE MEASUREMENTS IN LARGE 3D DOMAINS	13
2.1	Introduction	14
2.2	Method	17
2.2.1	Flow Facility	17
2.2.2	Reference Measurement	18
2.2.3	Stereo-PLIF Measurement	19
2.2.4	Edge Detection Procedure	20
2.2.5	Stereo-PLIF Calibration	20
2.2.6	Post-processing	23
2.2.7	Calibration Accuracy	24
2.3	Results and Discussion	26
2.3.1	Hydraulic Flow	26
2.3.2	Wave Swell by Water Drop Impact	30
2.4	Conclusion	35
3	EXPERIMENTAL INVESTIGATION OF WAVE TIP VARIABILITY OF IMPACTING WAVES	37
3.1	Introduction	38
3.2	Experimental approach	41
3.2.1	Wave flume	41
3.2.2	Wave generation	42
3.2.3	Free surface profile measurement	43
3.2.4	Experimental procedure	46
3.3	Results and discussion	47
3.3.1	System variability	47
3.3.2	Global wave behavior	49
3.3.3	Local wave behavior	55
3.4	Conclusion	64

4	GAS FLOW DYNAMICS OVER A PLUNGING BREAKING WAVE PRIOR TO IMPACT ON A VERTICAL WALL	67
4.1	Introduction	68
4.2	Experimental approach	70
4.2.1	Wave flume	70
4.2.2	Experimental methods	72
4.3	Results and discussion	74
4.3.1	Global gas flow	74
4.3.2	Local gas flow	75
4.3.3	Dynamics of the circulation zone	80
4.4	Conclusion	88
5	CONCLUSIONS AND PERSPECTIVES	91
5.1	Conclusions	92
5.2	Perspectives on future research	96
A	QUANTIFICATION OF SURFACE TENSION	101
B	INTERFEROMETRIC PARTICLE IMAGING	103
C	SYMMETRIC PHASE ONLY FILTERING	105
	REFERENCES	107
	ACKNOWLEDGEMENTS	115
	CURRICULUM VITAE	118
	LIST OF PUBLICATIONS	119

SUMMARY

The prospect of stricter national and international emission standards for the shipping industry are a driving force in the search for alternative shipping fuels, such as liquefied natural gas (LNG). However, new challenges arise with the widespread use of LNG. For example, there is a desire to use LNG cargo containment systems at lower filling levels. These filling levels are strictly limited to prevent the movement of liquid inside the containment system, which is known as sloshing. Sloshing inside a cargo containment system can result in extreme wave impact events with the potential to cause structural damage. Therefore, a fundamental understanding of these extreme wave impact events is required before studying increasingly complex phenomena.

The study of wave impacts on a wall has been an active area of research for decades. Moreover, the impact of waves upon structures is relevant for many fields such as ocean, coastal, and maritime engineering. The generation of repeatable waves in a laboratory environment is not trivial (Bagnold, 1939). Small changes in the experimental conditions, such as the water depth and the wave generation method, result in significant impact pressure variability. The impact pressure variability is even observed in carefully repeated wave impact experiments with minimal variability of the input parameters. For these measurements, the source of the impact pressure variability is thought to be the instability development on the wave crest. However, the mechanism that is responsible for the formation of these instabilities is still largely unknown.

The aim of this work is to gain insight in the sources of wave impact pressure variability. This is accomplished using direct measurements of the liquid free surface and particle image velocimetry of the surrounding air. The measurements are limited to a single wave (i.e., with a fixed steering signal and water depth) at atmospheric conditions, because of the complexity of the experimental measurements. A plunging breaking wave with a large gas pocket is generated that impacts on a vertical wall. The compression of the large gas pocket induces a significant gas flow between the wave crest and the vertical impact wall, which results in the formation of instabilities on the wave crest.

Quantitative measurements of the liquid free surface are obtained with an extension of the planar laser induced fluorescence (PLIF) method. The newly developed scanning stereo-PLIF measurement technique uses a stereo-camera set-up with a self-calibration procedure adapted for free surface flows. Thereby, the stereo-PLIF technique enables measurements of a free surface over a two-dimensional domain (e.g., $y = f(x, z, t)$). The system is versatile with a minimal

influence on the fluid properties and the measurement domain can be scaled as needed.

A repeatable plunging breaking wave is created in the wave flume of the Hydraulic Engineering Laboratory at the Delft University of Technology. The wave encloses a gas pocket as it approaches the vertical impact wall. Initially, the plunging breaking wave is globally comparable to waves that do not impact on a vertical wall. The aspect ratio of the cross-sectional area of the gas pocket remains relatively constant at $R_x/R_y = 1.6$ ($\sim \sqrt{3}$). Furthermore, the wave velocity ($\sqrt{gh_0}$) and wave tip velocity ($1.2\sqrt{gh_0}$) are initially similar to that of a plunging breaking wave. On the other hand, the trajectory of the wave tip is altered compared to that of a typical plunging breaking wave.

The trajectory of the wave tip is globally similar over repeated wave impact measurements. However, moments before impact the wave tip is deflected by the gas expelled from the gas pocket. The deflection of the wave tip introduces significant variation between the repeated measurements. On close inspection, the wave tip resembles a liquid sheet, that is destabilized by an initial Kelvin-Helmholtz instability (Villermaux et al., 2002). The flapping liquid sheet accelerates the wave tip, which triggers the development of a Rayleigh-Taylor instability. This results in approximately equally spaced liquid filaments (i.e., liquid fingers) over the spanwise direction of the wave. The spanwise wavelength depends on the density ratio (ρ_a/ρ_l) and surface tension, which was previously shown to be a source of wave impact pressure variability.

Additionally, particle image velocimetry measurements are performed to determine the interaction between the liquid and gas during a wave impact event. The global gas flow is similar to that of a plunging breaking wave, where a vortex develops on the leeward side of the wave. The vortex consistently separates from the breaking wave and lingers at the back of the breaking wave in the stagnant air. The development of circulation is typical for a vortex that eventually separates at a universal time scale denoted by the formation number (Gharib et al., 1998). However, a typical formation number can not be defined in this particular case, due to the simultaneous change of both the length and velocity scales.

The velocity profile between the wave tip and the vertical impact wall resembles that of a flow past a bluff body. A fit of the measured velocity profile agrees well with the velocity derived from mass conservation. Interestingly, the velocity close to the wave tip is approximately 2 times higher than the bulk velocity estimate. The high velocity close to the wave tip can thus result in an earlier onset of instability development compared to estimates based on the bulk velocity. Furthermore, the flow tends to separate close to the tip just before impact on the vertical wall. The effect of this flow separation on the impact pressure variability depends on the global wave shape prior to impact. For the case with a disturbance on the wave crest, the secondary vortex that forms close to the wave tip tends to break up. On the other hand, if the wave crest is smooth the secondary vortex remains attached. The attached secondary vortex increases the lift on the wave tip, which results in a significant deflection of the wave tip. Consequently, the development of secondary

vortices close to the wave tip results in wave impact pressure variability, as the typical deflection is larger than the membrane diameter of a contemporary pressure transducer.

Local phenomena such as flow separation and the development of instabilities define the variability of the peak pressure during wave impacts. On the other hand, the global characteristics of an air-water wave impact on a vertical wall can be retrieved with pressure impulse models (Cooker et al., 1995). The maximum wave impact pressure is relevant for LNG containments systems and wave energy converters. Consequently, numerical models that aim to quantify wave impact pressure variability require accurate models of both the gas phase and the development of free surface instabilities.

SAMENVATTING

Het vooruitzicht op strengere (inter)nationale emissienormen maakt het nodig om te zoeken naar alternatieve brandstoffen voor de scheepvaart, waaronder vloeibaar aardgas (LNG). Het in gebruik nemen van LNG is echter praktisch uitdagend: op dit moment kunnen LNG bunkerschepen alleen vrijwel vol of vrijwel leeg varen. Deze vullingsgraden zijn sterk gereguleerd om de beweging van vloeistof, ook wel bekend als klotsen (sloshing), binnenin de bunkerschepen te voorkomen. Dit klotsen kan structurele schade veroorzaken door het ontstaan van brekende golven die met een enorme kracht inslaan op de wanden van de bunker. Het is dus van belang om de inslag van brekende golven beter te begrijpen om zo steeds complexere situaties, zoals het klotsen van LNG, te kunnen beschrijven.

Het inslaan van golven op verticale wanden wordt al decennialang bestudeerd. Het speelt namelijk een rol in veel vakgebieden, zoals kustbouw, waterbouw en maritieme techniek. Het onderzoek wordt echter gecompliceerd door de problemen die ontstaan bij het creëren van herhaalbare golven in een laboratoriumomgeving (Bagnold, 1939). De druk die de golf uitoefent op de verticale wand wordt sterk beïnvloed door kleine verandering in de omstandigheden, zoals de waterdiepte en de methode voor het genereren van de golven. Daarnaast verschilt de druk ook als er nauwelijks verschillen zijn in de omstandigheden. In dit geval wordt de variatie van de inslagdruk toegeschreven aan de instabiliteit ontwikkeling op de kruin van de golf. Echter, het mechanisme dat resulteert in de ontwikkeling van instabiliteit op de kruin van een golf is nog steeds onbekend.

Dit onderzoek is opgezet om de mechanismes die verantwoordelijk zijn voor de variatie in inslagdruk in kaart te brengen. Het wateroppervlak en de stroming in de lucht zijn met experimentele methodes onderzocht. In dit onderzoek wordt vanwege de complexiteit van de experimentele meettechniek een golf beschreven die is verkregen op één enkele waterdiepte, met één methode voor het genereren van de golf onder normale atmosferische condities.

Het wateroppervlak is in kaart gebracht met een kwantitatieve methode die is gebaseerd op *planar laser induced fluorescence (PLIF)*. Deze nieuw ontwikkelde, kwantitatieve methode met de naam *scanning stereo-PLIF* maakt gebruik van een stereocamerasysteem en een speciaal ontwikkelde kalibratiemethode voor wateroppervlaktes. Hierdoor maakt het systeem metingen over een tweedimensionaal domein, zoals beschreven door $y = f(x, z, t)$ mogelijk. Het systeem is breed inzetbaar en het tweedimensionale meetgebied is makkelijk te wijzigen, daarnaast beïnvloedt de gebruikte fluorescente verf de eigenschappen van de vloeistof nauwelijks.

In de golfgoot van het *Hydraulic Engineering Laboratory* bij de technische universiteit in Delft is een herhaalbare brekende golf gegeneerd. De brekende golf omsluit een luchtzak voordat deze inslaat op de verticale wand. Op een globaal niveau is de brekende golf vergelijkbaar met een golf die niet inslaat op een verticale wand. Zo blijft de verhouding tussen de assen van de ellips die de doorsnede van de luchtzak omschrijft ongeveer constant met een waarde van $R_x/R_y = 1.6$ ($\sim \sqrt{3}$). Daarnaast zijn de snelheid van de golf ($\sqrt{gh_0}$) en de tip van de golf ($1.2\sqrt{gh_0}$) ongeveer gelijk aan die van een golf die niet inslaat op een verticale wand. Het pad van de golftip verschilt daarentegen van een typische golf die niet inslaat op een verticale wand.

Het pad van de golftip is op een globaal niveau vergelijkbaar over herhaalde experimenten. Op het laatste moment voordat de golf inslaat op de verticale wand wordt de tip van de golf weggeblazen door het gas dat uit de luchtzak stroomt. Hierdoor ontstaan significante verschillen in het punt waarop de golf inslaat over herhaalde metingen. Het lokale verschil ontstaat doordat de golftip op het laatste moment lijkt op een dun vloeistofvel, dat wordt verstoord door een eerste Kelvin-Helmholtz instabiliteit (Villermaux et al., 2002). Het klapperen van dit vloeistofvel zorgt ervoor dat de golftip lokaal wordt versneld, waardoor zich een nieuwe Rayleigh-Taylor instabiliteit ontwikkelt. Hierdoor ontstaan over de breedte van de golf op een ongeveer gelijke afstand vloeistoffilamenten, ofwel vloeistofvingers. De afstand tussen de vingers (de golflengte) is afhankelijk van de dichtheidsratio van het gas en de vloeistof (ρ_a/ρ_l) en van de oppervlaktespanning. De afhankelijkheid van deze parameters was al bekend uit eerder kwalitatief onderzoek, maar dit onderzoek geeft een eerste indicatie van de afhankelijkheid van de vingerafstand van deze parameters.

Naast de oppervlaktemetingen is ook *particle image velocimetry* toegepast om de koppeling tussen het gas en de vloeistof te onderzoeken voordat de golf inslaat op de verticale wand. Op een globaal niveau is de stroming van het gas vergelijkbaar met de gasstroom over een brekende golf die niet inslaat op een verticale wand: er ontstaat een vortex aan de achterkant van de golf. Deze vortex komt consistent los van de golfkruin waarna hij in de stilstaande lucht achter de golf blijft hangen. De ontwikkeling van de circulatie is typisch voor een vortex die uiteindelijk scheidt van de structuur waaraan hij bevestigd is op een universele tijdschaal. Deze tijdschaal is ook wel bekend als het formatiegetal (Gharib et al., 1998). Voor de inslaande golf kan helaas geen eenduidig formatiegetal worden bepaald, doordat zowel de tijd- als lengteschaal op hetzelfde moment veranderen.

Tussen de tip van de golf en de verticale wand ontstaat een stroming waarvan het snelheidsprofiel lijkt op dat van een stroming om een stomp voorwerp. De experimenteel bepaalde gemiddelde snelheid tussen de tip van de golf en de verticale wand is vergelijkbaar met de theoretisch bepaalde snelheid op basis van massabehoud, indien de gemiddelde snelheid van de experimentele meting wordt bepaald op basis van een trendlijn van het snelheidsprofiel. Het is interessant dat de snelheid dichtbij de tip van de golf ongeveer twee keer zo groot is als de theoretisch bepaalde gemiddelde snelheid op basis van massabehoud. Door de hoge snelheid dichtbij de golftip kan het golfoppervlak eerder instabiel worden dan op basis van

massabehoud zou worden verwacht. Naast dat de snelheid van het gas hoger is, ontstaat er ook een lokale werveling aan de tip van de golf voordat de golf inslaat op de verticale wand. Het effect van deze werveling op de variabiliteit is afhankelijk van de golfvorm. Indien er een typische verstoring op het golfoppervlak aanwezig is, scheidt de werveling eerder van de golftip en wordt er een grenslaag gevormd over de tip van de golf. Indien er geen verstoring aanwezig is op het golfoppervlak, blijft de werveling langer aan tip bevestigd. De werveling bij de tip van de golf resulteert in een verhoging van de liftkracht en daardoor een grotere afbuiging van de golftip. Er kan geconcludeerd worden dat het ontstaan van lokale wervelingen aan de golftip resulteert in de variabiliteit van de druk die wordt gemeten bij het inslaan van een golf op een verticale wand, omdat de afbuiging van de golftip groter is dan de diameter van het membraan in een typische druksensor.

De variabiliteit van de druk tijdens het inslaan van herhaalbare golven op een verticale wand wordt veroorzaakt door lokale effecten nabij de tip van een golf, zoals de wervelingen en de instabiliteit van het golfoppervlak. Daartegenover staat dat het globale drukprofiel door de inslag van een watergolf omringd door lucht kan worden bepaald met behulp van drukimpulsmodellen (Cooker et al., 1995). De maximale druk die optreedt tijdens het inslaan van een golf is van belang voor LNG bunkersystemen en apparaten die energie halen uit de beweging van golven. Het is van belang dat modellen die worden gebruikt om de variabiliteit van een golfinslag te bepalen beschikken over een nauwkeurige implementatie van zowel gedrag van het gas als de ontwikkeling van een instabiel golfoppervlak.

1

INTRODUCTION

Parts of this chapter were published in M. van Meerkerk, C. Poelma, B. Hofland, and J. Westerweel, "Experimental investigation of wave tip variability of impacting waves", *Physics of Fluids*, 32,082110, 2020

1.1 BACKGROUND

Imagine having a pleasant day at the beach and you decide to create a sand castle in the surf zone. Of course, everyone knows what happens when the tide rises. The sea creates relatively small waves that impact your castle, but even these small waves exert a tremendous amount of force on the walls of your castle. Eventually, your castle will be destroyed by the ocean, but you had your fun with it and you continue to enjoy your day at the beach. However, the impact of waves on structures can not be neglected in daily life.

The study of wave impacts on walls has been an active area of research for decades (Bagnold, 1939; Hattori et al., 1994; Blackmore et al., 1984; Bullock et al., 2001; Cuomo et al., 2010; Wang et al., 2018). The impact of waves is relevant for coastal structures, dunes, and sandy beaches exposed to the ocean (Buchner et al., 2007). Ships, especially high-speed crafts, experience wave impacts from both the approaching waves and through *slamming* (Dias et al., 2018) (fig. 1.1 a). Wave impacts can also occur inside a moving container that is not completely filled with a fluid (i.e. that has a free surface). The movement of fluid inside a container is called *sloshing* (Faltinsen et al., 2009). The effect of sloshing is relevant for space applications (see figure 1.1 b) and during the transport of liquids, such as liquefied natural gas (LNG) in cargo containment systems.

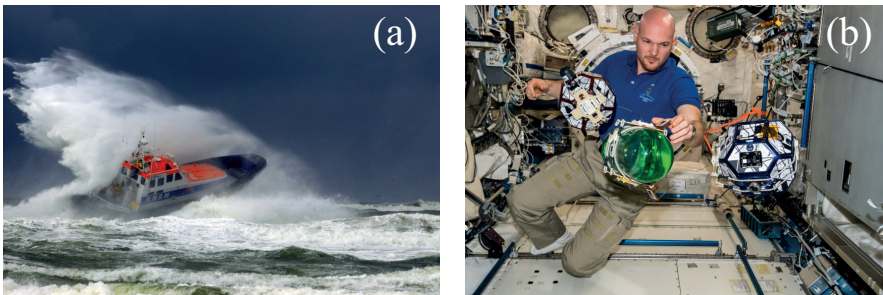


Figure 1.1: Typical examples of free surface waves interacting with structures. (a) A slamming wave that interacts with both the hull and the deck of a KNRM lifeboat (KNRM, 2019). (b) Sloshing in partially filled fuel tanks aboard the international space station during the *thether slosh* project (ESA, 2020).

The use of LNG is expected to increase in the coming years driven by the abundant supply and the need for a transition fuel (International Gas Union, 2020). In the coming year the global gas market is expected to decrease by 4% due to the Covid-19 pandemic. Nonetheless, the use of gas for industrial purposes is still expected to grow with 2.5% per year up to 2025 (International Energy Agency, 2020). The maritime industry contributes significantly to the increased use of LNG as a transport fuel. Stricter national and international emission standards for the shipping industry necessitate a transition to lower emission fuels such as LNG.

The widespread use of LNG as both a transport fuel and in industrial processes, requires an improved infrastructure to accommodate large as well as small scale solutions. Improving the LNG infrastructure leads to new challenges, such as a growth in bulk capacity of the cargo containment systems (CCSs), increased exposure of CCSs to extreme weather conditions, and the desire to use CCSs at lower filling levels (Delorme et al., 2009). However, the filling levels of typical bulk carriers are strictly limited to reduce the risk of sloshing damage. On the other hand, there is a market desire to use lower filling levels and to use altered containment system designs.

Containment system design changes can result in both lower investment costs and reduced operational costs. However, new designs are currently limited by the sloshing assessment methodology (Gavory et al., 2009). The assessment methodology is based on long-term statistics of pressure peaks collected in model tests. These results are scaled to physical dimensions with a calibration function based on historical data. The calibration function is required, as the basic physical processes involved during sloshing of LNG are not well understood. For example, the physical mechanism that results in wave impact pressure variability during wave impact measurements is not yet known, while wave impact events are at the basis of the extreme loads observed in sloshing tests. Therefore, it is essential to study the sources of variability that arise during wave impact events in well-controlled environments before studying increasingly complex phenomena such as sloshing of LNG.

In the remainder of this chapter previous work on wave impacts will be discussed, and the result of recent studies on sloshing will be introduced. Several concepts, such as *global and local flow* and *elementary loading processes* will be thoroughly reviewed. Finally, the chapter is concluded with the research objective and an outline of this thesis.

1.2 WAVE IMPACTS

The consistent interest in wave impacts on structures has resulted in numerous review articles. Recently, the effect of liquid sloshing has been thoroughly reviewed by Ibrahim (2020). A broad overview of both slamming and wave impacts on structures in the context of sloshing is presented by Dias et al. (2018). The impact of waves on vertical structures has been reviewed by Peregrine (2003). Especially the impact of waves on structures is relevant in numerous applications spanning almost all engineering domains (fig. 1.1). However, the study of wave impacts in laboratory environments is not trivial.

Bagnold (1939) showed that even in carefully controlled experiments significant variation exist in the peak pressure of a wave impact. A main source of variability is the limited control of the parameters that influence the wave generation, among which are the water depth, the wave generation method, and the surrounding environment (Hofland et al., 2010; Kimmoun et al., 2010). In large-scale outdoor experiments even the weather conditions can result in variability of the peak impact

pressure (Hofland et al., 2010). Among others, Bagnold (1939) showed that the integral of the impact pressure over time (e.g., the pressure impulse) is repeatable. The impulse is easily converted to a net force exerted on a structure, and is often far more important than the extreme loads. For example, the hull design of high-speed vessels in slamming conditions is based on the net force exerted by the pressure impulse (Dias et al., 2018). The impact pressure of a wave is also often modeled and scaled with pressure impulse theory (Cooker et al., 1995). However, the peak impact pressure remains an important design parameter in specific applications, such as sloshing in LNG containment systems (Y. K. Song et al., 2013; Bogaert et al., 2010; Lafeber et al., 2012a) and slamming of wave energy converters (Y. Wei et al., 2016; Henry et al., 2015).

In the remainder of this section concepts that are relevant for sloshing experiments are introduced. First, the wave types that are observed during sloshing experiments are introduced. The effect of each wave type on the structure is subdivided in so-called elementary loading processes. Thereafter, the details of wave impact experiments in the context of sloshing are introduced. Here topics such as scaling and the development of free surface instabilities are discussed.

1.2.1 WAVE IMPACT CLASSIFICATION

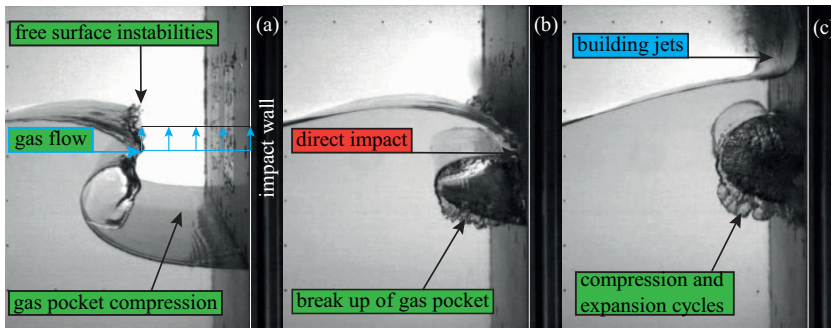


Figure 1.2: Typical example of the development of a gas-pocket wave impact with a plunging breaker (Adapted from Bogaert, 2018, and used with permission). The elementary loading processes (ELP's) easily identify development of the wave impact (Lafeber et al., 2012b).

The impact pressure is directly related to the shape of the wave prior to impact, which requires a classification of wave shapes. Four wave impact types can be identified based on both the shape and the behavior of the wave prior to impact. They are a slosh, a flip-through, a gas-pocket, and an aerated wave impact (Hull et al., 2002; Chan et al., 1988; Hattori et al., 1994). The gas-pocket impact is often further subdivided in two classes based on either having a gas pocket with a relatively large or small cross-sectional area (Faltinsen et al., 2009; Hattori et al., 1994). The gas pocket cross-sectional area determines the oscillation frequency after impact, which

is either low or high for a gas pocket with a respectively large or small cross-sectional area (Hattori et al., 1994). The wave shape prior to impact is a good predictor of the peak impact pressure. However, the classification boundaries are not precisely defined and a more detailed description is required.

Several stages can be identified during a wave impact event. An example of a typical gas-pocket impact with a plunging breaker is shown in figure 1.2. The plunging breaker approaches the vertical impact wall, while the gas pocket cross-sectional area reduces (fig.1.2a). The reduction of the gas pocket volume occurs simply through the air escaping. Numerical simulations of the escaping air, among which are those of Guilcher et al. (2018) and Behruzi et al. (2017), indicate that compressibility eventually becomes important for different gas compositions and length scales (i.e., wave height and water depth). The escaping air exerts a shear force on the free surface of the wave crest, which triggers the development of instabilities on the wave crest surface (Dias et al., 2018).

The peak impact pressure is the result of the direct impact of the wave on the vertical wall (fig. 1.2b). In this case, the deceleration of the liquid surrounding the gas pocket results in the formation of Rayleigh-Taylor instabilities. The horizontal momentum of the wave is deflected by the impact wall, which results in the formation of two building jets (e.g., the upwards and downwards directed liquid filaments). The gas pocket volume *after* impact has been studied in detail (Abrahamsen et al., 2011; Lugni et al., 2010b; Lugni et al., 2010a). The enclosed gas pocket compresses and expands with a frequency that depends on the initial breaker shape (Hattori et al., 1994; Abrahamsen et al., 2011). The different impact stages can be subdivided into elementary loading processes (ELP's) and are, for a typical gas pocket impact, shown in figure 1.3 (Lafeber et al., 2012a). The ELP's are defined as *direct impact* (ELP₁), *building jet* (ELP₂), and *compressed gas* (ELP₃). Different combinations of ELPs result in specific wave impact types (Lafeber et al., 2012a). Furthermore, the ELPs identify physical phenomena that occur during each stage of a wave impact.

1.2.2 SCALING OF WAVE IMPACTS

A wave that approaches a wall is a time dependent physical phenomena that spans several length scales. Therefore, the development of the wave in sloshing and wave impact experiments is divided into a *global* and *local flow* (Bogaert et al., 2010). The *global flow* determines the wave profile prior to impact, and as such the elementary loading processes involved (fig. 1.3). The *local flow* defines the details of the wave that are changed by the presence of an impact wall.

The *global* flow is often described using the incompressible Euler equations in both phases. Consequently, the global flow is inviscid and incompressible, whereas the *local* flow is influenced, among others, by viscosity and compressibility. The Euler equations rewritten in their non-dimensional form are often used to identify the relevant scaling parameters for sloshing experiments. This results in Froude scaled sloshing experiments, which additionally require the density ratio (DR) of the liquid

and gas to be consistent. However, Karimi et al. (2015) showed that the *global* flow is almost independent of both the scale and the density ratio (DR).

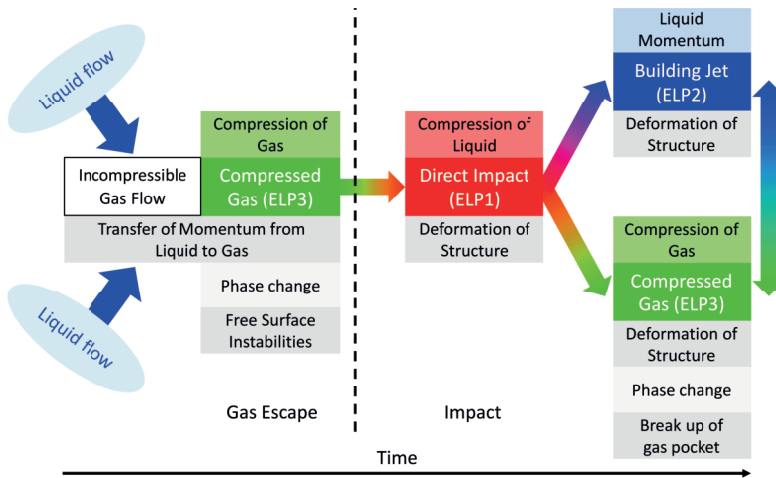


Figure 1.3: Schematic representation of the elementary loading processes (ELP's) involved in wave impact experiments (Adapted from Bogaert, 2018, and used with permission). The ELP's identify physical phenomena that occur in each elementary loading process, such as phase transition for fluids that are close to the phase boundary and the development of free surface instabilities Lafeber et al. (2012b).

On the other hand, the *local* flow and the scaling are not well understood, as viscosity, surface tension, and compressibility become relevant prior to impact. Additionally, phase change and the aeration of the liquid are also important prior to impact (Bullock et al., 2001; Bredmose et al., 2015; Bullock et al., 2007; Yung et al., 2010). In practice, wave impact experiments are often not performed with full similarity, as experiments are often conducted with water and air at atmospheric conditions (Bogaert, 2018). Lack of similarity between scaled experiments results in local flow differences. These differences complicate comparison between scaled experiments, which is especially relevant for sloshing of LNG. Additionally, the formation and development of instabilities is postulated to be the main source wave impact pressure variability (Lubin et al., 2019; Dias et al., 2018; M. Frihat et al., 2016).

1.2.3 INSTABILITIES IN SLOSHING

The peak impact pressure of repeated wave impact experiments varies significantly. The variability is attributed to the development of instabilities on the wave crest (Dias et al., 2018; M. Frihat et al., 2016). For example, the development of instabilities during repeated wave impact experiments is shown in figure 1.4. The global wave is almost identical during repeated measurements, whereas significant variations are visible over the spanwise direction of the wave crest. The source of these instabilities

and their formation mechanism are still largely unknown (Lubin et al., 2019). In the case of a gas-pocket type impact a strong gas flow is forced over the wave crest, which results in a shear force on the wave crest. The instability development is, therefore, suggested to be initiated by a Kelvin-Helmholtz type instability (Karimi et al., 2015; Lubin et al., 2019; Fortin et al., 2020; M. Frihat et al., 2016).

Sloshing and wave impact experiments have been conducted at different length scales to determine the effect of instability development on the variability of the peak impact pressure. The physical properties of both the liquid and gas, such as the surface tension (L. Frihat M. B. et al., 2017), viscosity, density ratio (Karimi et al., 2015), have also been varied. However, the reported measurements are often based on qualitative pressure measurements or quantitative side view measurements. These side view measurements can be obstructed by the presence of liquid filaments, such as those shown in figure 1.4. Therefore, there is a need to determine the variability and formation of instabilities with a quantitative measurement technique.

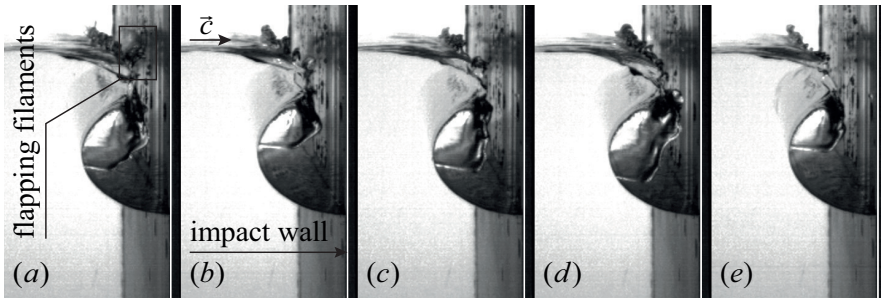


Figure 1.4: Typical example of the impact of several (a-e) repeatable focused waves obtained in the SLOSHEL project (Adapted from Bogaert, 2018, and used with permission). The wave approaches the impact wall from left to right (i.e., with a velocity denoted by \vec{c}). The images are recorded prior to impact on a vertical wall. The span-wise distribution and growth of the free surface instabilities on the wave crest is significantly different between repetitions. For example, flapping liquid filaments are observed in the box of panel (a), whereas these are almost absent in panel (e).

1.3 SLING PROJECT

This research was performed as part of the NWO-TTW Perspectief public-private research program SLING (i.e., “Sloshing of Liquefied Natural Gas”). The primary aim of the program is to provide a first-principle approach that disentangles the physical problems that occur during sloshing of LNG in containment systems. The project aims to enable technological development in the complete LNG infrastructure with crucial cost saving potential.

The physical problems of sloshing in LNG are subdivided in three thematic projects: *multiphase dynamics*, *variability of impact loads*, and *structural response*. Additionally, an overarching project (i.e., *sloshing assessment*) is defined that ensures

an integral approach between the three thematic projects. The project consists of seven individual Ph.D. projects, two PDEng positions, and one overarching PostDoc position. The physics of sloshing are disentangled with a combination of numerical and experimental work. A next step in sloshing research requires experimental work with working fluids other than air and water at atmospheric conditions. The final project in the SLING program is, therefore, the construction of a new multiphase test facility.

1.3.1 THE ATMOSPHERE

The *Atmosphere* is a new multiphase test facility that has been constructed at the Maritime Research Institute Netherlands (MARIN) to facilitate the SLING project. Figure 1.5 presents a schematic of the autoclave that can house several experiments, such as a wave flume. The environmental conditions are controlled within a temperature range of $15 \leq T \leq 200$ °C and a pressure of $5 \text{ mbar} \leq p \leq 10$ bar. The gas condition and composition can be controlled with a gas system. The gas can be composed of water vapor, nitrogen, helium, and sulfur hexafluoride (SF_6). The facility is equipped with sensors that measure relevant quantities, such as the water level, the temperature distribution, the gas composition, and the pressure of wave impacts. Furthermore, the facility is computer controlled, which allows continuous and repeatable measurements to be conducted.

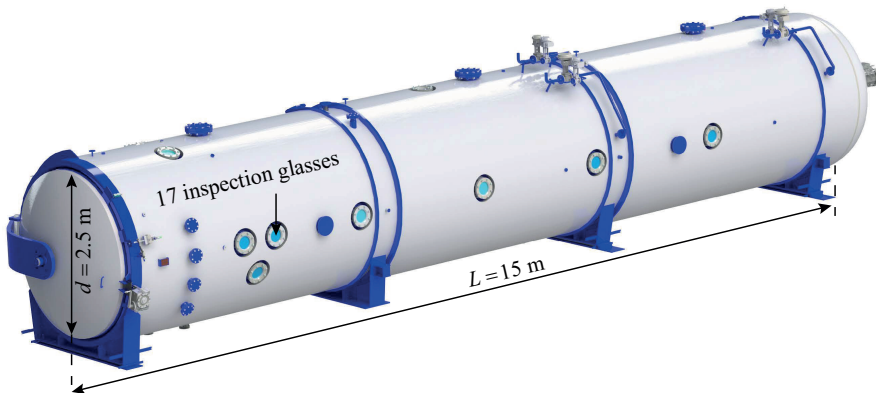


Figure 1.5: A schematic representation of the *Atmosphere* the new mutliphase test facility at MARIN (Adapted from MARIN, 2020, and used with permission). The autoclave with a diameter of 2.5 m and length of 15 m can house different experiments. Optical access to the experiments is provided by the 17 inspection glasses arranged in multiple configurations.

1.4 OBJECTIVES AND SCOPE OF THE RESEARCH

A detailed understanding of wave impacts on vertical walls is essential. However, the study of the phenomena that occur on the wave crest prior to impact is not trivial, due to both the inherent variation in wave generation and the difficulty of obtaining quantitative free surface measurements. In this work, we aim to gain insight in the sources of pressure impact variability. This is accomplished using direct measurements of the liquid free surface and particle image velocimetry of the surrounding air. Because of the complexity of the experimental measurements this work is limited to wave impact experiments of a single type (i.e., with a single steering signal and water depth) at atmospheric conditions. The wave is limited to that of plunging breaking wave with a large gas pocket that impacts on a vertical wall. The large gas pocket results in a significant gas flow between the wave crest and the vertical impact wall, which results in the formation of instabilities on the wave crest.

1.5 OUTLINE OF THE THESIS

This thesis is organized as follows. In Chapter 2 the measurement of complex free surface flows is discussed in the context of wave impact experiments. A technique is introduced to non-intrusively (i.e., without the need for seeding or patterns) measure free surface flows on a two-dimensional domain (i.e., $\eta = \eta(x, y)$) with a scanning light sheet and a stereo camera system. Additionally, the technique is designed to be used within the limitation of the *Atmosphere*. The accuracy of the measurement system is studied and measurements are presented at two length scales. The system accurately measures the free surface of an hydraulic jump at different Froude numbers and the free surface after impact of a liquid droplet; both measurements are obtained with the same camera calibration.

In Chapter 3 experimental measurements of the wave tip variability of an impacting wave are introduced. The impact pressure variability observed in sloshing experiments is often attributed to the formation of free surface instabilities on the wave crest. A repeatable wave is generated in the flume of the Hydraulic Engineering Laboratory at the Delft University of Technology. The source of wave tip variability is twofold, as it consist of *system* and *hydrodynamic* variability. Here, the system variability is minimized within the experimental limitations, which on a global scale results in a repeatable wave. However, locally significant variation (i.e., on the scale of a typical pressure sensor) in wave shape exists. Additionally, a shear instability develops on the thinning and elongating wave tip, which triggers the development of a Rayleigh-Taylor instability.

In Chapter 4 the gas flow over the wave crest is discussed. Particle image velocimetry measurements (PIV) are combined with stereo-PLIF measurements to obtain the gas flow over a plunging breaking wave prior to impact on a vertical wall. The PIV measurements are performed at two scales (i.e., two separate field of views)

to determine the global and local gas behavior. Typically the gas flow between the wave crest and the impact wall is often assumed to be constant, but it is here shown that the gas flow is skewed towards the wave tip. The velocity profile between the wave crest tip and the impact wall is similar to that of a potential flow past a bluff body. The high velocity near the wave crest tip can result in earlier than expected onset of instability development. Additionally, the gas flow tends to separate from the wave crest tip just moments prior to impact on the vertical wall. This results in the development of a secondary vortex with a lifetime that depends on the initial smoothness of the wave crest. The lifetime of the secondary vortex is significantly longer for an initially smooth wave crest, which results in an additional displacement of the wave crest tip.

Finally, in chapter 5, the general conclusions of this thesis are presented along with perspectives on further research.

SCANNING STEREO-PLIF METHOD FOR FREE SURFACE MEASUREMENTS IN LARGE 3D DOMAINS

In this chapter, we extend a planar-laser induced fluorescence (PLIF) method for free surface measurements to a three-dimensional domain using a stereo-camera system, a scanning light sheet, and a modified self-calibration procedure. The stereo-camera set-up enables a versatile measurement domain with self-calibration, improved accuracy, and redundancy (e.g., possibility to overcome occlusions). Fluid properties are not significantly altered by the fluorescent dye, which results in a non-intrusive measurement technique. The technique is validated by determining the free surface of a hydraulic flow over an obstacle and circular waves generated after droplet impact. Free surface waves can be accurately determined over a height of $L = 100$ mm in a large two-dimensional domain ($y(x, z) = 120 \times 62$ mm²), with sufficient accuracy to determine small amplitude variations ($\eta \approx 0.2$ mm). The temporal resolution ($\Delta t = 19$ ms) is only limited by the available scanning equipment ($f = 1$ kHz rate). For other applications, this domain can be scaled as needed.

This chapter is based on: M. van Meerkerk, C. Poelma, J. Westerweel, "Scanning stereo-PLIF for free surface measurements in large 3D domains", *Experiments in Fluids*, 61, 19, 2020

2.1 INTRODUCTION

Small-scale free surface dynamics play a significant role in many applications. For example, they strongly influence the response of structures to wave impacts (Lafeber et al., 2012a), and the transfer of heat, momentum, mass, and energy between the ocean and atmosphere (Buckley et al., 2016; Jähne et al., 1998). Therefore, measurements of the small-scale free surface dynamics are required. These measurements are typically performed with intrusive point measurements (e.g., resistive wave probes). However, instantaneous wave height measurements can be obtained with optical techniques that are non-intrusive and therefore preferential in many applications. These optical techniques can be categorized as *refraction*, *stereo-correlation* or *projection* based (Fig. 2.1).

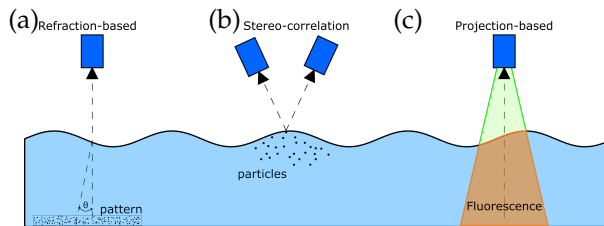


Figure 2.1: General measurement principle of free surface measurement techniques. (a) *Refraction*-based techniques relate the slope change to a change in height. (b) *Stereo-correlation* based techniques determine the three-dimensional world position of particles or naturally present features. (c) *Projection*-based techniques determine the free surface height with a projected pattern.

Techniques based on *refraction* relate the slope change of a liquid free-surface to the refraction of light. A one-dimensional collimated light source (e.g., laser beam) is typically used to determine the deflection on position-sensing photodiodes (J. Liu et al., 1993) or a camera. A collection of points can be obtained by rapidly scanning the light source over a line (Savelsberg et al., 2006). The technique can be extended to a two-dimensional domain by imaging a pattern through a refractive medium. The patterns are either created by a random-dot pattern (Moisy et al., 2009) or a distribution of particles in a flow (Gomit et al., 2013). Advantages of refraction-based techniques are the ease-of-implementation, the relatively large domain size, and the small error (Table 2.1). However, ray crossing, which occurs when either the surface curvature or the surface-to-pattern distance becomes too large, limits the measurement of steep and large amplitude waves (Moisy et al., 2009).

Stereo-correlation techniques either use stereo-vision to triangulate characteristic features, such as ocean whitecaps (Benetazzo et al., 2012), or use *particle image velocimetry* (PIV)/ *particle tracking velocimetry* (PTV) approaches to determine the free surface height. The particles used in these approaches are often buoyant (Turney et al., 2009) or neutrally buoyant (Douxchamps et al., 2005). The effect of particles on

surface tension can be minimized by ensuring that the particles are hydrophobic. However, particle clustering can occur in regions of convergence of interfacial velocity, which can result in local variance of fluid properties (Turney et al., 2009). The stereo-correlation techniques can obtain free surface heights over large spatial domains (Table 2.1). However, considerable effort is required to obtain appropriate illumination. Furthermore, the sensitivity to small amplitude free surface disturbances is limited (Zavadsky et al., 2017).

Lastly, *projection*-based techniques project an image or pattern on a liquid free surface. No surface seeding is required when there are naturally present contaminants (Gomit et al., 2015) or when the reflection of colored light is used (Dabiri et al., 2001). Otherwise, a dye is required to make the liquid fully opaque (Tsubaki et al., 2005; Cobelli et al., 2009) or to make the liquid fluorescent (André et al., 2014; Buckley et al., 2017; Duncan et al., 1999). For fully opaque fluids, fringe projection techniques can be applied to obtain accurate, two-dimensional free surface height measurements in large three-dimensional domains (Cobelli et al., 2009). For fluorescent fluids, accurate line measurements can easily be obtained with planar laser-induced fluorescence (PLIF) techniques (Duncan et al., 1999). Furthermore, the fluorescent dye does not change the fluid properties as the concentration of dye is typically low.

So far, PLIF-based free surface measurement techniques have been limited to line measurements. The technique offers accurate free surface height measurements, without altering the fluid properties or the need for fixed patterns. Furthermore, per-pixel wave height measurements can be obtained along a line (Buckley et al., 2017). In contrast, *stereo-correlation* based approaches use particles or features and are limited by the distribution of these particles or features over the surface. The accuracy of PLIF-based techniques can even be improved with detection methods relying on light sheet properties (e.g. André et al., 2014). However, the PLIF-based approaches are currently limited to planar domains.

This study presents a two-dimensional PLIF-based approach, which applies a stereo-camera set-up with a scanned light sheet (Brücker, 1996). Conventional free surface measurements approaches are summarized in Table 2.1. The current technique can be used in experiments with limited optical access, due to the small camera separation angle. A multi-step calibration procedure is used to reduce the calibration requirements (Hori et al., 2004; Wieneke, 2008). These optical limitations are imposed by future work in the newly build Multiphase Wave Lab at MARIN in The Netherlands. The technique is also evaluated for typical optical conditions. Measurements can be obtained in relatively large three-dimensional domains ($(x, y, z) = (120, 100, 62)$ mm) with sufficient accuracy to resolve small amplitude waves ($\eta \approx 0.2$ mm).

The chapter is organized as follows. The experimental set-up and equipment are introduced in Section 2.2. This section also describes the calibration procedure. Section 2.3 shows and discusses the measurements of a hydraulic flow over an obstacle and the waves generated by a droplet impact are shown. Finally, the last section presents some concluding remarks.

Table 2.1: Overview of selected free surface measurement techniques.

Method	Domain size ($x \times y$) m ²	Frequency (f) Hz	Amplitude (A) m $\times 10^{-3}$	Accuracy ($\Delta A/A$) %
Refraction-based techniques				
Laser beam refraction				
Savelsberg et al. (2006)	0.05	100	$O(1)$	-
Free Surface Synthetic Schlieren				
Moisy et al. (2009)	0.2×0.2	100	$O(0.01 - 1)$	$O(2)$
Gomit et al. (2013)	0.2×0.2 0.4×0.5	10 10	$O(13)$ $O(10)^*$	$O(3)^*$ $O(7)^*$
Stereo-correlation techniques				
Benetazzo et al. (2012)	35×35	5 – 10	$O(10^3)$	$O(1 - 2)$
Turney et al. (2009)	0.07×0.7	250	$O(10)$	$O(10)$
Douxchamps et al. (2005)	0.5×0.5	25 & 250	$O(40)$	$O(10 - 15)$
Zavadsky et al. (2017)	0.25×0.4	100	$O(10)$	$O(15 - 30)^*$
Projection-based techniques				
Gomit et al. (2015)	4×8	$O(0.01)$	$O(130)$	$O(8)$
Dabiri et al. (2001)	0.18×0.18	30	1.2	$O(6)$
Cobelli et al. (2009)	0.3×0.45	4×10^3	$O(100)$	$O(0.2)$
Tsubaki et al. (2005)	$O(0.14 \times 0.18)$	12	$O(10)$	$O(10)$
André et al. (2014)	0.0075	8×10^3	$O(1)^*$	$O(1)^*$
Buckley et al. (2017)	0.51	7.2	$O(1 - 20)$	$O(1 - 10)^*$
Duncan et al. (1999)	0.12	500	$O(50)^*$	$O(1)^*$

Several parameters are estimated from data presented in each paper, which is denoted by an asterisk (*). A parameter that was not defined and could not be estimated is denoted by (-).

2.2 METHOD

The method allows one to extend one-dimensional height measurements ($y(x, t)$) typically obtained with PLIF (Table 2.1) to a two-dimensional domain ($y(x, z, t)$). In essence this could be achieved with a single camera and a multi-plane calibration procedure. However, a stereo-camera set-up allows one to apply a broad calibration that can be refined with an adapted self-calibration procedure as the z -direction is constrained by the scanned light sheet. Furthermore, the accuracy of the method can be improved with a stereo-camera set-up. This results in a robust method that can, with some adjustments, be used in applications with occlusions.

The experimental set-up and equipment are introduced in this section. Furthermore, the method to obtain stereo-PLIF measurements is detailed. First, the relevant equipment is introduced. Then, the edge detection procedure is introduced, which is required for the adapted self-calibration procedure and measurements. Finally, the stereo-PLIF calibration is detailed, which uses an adapted self-calibration procedure.

2.2.1 FLOW FACILITY

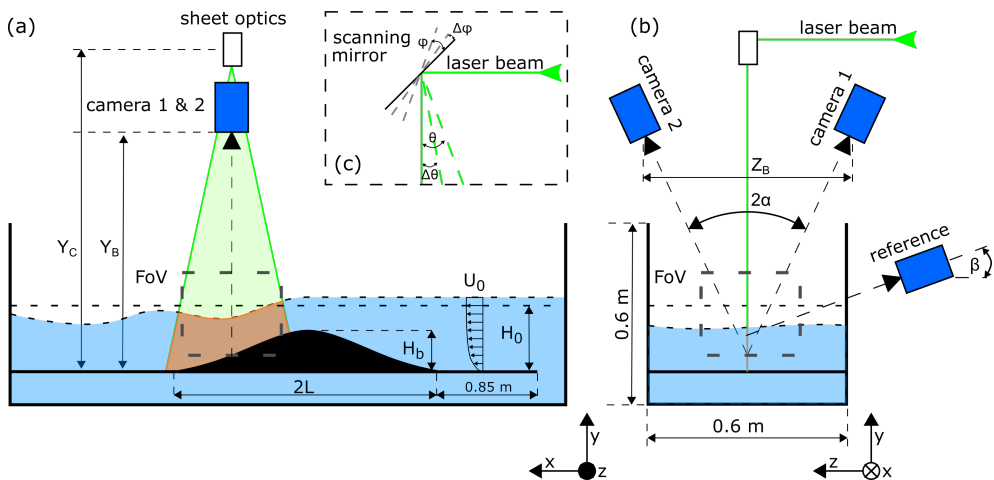


Figure 2.2: Schematic of the experimental set-up. (a) Side-view of the set-up. The wave pattern is determined by the incoming flow (U_0), the initial water depth (H_0), and the obstacle height (H_b). The cameras for the PLIF and stereo-PLIF are aligned on a yz -plane. (b) Front-view of the set-up, orientation of the PLIF (reference) and stereo-PLIF system (camera 1 and 2), with respect to the light sheet location. Two-dimensional free surface measurements are obtained with the stereo-PLIF system. Reference measurements are obtained at the central light sheet location. (c) The light sheet is scanned with an oscillating mirror driven by a galvanometer over an angle interval of ($\Delta\theta$) spanning a separation angle (θ).

Figure 2.2 shows the experimental set-up used in this study. The experiments are performed in the water tunnel of the Laboratory for Aero- and Hydrodynamics at the Delft University of Technology. The test section has an area of $0.6 \times 0.6 \text{ m}^2$ and a length of 5 m. A false bottom, 190 mm above the channel bottom, is used to generate a defined boundary layer, and to allow the water tunnel to be operated at a reduced water depth.

Free surface waves are generated behind an obstacle, which is mounted on the false bottom at a distance of 0.85 m from the leading edge. The shape of the obstacle is defined by a fourth-order polynomial

$$y(x) = H_b(1 - 2(x/L)^2 + (x/L)^4) \quad (2.1)$$

with $H_b = 0.117 \text{ m}$ the obstacle height, and $L = 0.295 \text{ m}$ the obstacle half-length (Gui et al., 2014).

In the current work, a number of free surface wave patterns is obtained by varying the Froude number, while keeping the initial water depth constant. The free surface wave pattern is defined by the water depth above the obstacle ($H_0 - H_b$) and the upstream Froude number $Fr = U_0 / \sqrt{gH_0}$, where U_0 is the upstream bulk velocity, g is the gravitational acceleration, and H_0 is the initial water depth. The upstream Froude number is always sub-critical ($Fr < 1$). However, transition to critical conditions ($Fr = 1$) occurs at or near the obstacle (Gui et al., 2014).

The upstream flow conditions, at constant water depth (H_0), are determined prior to the free-surface wave height measurements (Table 2.2). The liquid velocity is measured with a disk-type programmable electromagnetic liquid velocity meter (P-EMS E30, Deltares) where one of the axes is aligned with the flow. The probe is calibrated for a velocity range of $\pm 1 \text{ m s}^{-1}$ with an accuracy of 1%. The initial water depth (H_0) is measured with a ruler.

Table 2.2: Flow conditions for the free surface waves generated behind the obstacle.

Case	$U_0 \times 10^2 \text{ [m s}^{-1}\text{]}$	$H_0 \text{ [m]}$	$\frac{(H_0 - H_b)}{H_0}$	$Fr \times 10^2$
1	5.23 ± 0.17	0.144	0.189	4.40 ± 0.14
2	6.40 ± 0.17	0.144	0.189	5.39 ± 0.14
3	11.2 ± 0.19	0.144	0.189	9.43 ± 0.16

2.2.2 REFERENCE MEASUREMENT

A commonly applied PLIF system is used as a reference for the stereo-PLIF free surface measurements (Duncan et al., 1999; Buckley et al., 2016). The light sheet from a Nd:YLF laser (LDY 304PIV laser, Litron) illuminates the liquid containing a fluorescent dye (Rhodamine WT at 120 mg m^{-3}). The concentration of fluorescent dye is low enough such that it does not influence the static surface tension of the fluid (Appendix A). The dynamic surface tension is more appropriate for steep waves

where compression can locally alter the surfactant concentration (Duncan et al., 1999). However, for the current application the static surface tension is sufficient, but the effect of compression on the surfactant concentration at a time scale similar to the wave action needs to be investigated in future work. Images are acquired with a high-speed CMOS camera (Imager HS 4M, LaVision) equipped with a 105mm Micro-Nikkor objective and a high-pass filter (OG570, Schott). The magnification (M_0) at the center plane is about $M_0 = 0.1$, with an object distance of $Z = 1$ m. A large depth-of-field is obtained, which with an aperture of $f/11$, and a wavelength of $\lambda = 527$ nm, results in $\delta z \cong 4(1 + 1/M_0)^2 f^{\#2} \lambda \approx 30$ mm (Adrian et al., 2011). The camera (Fig. 2.2) is placed at an angle (β) of 15° with respect to the light sheet (xy -plane) to avoid interference from the liquid meniscus (Belden et al., 2011).

An inverse, third-order polynomial is used to determine the mapping from image to world coordinates (Soloff et al., 1997). The camera is calibrated using a two-plane dot-pattern target (Type 22, LaVision). A resolution of 10.1 pixels per millimeter is obtained over a field-of-view of approximately 180×180 mm².

2.2.3 STEREO-PLIF MEASUREMENT

The stereo-PLIF system extends a PLIF system to a three-dimensional domain with a scanning light sheet and a stereo-camera set-up. The method is comparable to conventional techniques such as scanning-PIV (Brücker, 1996). Images are acquired with two high-speed CMOS cameras (Imager HS 4M, LaVision) equipped with a 105mm Micro-Nikkor objective and a high-pass filter (OG570 Schott). The magnification at the center plane is approximately $M_0 = 0.1$, which with an aperture of $f/11$ results in a depth-of-field of $\delta z \approx 30$ mm.

The cameras are placed in a stereo configuration (Fig. 2.2), with a full separation angle (2α) of either 30° or 50° . These two full separation angles are imposed by optical limitations in the experimental facilities, respectively the Multiphase Wave Lab¹ at MARIN in The Netherlands and the water tunnel of the Laboratory for Aero- and Hydrodynamics at the Delft University of Technology. Optimal accuracy, for conventional stereo-PIV applications, is obtained for a full separation angle of $60^\circ \leq 2\alpha \leq 90^\circ$ (Lawson et al., 1997). The two angles are used to determine the influence of the separation angle on the measurement accuracy at comparable focal points ($L_f \approx 1$ m). Consequently, the nominal magnification remains the same for both camera separation angles. Therefore, the error is expected to scale as $e_r \propto \sigma_{\Delta z} / \sigma_{\Delta x} \propto \tan(\alpha)^{-1}$ (Lawson et al., 1997).

Two-dimensional free surface height measurements are obtained by scanning the light sheet in a sawtooth profile over the three-dimensional measurement domain with an oscillating mirror driven by a galvanometer (CT-6210H, Cambridge Technology) located at $y_c = 1745$ mm above the false bottom (Fig. 2.2a). The large

¹ The Multiphase Wave Lab is a wave flume enclosed in an autoclave, which can be operated at elevated pressure, and temperature. Furthermore, the gas surrounding the fluid can be replaced by mixtures. The optical access to the wave flume is severely limited, due to the small viewing windows of the autoclave.

distance of the scanning mirror ensures almost vertical measurement planes (Fig. 2.5a), with a maximum angle deviation, with respect to the y -axis, of approximately 2.3° at the outer edges of the measurement domain ($z_d \approx 62$ mm) (Fig. 2.5b).

2.2.4 EDGE DETECTION PROCEDURE

An accurate edge detection method is required for the calibration procedure and the free surface reconstruction. Large variations in image intensity (I) are observed as a result of the liquid properties (Fig. 2.3a). The variations are a result of refraction, light focusing, and reflection at the air-water interface. Traditional edge detection can result in detection errors due to the semi-reflective properties of the air-water interface (André et al., 2014).

The edge detection error depends also on the camera separation angle. The specular bias is reduced at small camera separation angles, but the quantization errors increase. Hence, there is trade-off between detection errors and quantization errors (Benetazzo, 2006). Furthermore, the variation in intensity along the laser light sheet can introduce other angle dependent errors (André et al., 2014). These errors can be reduced with other detection methods, such as hyperbolic tangent fit methods (Hwung et al., 2009). However, the detection accuracy is not necessarily improved, and often these methods require an increased computational effort. Instead, a multi-step intensity-based detection procedure is used in the current work.

The edge information is obtained from the raw image (2016×2016 pixels) with a multi-step intensity-based detection procedure (Fig. 2.3a). First, the background intensity variation, based on the windowed mean and standard deviation, is determined over the first part of the image (500 pixels). Then, a discontinuous threshold distribution is determined per window, which is defined as the mean plus two times the standard deviation (Fig. 2.3b). Finally, a continuous threshold distribution is obtained by fitting a second-order polynomial to the discontinuous data.

The raw image is binarized with the continuous threshold distribution. Then, the image is smoothed with a two-dimensional 3×3 Gaussian filter to suppress the small-scale image noise (Fig. 2.3c). Finally, the edge is defined as the pixel with a gray level above the threshold with the lowest y -value (i.e. topmost “white” pixel in Fig. 2.3c).

Detection errors can occur with a per-column threshold operation. However, pixel data cannot be easily filtered, due to the variation in magnification over the domain. This would result in a variable filter length in world coordinates. Therefore, pixel coordinate data is processed without further filtering.

2.2.5 STEREO-PLIF CALIBRATION

The scanning stereo-PLIF system is calibrated with a self-calibration procedure after an initial calibration at the outer edges of the measurement domain (i.e., front and

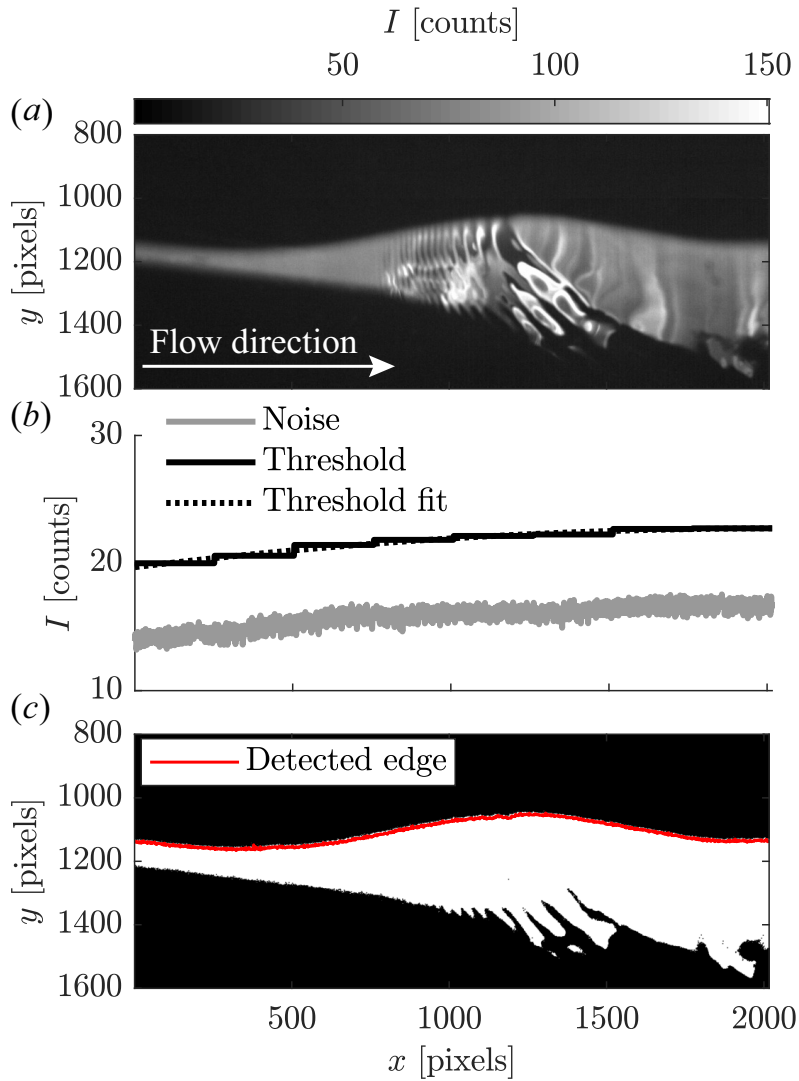


Figure 2.3: Image processing steps for edge detection of the free surface waves. (a) The raw image (2016×2016 pixels) is cropped to show the surface waves. (b) The threshold distribution is determined over the top part of the image (500 pixels), which does not contain free surface information. (c) The image is thresholded and smoothed with a (3×3) Gaussian filter. The edge is detected based on the maximum value per column.

aft plane). An updated mapping function is determined at each light sheet location for the two-dimensional free surface measurements.

The self-calibration procedure is similar to typical stereo-PIV applications (e.g., Wieneke, 2008; Horii et al., 2004). There is, however, a distinct difference. A stereo-PLIF measurement contains only curvilinear lines (i.e., the intersection of the light sheet with the surface) at a specific free-surface height, whereas a stereo-PIV measurement contains information over the entire field-of-view. Images of the liquid free surface are obtained at several unique still water heights, hereby sampling the entire field-of-view. The whole process of the stereo-PLIF calibration procedure is detailed in the following sections.

First, a broad calibration is performed at two planes enclosing the measurement domain (i.e., positive and negative z), shown in Fig. 2.4, with a two-plane dot pattern target (Type 22, LaVision). An inverse third order polynomial mapping function $\vec{x} = F_{0,i,j}^{-1}(\vec{X})$ is determined for each camera (j) and plane (i), which maps pixel coordinates $\vec{X} = (X, Y)$ to world coordinates $\vec{x} = (x, y, z)$ (Soloff et al., 1997).

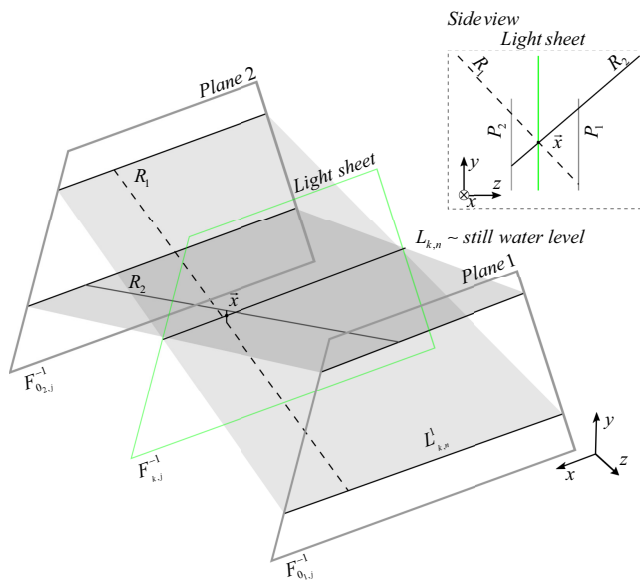


Figure 2.4: Definition of variables used in the adapted self-calibration procedure. The stereo cameras are calibrated, with an initial mapping ($F_{0,i,j}^{-1}$), at the outer edges of the domain (i.e., Plane 1 and 2). The projection lines (R_j) formed by backprojection are used to triangulate the still water level (i.e., curvilinear line $L_{k,n}$). An updated mapping $F_{j,k}^{-1}$ is determined at each light sheet location (k) with the triangulated world (\vec{x}) and pixel (\vec{X}) coordinates. The inset shows a side view of the intersecting projection lines and the calibration planes (P_1, P_2) at the outer edges of the domain.

Then, images of the free surface are acquired at several still water heights ($N = 14$) for each light sheet location (k). The edge detection procedure is applied to obtain

curvilinear lines ($L_{k,n}$) for each light sheet location (k) and still water height (n). These lines span the entire field-of-view.

Compared to stereo-PIV the lines do not contain identifiable points (i.e., matching world and pixel coordinates). Furthermore, identifiable points can not be obtained with the approach of Hori et al. (2004), as the scanning mirror is not calibrated. Identifiable points are obtained by distance minimization between camera projection lines ($R_j(\vec{x})$), which are the rays formed by back-projection of single pixels to the enclosing calibration planes (Fig. 2.4). The projection lines of both cameras are matched based on the minimal distance between skew lines with a maximum distance threshold (Gellert et al., 1989). The point of minimal distance defines the world coordinate (\vec{x}) with corresponding pixel coordinates for both cameras (Fig. 2.4).

Next, an updated inverse polynomial mapping is determined for each camera and light sheet location (k). The matched features are all constrained on a light sheet (i.e., a single plane), which enables the use of back-projection methods. The inverse mapping defines world coordinates $(x, y, 0) = F_{j,k}^{-1}(\vec{X})$ on a light sheet plane (Adrian et al., 2011). The mapping function is completed by fitting a plane to the z -coordinates ($z = f(x, y)$).

Finally, the calibration domain is aligned with the liquid free surface, as the rough calibration is not necessarily aligned with the still water level. The two-dimensional free surface height $y = y(x, z)$ is determined with the calibrated stereo-PLIF system. A plane is fitted to the reconstructed two-dimensional free surface, which is subtracted as a correction for the misalignment.

2.2.6 POST-PROCESSING

Post-processing is applied to the world coordinates obtained with both stereo cameras. The post-processing is applied to obtain uniformly distributed coordinates. Furthermore, the obtained data is filtered and averaged to obtain a combined stereo-PLIF measurement.

First, the pixel data obtained with the edge processing procedure is mapped to the respective measurement plane (i.e., light sheet location k) using the updated mapping function. The stereo camera data can not be directly combined as the world points are non-uniformly distributed. Therefore, the world data is interpolated, with a linear interpolation method, to a uniformly distributed grid over the x -direction with a spacing of $\Delta x = 0.1$ mm. Higher-order interpolation methods are in the current application not required, as a grid point is displaced by only $\|\vec{x} - \vec{x}_i\| \approx 0.04$ mm on average.

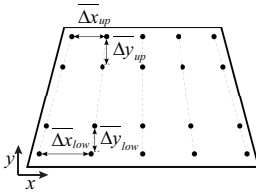
Then, the now uniformly distributed stereo data is filtered. First, a Hampel filter, with a filter length of $L_{h,f} = 2.7$ mm, is applied, which removes values that deviate more than three standard deviations from the median over the filter length (H. Liu et al., 2004). Then, to smooth the data a second order Savitzky-Golay finite impulse response filter is applied, with a filter length of $L_{h,s} = 2.7$ mm (Orfanidis, 1995).

Finally, the stereo-PLIF data is obtained by averaging the data from both stereo cameras.

2.2.7 CALIBRATION ACCURACY

The resolution of the initial polynomial mapping is not constant over the field-of-view (Table 2.3). The large angle of the stereo cameras, with respect to the z -axis, results in a magnification change over the field-of-view. Hence, there is a significant difference between the vertical and horizontal resolutions, where the horizontal resolution changes approximately 20 % over the field-of-view. Furthermore, the accuracy changes as function of the camera separation angle (Lawson et al., 1997).

Table 2.3: Resolution change over the field-of-view for the initial polynomial mapping. The initial mapping is defined at the outer edges of the domain (i.e., plane 1 and 2). The resolution change of the stereo-PLIF system, with units of pixels mm^{-1} , is presented per separation angle (2α) and averaged over the two initial calibration planes.



2α	$\overline{\Delta x}_{\text{up}}$	$\overline{\Delta x}_{\text{low}}$	$\overline{\Delta y}_{\text{up}}$	$\overline{\Delta y}_{\text{low}}$
30	11.0	9.2	2.6	2.5
50	14.2	11.4	5.4	5.4

A measure of accuracy for the self-calibration procedure is the standard deviation per still water height. Therefore, a selection of still water levels used in the self-calibration procedure for a calibration domain of $z_d \approx 62$ mm, measurement plane spacing of $\Delta z \approx 3$ mm, an initial domain size of $\Delta z_d = 80$ mm, and camera separation angle of $2\alpha = 50^\circ$ are shown in Fig. 2.5a. The standard deviation varies from $\sigma_{\text{up}} = 0.52$ mm to $\sigma_{\text{down}} = 0.30$ mm over the height $-110 \leq y \leq 50$ mm with an average of $\bar{\sigma} = 0.38$ mm; see Table 2.3. The higher standard deviation of σ_{up} is either caused by the increased magnification at the top of the domain or the limited depth-of-field (i.e. the edge of the focal domain), which is evident from the larger spread over the x -direction (Fig. 2.5b). The measurement planes are positioned at a small angle, which remains minimal (2.3°) even at the outer edges of the domain (Fig. 2.5b). Furthermore, the angle could be removed easily by interpolating the data to a vertical plane. The virtual location of the scanning mirror, that is the intersection point of the measurement planes, is located at $y \approx 1743$ mm above the false bottom, which corresponds with the measured value of $y_c \approx 1745$ mm.

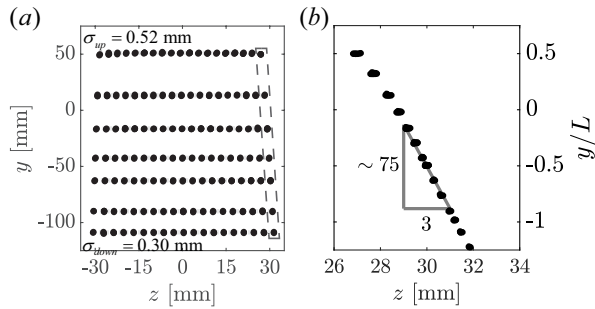


Figure 2.5: Still water levels used for the self-calibration procedure. (a) Triangulated still water heights ($N = 14$) for $z_d \approx 62$ mm, $\Delta z = 3$ mm, and $2\alpha = 50^\circ$, showing a change in angle per light-sheet location (k) and a change in domain size over the z -direction. (b) Zoom-in of the dashed box. The variation in z -direction is largest at the edges of the domain, with an angle of $\tan^{-1}(3/75) \approx 2.3^\circ$ with respect to the y -axis.

The accuracy of the self-calibration procedure is further evaluated by comparing the still water levels reconstructed with the reference and stereo measurement system (Fig. 2.6). Measurements are performed with the stereo cameras at two different separation angles (2α), while maintaining a constant focal point. The zero level correction is performed at equal still water level for both the stereo and reference measurement. However, the zero level is not equal for the two separation angles.

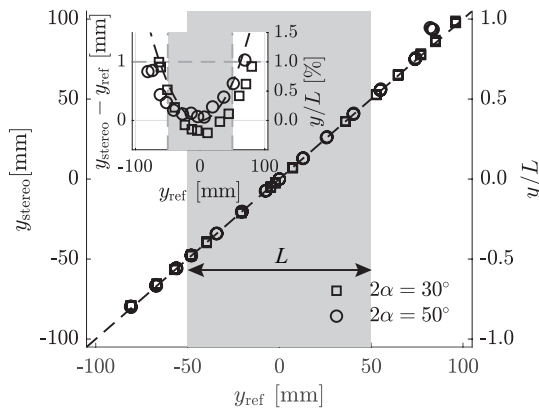


Figure 2.6: The still water heights used for the self-calibration procedure are shown, per measurement domain (z_d), over the domain height (y) with the reference measurement (y_{ref}) on the horizontal, and the stereo measurement (y_{stereo}) on the vertical axis. To guide the eye a dashed line (---) is introduced as $y_{stereo} = y_{ref}$. The inset shows the difference between $y_{stereo} - y_{ref}$ for separation angle $2\alpha = 30^\circ$ as (\square), and $2\alpha = 50^\circ$ as (\circ). The y_{stereo} data is normalized with the desired domain size L of 100 mm.

The free surface height is reconstructed accurately over the domain size of $-100 \leq y \leq 100$ mm without significant influence of the domain size (z_d) and inter-plane spacing (Δz) for both camera separation angles (Fig. 2.6). The difference between $y_{\text{stereo}} - y_{\text{ref}}$ over the domain size, for either separation angle $2\alpha = 30^\circ$ (indicated by \square) or $2\alpha = 50^\circ$ (indicated by \circ), is relatively small, as shown in the inset of Fig. 2.6. For both separation angles the error remains within 1 % of the target domain size (L) of 100 mm. A systematic error is observed, which clearly displays a parabolic behavior.

2.3 RESULTS AND DISCUSSION

2.3.1 HYDRAULIC FLOW

The free surface waves behind an obstacle are measured at two separation angles (2α) for three different Froude numbers (Table 2.2). The free-surface wave patterns vary over a significant height, which is ideal for a proof of principle measurement. Furthermore, the wave patterns display a variety of length scales from capillary waves to large free surface undulations as shown in Fig. 2.7. These free surface undulations are clearly observed to travel downstream as shown in the animation (Movie 2.1).

An instantaneous snapshot of the free surface height (y) is shown in Fig. 2.8 (a,d,g) for the three different Froude numbers. The measurements are obtained for a domain size of $z_d \approx 62$ mm, plane spacing of $\Delta z = 3$ mm, and a separation angle of $2\alpha = 50^\circ$. The free surface height is reconstructed over $N_p = 19$ measurement planes with an acquisition frequency of $f_a = f/N_p \approx 53$ Hz per scan, where the cameras and scanning mirror operate at $f = 1$ kHz.

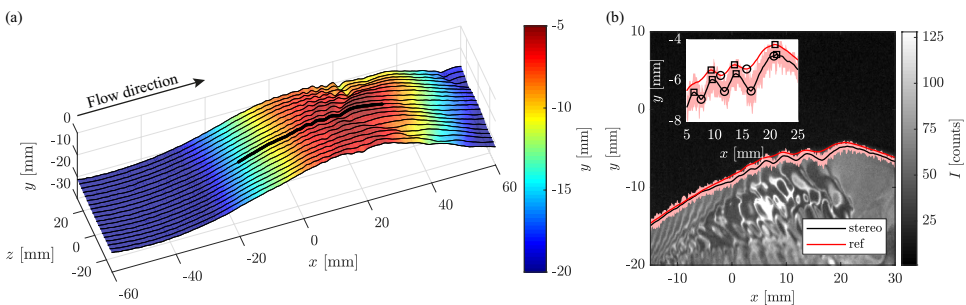


Figure 2.7: (a) Instantaneous free surface height for $Fr = 0.054$. The obstacle center is located at $x \approx -80$ mm. The free surface displays typical crescent shaped disturbances, which can be clearly observed in the animation (Movie 2). The thick black line represents the data shown in (b). (b) The back-projected reference image is shown, with the stereo and reference data at the corresponding location. The inset shows the difference between the stereo and reference measurement, with an indication of the local peaks (\square) and troughs (\circ). Panel b will be discussed later.



Movie 2.1

The differences in amplitude and wavelength of the free surface waves are apparent. The temporal variance of ($\eta(x, z, t) = y - \bar{y}$), with respect to the temporal mean \bar{y} , is clearly observed in a space-time diagram. These space-time diagrams are obtained at two locations, spanning the z -direction, as shown in Fig. 2.8 (b-c,e-f,h-i).

Limited free surface disturbances, without a repetitive pattern, are expected at $x = -40$ mm (Fig. 2.8 b,e,h), as the upstream flow is relatively uniform. There is indeed no apparent pattern visible over the z -direction. However, the temporal fluctuations ($y - \bar{y}$) for the first two cases are still significant ($\sigma_1 = 0.34$ and $\sigma_2 = 0.48$ mm). These periodic wave shape variations over time (Fig. 2.10 b,e) are introduced by fluctuations in the upstream flow. For $Fr = 0.094$ (Fig. 2.10 h) the velocity fluctuations have a negligible influence on the drowned hydraulic jump. Therefore, the standard deviation for the measurement at $Fr = 0.094$ is considered as a representable error measure, which has a magnitude of $\sigma_3 \approx 0.15$ mm. The bias error, between the stereo and reference measurement, defined as the difference between the temporal average of the stereo and reference measurement, is 1.0 mm for $Fr = 0.094$, or 1 % of the target domain size.

The second location is defined for each Froude number, to capture the changes in the free surface behavior. For $Fr = 0.044$ at $x = 20$ mm (Fig. 2.8c), small variations in span wise wave behavior are observed. For the $Fr = 0.054$ at $x = 10$ mm (Fig. 2.8f), the span wise variations are more pronounced with an increased disturbance amplitude. Furthermore, large, span wise moving, surface disturbances are observed. For the final measurement at $Fr = 0.094$, a relatively stationary free surface is expected. However, large free surface disturbances are observed. These disturbances occur due to air bubbles trapped on top of the recirculating flow of the submerged hydraulic jump (Te Chow, 1959), which can be clearly observed in the animation (Movie 3).

The shape of the crescent-shaped disturbance, with preceding capillary waves, observed in Fig. 2.8d resembles the instabilities observed on spilling breakers (Su et al., 1982; Duncan et al., 1999). The surface disturbance shown by Gui et al., 2014 is, however, not observed with the current free surface measurements.

It is found that bubbles on the surface seriously deteriorate the signal quality, so that the measurement technique is not suited for flows with a lot of air bubbles. An example of such a detection error is shown in Fig. 2.9. The viewing lines of stereo-camera 1 cross the interface of an air bubble (Fig. 2.9a). This is registered as an additional interface above the true interface, due to the reflection of light in the air bubble. Camera 2 registers a shadow below the true interface, as the fluorescent light is reflected (Fig. 2.9b). However, the error introduced by the air bubble is limited (Fig. 2.9c). In the current work, a quality indicator (e.g. the vector norm of the distance between triangulated and mapped data) is not included, but more elaborate validation and/or processing can easily be implemented for particular situations (e.g. do not average if one of the cameras has “step-like” results).



Movie 2.2



Movie 2.3

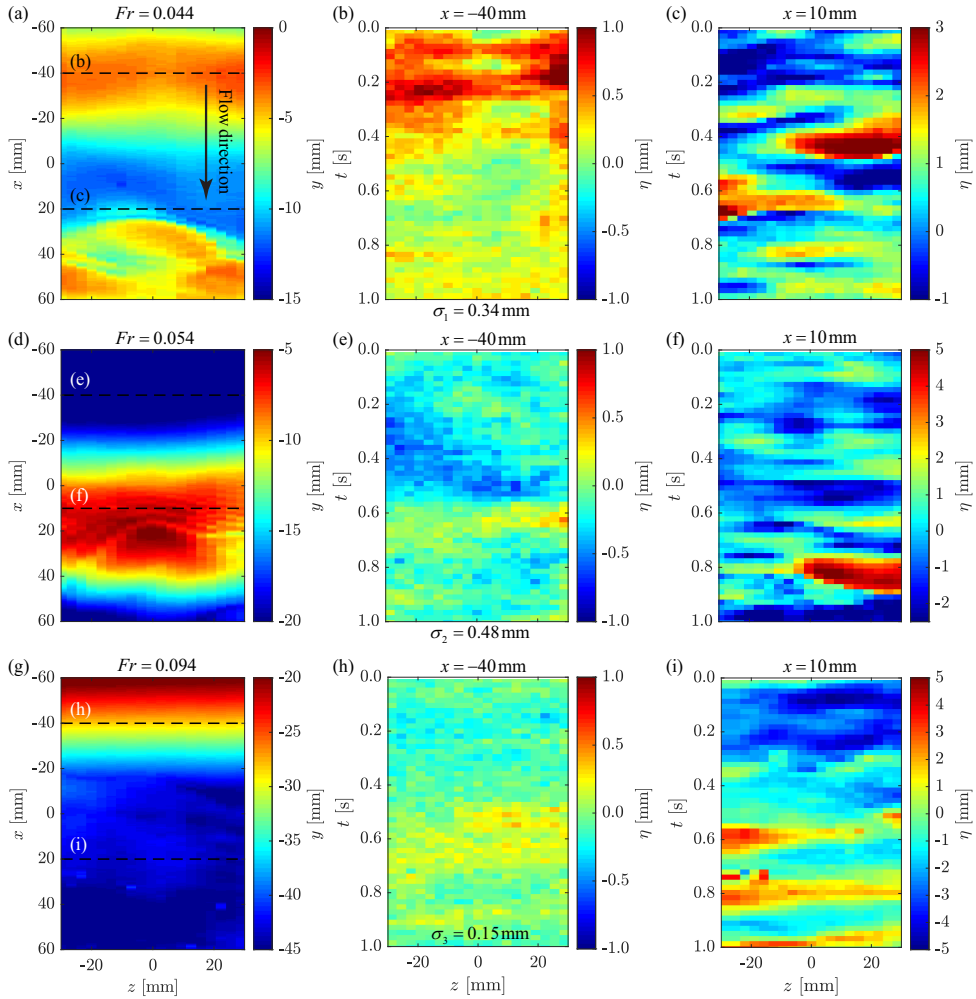


Figure 2.8: Instantaneous free surface height, shown in (a, d, g), for different Froude numbers (Table 2.2). Fluid flows from negative to positive x and the obstacle center is located at $x \approx -80$ mm. The space-time diagrams of free surface height ($\eta(x, z, t) = y - \bar{y}$) at the respective x -coordinates per Froude number, indicated by (---), are shown in (b-c, e-f, h-i). Note that the color scaling is different for each case.

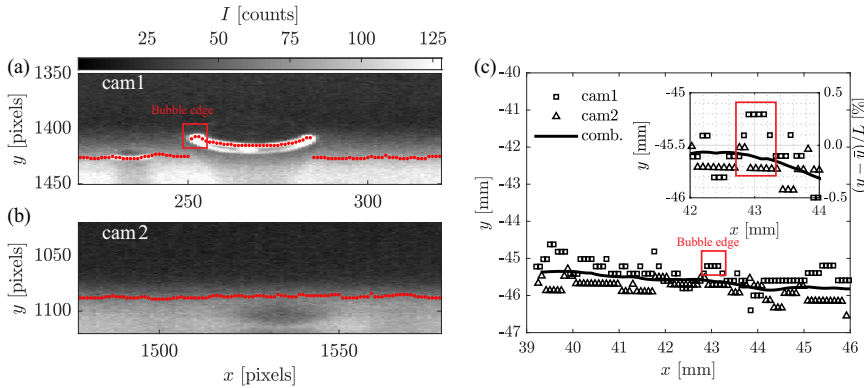


Figure 2.9: Image of an edge detection error due to the presence of an air bubble on the liquid surface at the recirculation area of the drowned hydraulic jump ($Fr = 0.094$). (a) Stereo camera 1 looks through the interface of the air bubble, which results in a detection error close to the liquid free surface. (b) Stereo camera 2 does not look through the bubble, but the bubble appears as a shadow below the interface. (c) The local free surface height per camera (cam 1/2) and filtered free surface height (comb.) are shown at the detection error location. The inset shows a zoom at the detection error location, which shows an error of approximately 0.4 mm.

A comparison between the temporal mean of the stereo and reference measurements is shown in Fig. 2.10a. The average difference is negligible (0.2 mm or 0.2 % of the target domain size) with a maximum deviation of 0.45 mm. The error for $Fr = 0.044$ seems to be considerably larger. However, the standard deviation of the difference is, for both cases (i.e. $\sigma_1 = 0.45$ and $\sigma_2 = 0.28$ mm), comparable to the previous error definition. The amplitude of the free surface disturbance is estimated as $A_1 \approx 3.2$ mm and $A_2 \approx 8.6$ mm, which results in a relative error (σ_i / A_i), as defined in Table 2.1, of 14 % and 10 % respectively. However, the relative error compared to the target domain size (σ_i / L) is negligible (~ 0.4 %). For the smaller camera separation angle ($2\alpha = 30^\circ$) the averaged difference remains the same, whereas the maximum increases to 0.81 mm. The reference camera system also has an inherent error, which for a typical PLIF system is approximately 0.5 mm (Duncan et al., 1999). In this case the typical error of the reference system is estimated as the error induced by a single pixel shift, which corresponds to 0.1 mm or approximately 1 – 3 % of the amplitude. The errors of the stereo-camera system are comparable to typical PLIF systems (e.g., Duncan et al., 1999; Buckley et al., 2017).

The space-time diagrams of the disturbances ($\eta(x, 0, t) = y - \bar{y}$) are, for $Fr = 0.044$ and $Fr = 0.054$, shown in Fig. 2.10b-c. These results are obtained at the center line of the domain. The growth and decay of the free surface disturbances are visible. First of all, the amplitude of the free surface disturbances is observed to be larger for $Fr = 0.044$, whereas the occurrence frequency is higher for case one. Second, for $Fr = 0.054$ a crescent type of disturbance is observed, where the small amplitude waves are observed to travel upstream (towards negative x).

The local phase speed of the disturbances is, for both cases, estimated with a line as $c_{p,1} \approx 24.7$ and $c_{p,2} \approx 29.7$ cm s⁻¹, respectively, (Fig. 2.10b-c). The estimate is checked by comparing the wavelength of the disturbances on the wave crest for $Fr = 0.054$ (Fig. 2.7a) with linear theory. A zoom-in of the disturbance is shown in Fig. 2.7b, where peaks (\square) and troughs (\circ) are indicated. The wavelength λ of the first disturbance, defined as the difference between crests and troughs, is approximately $\lambda_1 = 4.8$ mm ($k = 1.3 \times 10^3$ m⁻¹). The dispersion relation for gravity-capillary waves on still water is,

$$\omega^2 = \left(gk + \frac{\gamma}{\rho} k^3 \right) \tanh(kH), \quad (2.2)$$

with γ the surface tension, $k = 2\pi/\lambda$ the wavenumber, and H the water depth. For deep-water surface waves the depth does not influence the dispersion relation (i.e., $\tanh(kH) \cong 1$) (Whitham, 1999; Lamb, 1993). The local phase velocity, on still water, is defined as $c = \omega/k$. Based on the wavelength of the first disturbance ($k = 1.3 \times 10^3$ m⁻¹) with surface tension and density values of $\gamma = 0.072$ Nm⁻¹, $\rho = 998$ kg m⁻³, respectively, the phase velocity is estimated as $c_{p,\lambda_1} \approx 32$ cm s⁻¹. The wavelength of the following crest is estimated as $\lambda_2 = 7.3$ mm, which results in a phase velocity of $c_{p,\lambda_2} \approx 28$ cm s⁻¹. The determined phase velocities are comparable to the estimate of $c_{p,2} \approx 29.7$ cm s⁻¹ (Fig. 2.10c). A small difference is expected as the space-time diagram is determined in a fixed frame of reference, whereas the phase velocity is based on a moving frame of reference. The order of magnitude of the Doppler shift $U = c_{p,2} - \bar{c}_{p,\lambda} \approx 2.4$ cm s⁻¹ is comparable with the upstream bulk velocity (Table 2.2). The ability of the method to measure capillary waves is indicated by the estimated wavelength and corresponding phase velocity.

2.3.2 WAVE SWELL BY WATER DROP IMPACT

As a second test case, a droplet impact is generated by releasing a water drop of approximately 5 mm in diameter from a height of 757 mm to impact on a deep-liquid pool ($H_0 = 141$ mm). The resulting free surface disturbances are recorded with the stereo PLIF system in exactly the same configuration as in the first test case, with a domain size of $z_d \approx 62$ mm, a plane spacing of $\Delta z = 3$ mm, and a camera separation angle of $2\alpha = 50^\circ$. The measurements are timed to obtain two impact events in one recording. However, the droplet release time is not synchronized with the recording time.

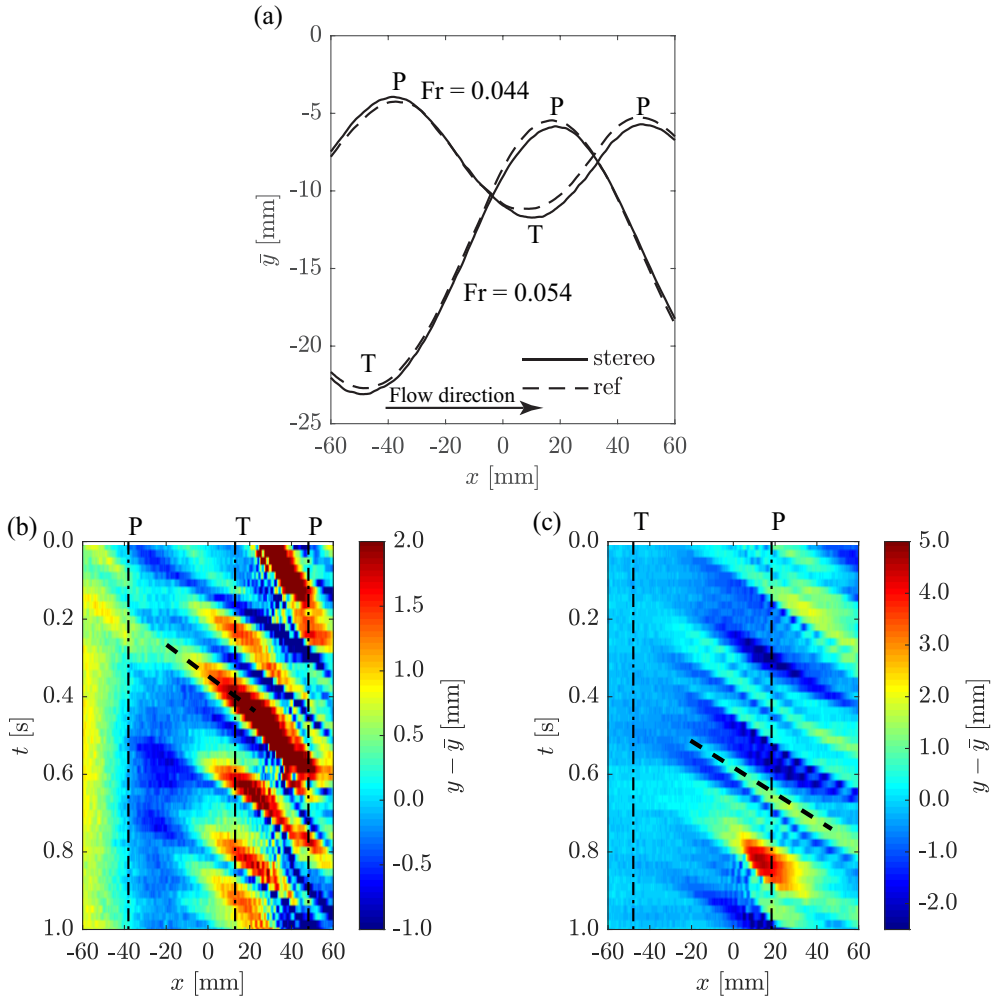


Figure 2.10: (a) The temporal average ($\bar{y}(x, 0, t)$) of the free surface wave at $z = 0$ for the stereo and reference measurement, which shows an average difference of $\overline{\bar{y}_{stereo} - \bar{y}_{ref}} = 0.1$ mm, a maximum difference of 0.45 mm, and a standard deviation of $\sigma_1 = 0.45$ and $\sigma_2 = 0.28$ mm. Space-time diagrams of the disturbance height ($\eta(x, 0, t) = y - \bar{y}$) showing the growth and decay of disturbances on the free surface wave along $z = 0$ mm for (b) $Fr = 0.044$ and (c) $Fr = 0.054$. The location of the wave trough (T) and peak (P) are indicated. The thick dashed-lines in (b) and (c) (---) indicates the velocity of a disturbance wave crest ($c_{p,1} \approx 24.7$ and $c_{p,2} \approx 29.7$ cm s $^{-1}$).

The free surface disturbances resulting from the droplet impact are clearly observed in the animation (Movie 4). Three instantaneous snapshots of the ring waves, generated by the second impact, are shown in Fig. 2.11(a-c). The two markers indicate the locations where time series are extracted, as shown in Fig. 2.11d.

The first time instance (t_1) is approximately 228 ms after the droplet impact at $\vec{X}_p \approx (-60.0, 0.0)$ mm (Fig. 2.11a). The maximum free surface disturbance $\eta(x, z, t) = y - \bar{y}$ is limited to ± 1.5 mm to remove the unphysical amplitude introduced by interference of either the incoming water drop or the rebounding liquid jet with the light-sheet.

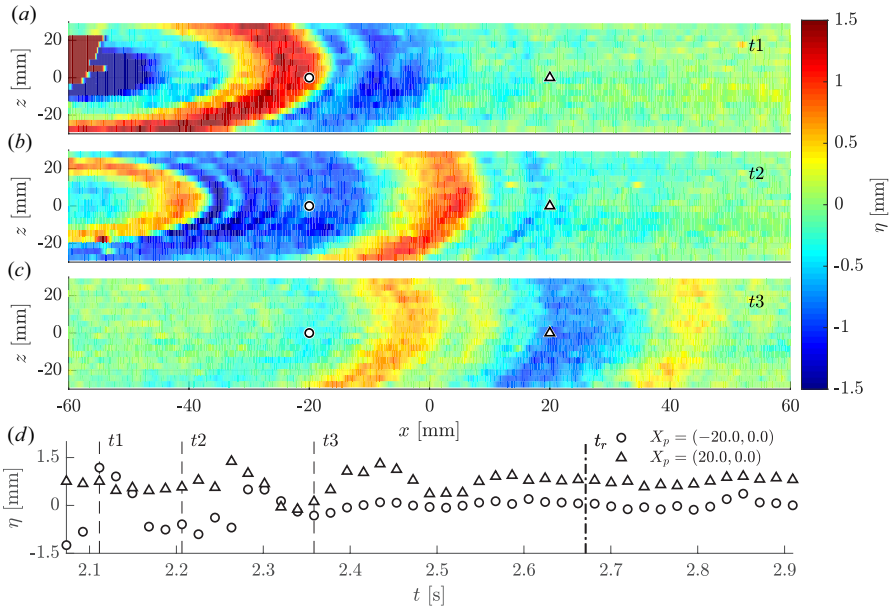


Figure 2.11: Instantaneous free surface height ($\eta(x, z, t) = y - \bar{y}$), with \bar{y} the temporal mean, for a droplet impact (a-c) denoted by t_{1-3} . The image shows spreading concentric waves. The temporal development for the points (○, △) at, respectively, $\vec{X}_p = (-20.0, 0.0)$ mm and $\vec{X}_p = (20.0, 0.0)$ mm, are shown in (d). The points of (△) are for clarity shifted by $y = 0.75$ mm. The dashed lines (---) indicate the time instance (t_{1-3}) of the instantaneous free surface heights (a-c). The dash-dotted line (-·-·) indicates the time (t_r) at which reflected free surface disturbances are observed.

At the second time instance (t_2), the marker (○) is located in the trough of the first wave train (Fig. 2.11b). The small amplitude and short wavelength waves preceding the second wave train are also observed. The marker (△) observes the small wavelength waves preceding the first wave train. Furthermore, the second wave train generated by the droplet rebound is observed in the instantaneous snapshot of the free surface height.



Finally, the third time instance (t_3) shows clearly the amplitude decay (Fig. 2.11c), as energy is conserved while the front and back group velocity diverge. The amplitude decay is proportional to time as $\eta \propto t^{-1/2}$ (Whitham, 1999).

A space-time diagram displays the free surface variation along the center line ($z = 0$ mm) of the measurement domain, which is used to estimate the local phase velocity (c_p) (Fig. 2.12). The minimum group velocity ($c_{g,\min}$) can, however, not be estimated according to Moisy et al., 2009, as the wave amplitude is below the measurement accuracy of the current stereo-PLIF configuration.

The local phase velocities of the wave crests, resulting from the droplet impact and rebound, are estimated as $c_p \approx 27.5$ cm s⁻¹ using the space-time diagram in Fig. 2.12. The local phase velocity is larger than the minimum phase velocity for surface waves $c_{p,\min} = (4g\gamma/\rho)^{1/4} = 23.1$ cm s⁻¹ with a wavelength at minimum phase speed of $\lambda_{p,\min} = 2\pi\sqrt{\gamma/(\rho g)} = 17.3$ mm. The wavelength of the surface waves, determined as the distance between the first peak and trough at t_3 (Fig. 2.11c), is approximately $\lambda \approx 44$ mm. The observed waves are deep-water gravity waves ($\lambda < H_0/2$) for which the local phase velocity $c_p = \sqrt{(g + \gamma\rho^{-1}k^2)/k} \approx 28.1$ cm s⁻¹ is comparable to the local phase velocity estimated from the space-time diagram shown in Fig. 2.12.

After, approximately, $t_r \approx 2.6$ s another free surface disturbance occurs (Fig. 2.11d and Fig. 2.12). This free surface disturbance is induced by the reflection of the initial wave train from the side walls of the channel. The reflected wave traveled a distance of $z \approx 600$ mm during $t_r \approx 2.6$ s, which corresponds to a local phase velocity of $c_p \approx 23$ cm s⁻¹. This local phase velocity is close to the minimum phase velocity ($c_{p,\min}$) of surface gravity waves.

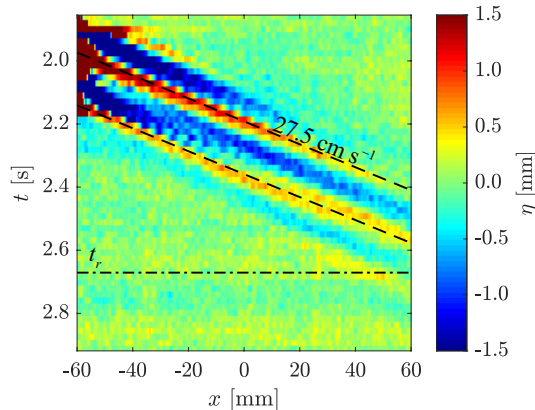


Figure 2.12: Space-time diagram of the free surface height ($\eta(x, 0, t) = y - \bar{y}$) along $z = 0$ mm, as shown in Fig. 2.11(a-c). The local phase velocity ($c_p = 27.5$ cm s⁻¹) of the two wave crests, generated by the droplet impact and rebound, are indicated with two dashed lines (---), and the interference resulting from the reflected wave is shown by the dash-dotted line (-·-·) at t_r .

A skew is introduced in the two-dimensional free surface measurements ($\eta(x, z, t)$), as is clearly observed in Fig. 2.13a. The scanning system acquires line measurements over the z -coordinate with a temporal spacing of $\Delta t = 1$ ms. In the current example, there are $N_p = 19$ light sheet locations. The difference between the first and last measurement plane is significant (18 ms). Based on the local phase velocity, this introduces a relative displacement of $\Delta x = c_p(\Delta t N_p) \approx 5.2$ mm. The measurements are therefore non-instantaneous, as the measurement time is too large which introduces a significant displacement.

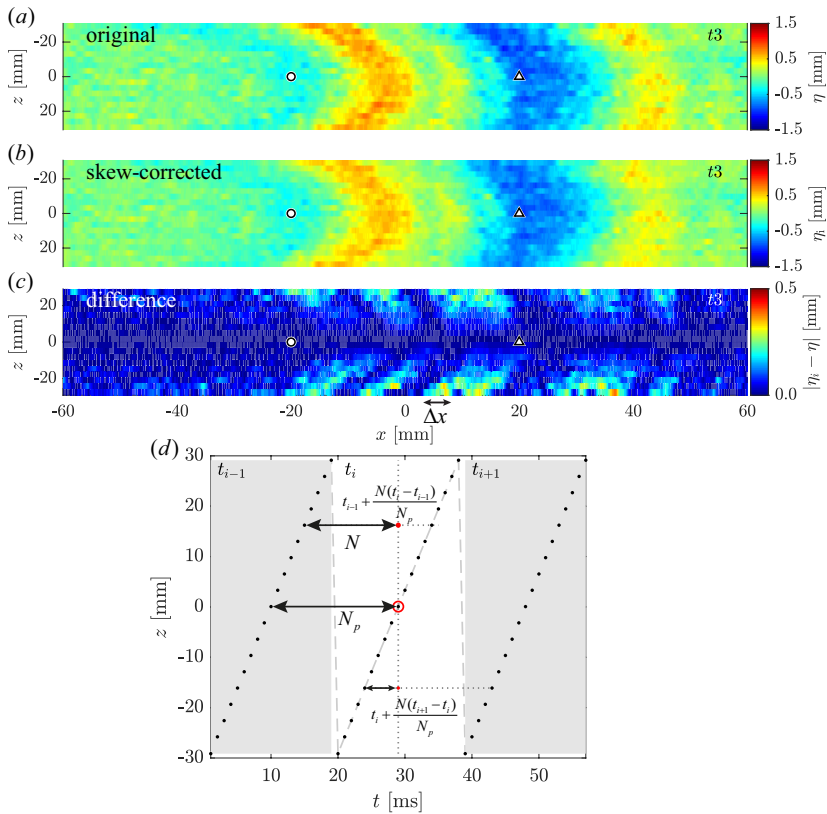


Figure 2.13: Temporal interpolation to reduce the skew introduced by scanning the three-dimensional domain. (a) Instantaneous free surface height ($\eta(x, z, t) = y - \bar{y}$), with \bar{y} the still-water level, for a droplet impact. (b) Skew-corrected instantaneous free surface height ($\eta_i(x, z, t) = y_i - \bar{y}_i$). (c) Absolute difference between original (η) and interpolated data (η_i). (d) Method used to interpolate data to common time (t).

Temporal interpolation can be applied to reduce the skew (Wellander et al., 2014) (Fig. 2.13d). The instantaneous free surface height (Fig. 2.13a) is interpolated to the center plane time (t), where a linear change in amplitude is assumed (Fig. 2.13b). The absolute difference between original (η) and interpolated (η_i) data shows an amplitude deviation of $|\eta_i - \eta| \approx 0.3$ mm with a horizontal shift of $\Delta x \approx 2.5$ mm (Fig. 2.13c). The horizontal shift corresponds to the displacement based on the local phase velocity, with the time over half the domain size $\Delta t = N/f = 9/1000 = 9$ ms and local phase velocity $c_p = 27.5$ cm s⁻¹ as defined in Fig. 2.12.

2.4 CONCLUSION

This chapter presents a scanning stereo-PLIF measurement system. The measurement system uses a stereo-camera set-up with a self-calibration procedure adapted for free-surface flows. Two-dimensional free surface height measurements can be acquired with a temporal resolution of 19 ms ($f = 53$ Hz), limited only by the available scanning equipment (1 kHz rate).

To the best of our knowledge, this system is unique as it allows us to measure time-dependent two-dimensional free surface height ($y(x, z, t)$) with disturbance amplitudes of $\eta \approx 0.2$ mm, over a domain height L of 100 mm. The accuracy with respect to the domain height (L) is high (0.2 %). On the other hand, accuracy with respect to the wave height is 12 %, which is comparable with the accuracy of other *projection*-based approaches (Table 2.1). The temporal resolution is lower than other *projection*-based approaches, but the temporal resolution is reduced in favor of the span wise resolution with currently 19 measurement planes at a span wise spatial resolution of $\Delta z \approx 3$ mm. The stream wise spatial resolution is high ($\Delta x = 0.1$ mm) compared to *correlation*-based approaches.

The temporal resolution is currently limited as is evident from the introduced skew, but results can be skew-corrected with temporal interpolation. Furthermore, the technique is versatile in its application. Therefore, the stereo-PLIF technique shows promise in the reconstruction of small amplitude variations over large two-dimensional surfaces with minimal influence on fluid properties.

3

EXPERIMENTAL INVESTIGATION OF WAVE TIP VARIABILITY OF IMPACTING WAVES

This chapter presents an experimental study on the variation in wave impact location and present a mechanism for the development of free surface instabilities on the wave crest for repeatable plunging wave impacts on a vertical wall. The existence of free surface instabilities on an impacting wave is well known, but their characteristics and formation mechanism are relatively unknown. The development of the global wave shape is measured using a visualization camera, whereas the local wave shape is measured with an accurate stereo-PLIF technique. A repeatable wave is generated with negligible system variability. The global wave behavior resembles that of a plunging breaker, with a gas pocket cross-sectional area defined by an ellipse of constant aspect ratio. The variability of the local wave profile increases significantly as it approaches the wall. The impact location varies by approximately 0.5% of the wave height or more than a typical pressure sensor diameter. Additionally, the wave tip accelerates to a velocity of $1.5\sqrt{gh_0}$ compared to the global wave velocity of $1.2\sqrt{gh_0}$. The difference in impact location and velocity can result in a pressure variation of approximately 25%. A mechanism for instability development is observed as the wave tip becomes thinner and elongates when it approaches the wall. A flapping liquid sheet develops that accelerates the wave tip locally and this triggers a spanwise Rayleigh-Taylor instability.

This chapter is based on: M. van Meerkerk, C. Poelma, B. Hofland, J. Westerweel, "Experimental investigation of wave tip variability of impacting waves", *Physics of Fluids*, 32, 082110, 2020

3.1 INTRODUCTION

In recent years, the liquefied natural gas (LNG) market showed significant growth with an increased demand for floating liquefaction facilities, storage facilities, and shipping solutions. Furthermore, LNG is proposed as an alternative shipping fuel, especially with the prospect of stricter emission standards (Aronietis et al., 2016). New challenges arise with the widespread use of LNG, such as the growth in bulk capacity of containment systems, trading routes with extreme weather conditions, and the use of lower filling levels (Delorme et al., 2009). Lower filling levels evidently lead to an increase in extreme impact events, which have the potential to cause structural damage (Buchner et al., 2007; Peregrine, 2003). Wave impact events are the basis of these extreme loads, which requires a fundamental understanding of wave impacts before studying increasingly complex phenomena (Ancellin et al., 2018a).

The study of wave impacts on a wall has been an active area of research for decades (Bagnold, 1939; Hattori et al., 1994; Blackmore et al., 1984; Bullock et al., 2001; Cuomo et al., 2010; Wang et al., 2018). Moreover, the impact of waves upon structures is relevant for many fields such as ocean, coastal, and maritime engineering. Bagnold (1939) already showed significant variation of the wave impact pressure for carefully repeated wave impact experiments. The generation of repeatable waves is not trivial. Small changes in the input parameters, such as the water depth, the wave generation method, and even the weather conditions (for large-scale outdoor experiments), results in significant variability of the impact pressure (Hofland et al., 2010; Kimmoun et al., 2010). On the other hand, the pressure impulse (i.e., the integral of pressure over time) is far more repeatable and is used to model and scale the pressure of wave impact experiments (Cooker et al., 1995; Almeida et al., 2020; Cuomo et al., 2010; Bullock et al., 2001; Ghadirian et al., 2019). In recent years, the study of liquid sloshing (Y. K. Song et al., 2013; Bogaert et al., 2010; Lafeber et al., 2012a; Lafeber et al., 2012b; Z. J. Wei et al., 2015) and slamming on both wave energy converters (Y. Wei et al., 2016; Henry et al., 2015; Renzi et al., 2018) and floating offshore structures (Buchner et al., 2007) has received considerable attention. The peak impact pressure is especially relevant in these applications (Buchner et al., 2007; Peregrine, 2003).

A number of reviews have been published both on extreme wave impact events and sloshing. For example, the effect of liquid sloshing impacts has been thoroughly reviewed by Ibrahim (2020). A detailed review of water wave impacts on vertical walls is presented by Peregrine (2003), whereas Dias et al. (2018) present a detailed review on slamming. The impact of a wave can be divided into several elementary loading processes, such as the direct impact, the jet deflection, and the compression of the entrapped or escaping gas (Lafeber et al., 2012b). Different types of wave impact can be defined by a combination of elementary loading processes. The classification of wave impact type depends on the wave shape prior to impact, which is either classified as a slosh, a flip-through, a gas pocket, or an aerated type of wave impact (Hattori et al., 1994; Chan et al., 1988; Peregrine, 2003). For example, the flip-through wave impact has been studied in detail with and without hydro-elasticity (Lugni et al., 2006; Lugni et al., 2014). The effect of hydro-elasticity is relevant for all wave

impact types (Korobkin et al., 2017). The flip-through wave impact only occurs for a limited parameter space (Peregrine, 2003). On the other hand, the impact of a plunging breaking wave occurs for a wider parameter space and often results in a gas pocket type wave impact. The impact type can easily be identified, but scaling of wave impacts from small-scale to large-scale experiments is not straightforward.

Obtaining dynamic similarity of liquid sloshing or wave impact events is complex (Ibrahim, 2020). The elementary loading processes can be used to identify the required similarity parameters (Lafeber et al., 2012b). For example, Froude scaling can be used for the global flow, where the wave is not influenced by the presence of the impact wall (i.e., the increase in pressure in the gas pocket and increase in flow from the enclosed gas pocket) (Bogaert et al., 2010; Dias et al., 2018). The global flow displays remarkable similarities with a plunging breaking wave, which allows a comparison of the wave crest velocity (Hattori et al., 1994; Vinje et al., 1981), the wave crest trajectory (Longuet-Higgins, 1995), and the gas pocket cross-sectional area (New, 1983; Bonmarin, 1989). The gas pocket behavior *after* wave impact has been studied in detail, which shows that the enclosed gas pocket decreases in volume and starts to oscillate (Abrahamsen et al., 2011; Lugni et al., 2010b; Lugni et al., 2010a). The decrease in volume of the gas pocket after wave impact is not related to gas leakage at the wave crest (Abrahamsen et al., 2011). On the other hand, the local flow is significantly altered by the strong gas flow over the wave crest for a gas pocket type wave impact. The local flow can be altered by the surface tension of the gas-liquid interface (L. Frihat M. B. et al., 2017), the gas-liquid density ratio (Karimi et al., 2015; Karimi et al., 2016), the compressibility of the gas (i.e., the speed-of-sound) (Bogaert et al., 2010), the possibility of phase change (Ancellin et al., 2018a; Ancellin et al., 2019; Ancellin et al., 2018b), and the aeration of the liquid (Bredmose et al., 2015; Bullock et al., 2007; Bullock et al., 2001). The scaling of the local flow is not well understood, but especially the formation of ligaments and droplets are thought to be relevant for the variability in wave impact pressures (Dias et al., 2018; Lubin et al., 2019).

The global features of a wave impact on a vertical wall can be accurately represented by potential flow models (Zhang et al., 1996; Peregrine, 2003; B. Song et al., 2019; B. Song et al., 2018; Ross et al., 2019). Apart from ignoring viscous effects, these simulations generally also ignore surface tension effects, as the impact is inertia dominated (Zhang et al., 1996). The irrotational flow assumption seems to be valid, as qualitative agreement between experimental and numerical impact pressures can be obtained (Dias et al., 2018). Nonetheless, the gas phase should not be neglected, especially when the flow separates near the wave crest (Etienne et al., 2018). Furthermore, the inertia of the wave tip is small and consequently it is pushed upward where it can eventually be blown off the wave crest (Zhang et al., 1996; Ross et al., 2019). Compressible multiphase simulations are required to capture this effect (Guilcher et al., 2014; Guilcher et al., 2018; Dias et al., 2018). However, the simulations are often not able to capture the development of instabilities on the wave crest (Dias et al., 2018; Etienne et al., 2018; Fortin et al., 2020; Renzi et al., 2018).

The source of impact pressure variability in repeated wave impact experiments is thought to be the instability development on the wave crest. However, the mechanism that is responsible for the formation of these instabilities is still largely unknown (Lubin et al., 2019). An approaching plunging breaking wave that encloses a gas pocket forces a strong gas flow over the wave crest, which results in a shear force on the wave crest. The shear force of the expelled gas is often postulated to result in a Kelvin-Helmholtz type instability (Lubin et al., 2019; Fortin et al., 2020; M. Frihat et al., 2016; Karimi et al., 2016). Additionally, the wave tip of the plunging breaking wave is deflected by the strong gas flow prior to the impact on the wall (Abrahamsen et al., 2011; Firoozkoobi et al., 2017). Prior to impact, gas cushioning (i.e., the increase in pressure in front of the wave tip) can also result in deformation of the wave tip (Ross et al., 2019; Hicks, 2018; Peters et al., 2013). The wave tip deflection is shown to depend on the density ratio and the scale of the experiment (Karimi et al., 2015; Karimi et al., 2016). However, accurate measurements of the wave tip deflection have up to now not been reported.

In the present study, accurate free surface measurements at both the global and local scale were performed to investigate the source of impact pressure variability in repeated wave impact measurements. The variability in impact location of the wave crest is accurately determined and a mechanism for the development of wave crest instabilities is proposed. Both the free surface instabilities and the deflection of the wave tip are important in the context of sloshing induced loads, where also the extreme impact pressure needs to be taken into account (Buchner et al., 2007; Peregrine, 2003). The global wave behavior is shown to be repeatable for measurements that have negligible system variability. Additionally, the wave behavior prior to impact is shown to resemble a plunging breaking wave. The local flow is investigated with a stereo-PLIF technique, which shows both an acceleration and a deflection of the wave tip prior to impact. The wave tip shows a significant variation in impact location on the scale of typical pressure membrane diameters of $d \sim 1 - 5.5$ mm (Souto-Iglesias et al., 2015; Lafeber et al., 2012a). Furthermore, the development of a span-wise instability is observed. The instability on the wave crest is remarkably similar to that of a flapping liquid sheet (Villermaux et al., 2002). The length scale of the instability depends on the wave shape, density ratio, and the surface tension, which was already suggested in previous work (Karimi et al., 2016; L. Frihat M. B. et al., 2017; Guilcher et al., 2018; Guilcher et al., 2014). Additionally, the study may also provide quantitative data of the wave shape, wave velocity, and wave instability for physical and numerical model validations.

This chapter is organized as follows. The experimental setup and equipment are introduced in section 3.2. This section also introduces the experimental procedure required for the generation of repeatable waves. Thereafter, the results are introduced and discussed. First in section 3.3.1, the system variability is quantified and repeatable waves are identified. Then in section 3.3.2, the behavior of the global wave is identified. Finally in section 3.3.2, the local wave behavior is discussed and two sources of impact pressure variability are identified. The findings are summarized in section 3.4.

3.2 EXPERIMENTAL APPROACH

3.2.1 WAVE FLUME

Figure 3.1 shows the experimental facility used in this study. The measurements are performed in the wave flume of the Hydraulic Engineering Laboratory at the Delft University of Technology. The flume is 39 m long with a cross-section of $0.79 \times 1 \text{ m}^2$, and the water depth is maintained at $h_0 = 500.0 \pm 0.5 \text{ mm}$ for all measurements. The flume is equipped with a piston-type wavemaker that has a maximum stroke of 2 m. Additionally, the flume contains an active reflection compensation (ARC) system, which is designed to operate during continuous wave or wave spectrum generation. In this work, the ARC system is disabled during generation of the single focused wave. After impact of the focused wave, the system is enabled to dampen the reflected waves and to reduce the downtime between experiments.

The current method of wave generation is similar to the *large scale* tests of the Sloshel project, where the effective flume length is scaled with the length-scale (λ) of the depth-based Froude number (i.e., $\lambda = h_0/H_\lambda = 1/6$ with h_0 the current water depth and H_λ the full-scale water depth) (Lafeber et al., 2012b). A Froude scaled experiment requires a reduced effective flume length, which is obtained by placing a 20 mm thick transparent perspex wall at a distance of $L = 23.4 \text{ m}$ from the wave board (fig. 3.1). The perspex wall is attached to a frame, which is fixed to a stable concrete block (i.e., with dimensions of $0.78 \times 0.80 \times 1.00 \text{ m}^3$ and a weight of approximately 1500 kg) placed in the flume. Silicone sealant is applied at the edges of the perspex wall to make it watertight. Nonetheless, exact Froude scaling is not achieved, due to practical limitations (e.g., the camera measurement system limits the water depth to 500 mm). The Froude scaled ratio is (1 : 7.3) compared to the (1 : 6) ratio of the Sloshel experiments, which will result in a smaller wave (i.e., with a smaller gas pocket and lower wave impact height) (Lafeber et al., 2012b; Bogaert et al., 2010).

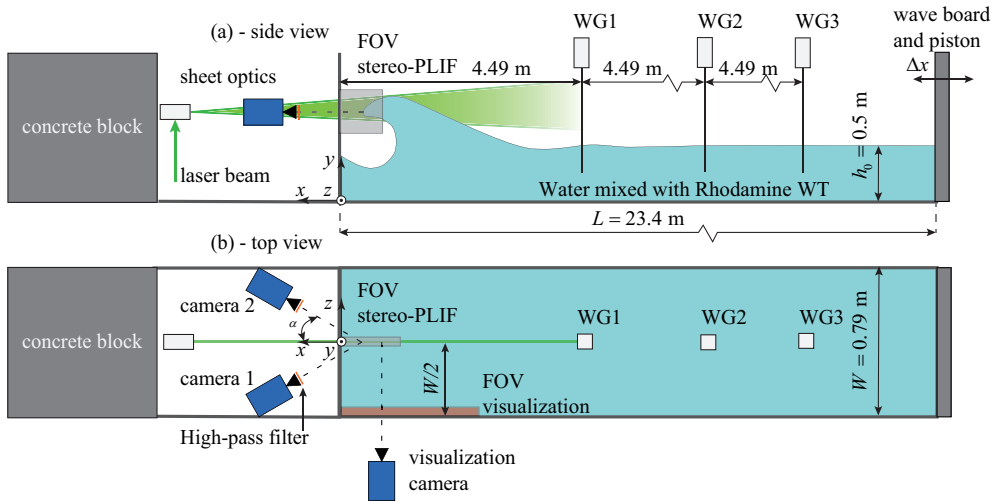


Figure 3.1: Schematic of the experimental facility. The origin of the coordinate system is located at the center plane of the wave flume on the bottom of the flume. The positive x -direction is from the wave board towards the impact wall. (a) Side-view of the wave flume. The cameras for the stereo-PLIF are aligned on a xz -plane. A vertical light sheet (xy -plane) is created at the center plane of the flume. A focused wave, generated at the wave board ($x = -L$), impacts the impact wall at $x = 0$. (b) Top view of the set-up. The visualization camera measures the global wave shape, either at the sidewall or the light-sheet location. The stereo-PLIF system measures wave crest details in a smaller field-of-view at the light-sheet location.

The flume is equipped with a control system, a data acquisition system, resistance-type wave gauges, a position sensor on the wave board, and temperature sensors for both the water and air (TSP01, Thorlabs). The wave shape is additionally determined on a global and local scale with a camera measurement system. The generation of repeatable waves is not trivial and the required experimental procedure is further detailed in section 3.2.4. The wave gauge, position sensor, and trigger signals are collected at a frequency of 100 Hz. The three wave gauges measure the surface elevation ($\eta = y - h_0$) at respectively $x/h_0 = 8.98$, 18.0, and 26.9 (fig. 3.1). The position sensor (GHM2000MD601V2 position sensor, Temposonics) records the position of the wave board (fig. 3.1).

3.2.2 WAVE GENERATION

We obtain a large gas pocket wave with a technique that focuses the wave energy in the temporal domain (Hofland et al., 2010). The wave board (fig. 3.1) generates wave groups with their own group velocity and phase speed, which results in a variety of wavelengths as shown later in figure 3.3. The wave energy of these wave groups is focused on a single location in the flume, the focal point (x_f). The focal point defines the wave shape upon impact, where a shift of the focal point results in respectively:

an aerated, a flip-through, a gas pocket, or a slosh impact (Hattori et al., 1994). The focal point also determines the angle between the wavefront and the impact wall, where a parallel front (i.e. a wave crest aligned with the impact wall) results in a high impact pressure (Bullock et al., 2007). The normalized focal point of $x_f/h_0 = 0.81$ is selected with a trial-and-error approach to obtain a large gas pocket with a parallel front, which results in a spray cloud (Bagnold, 1939).

The generation of nominal identical waves with a focusing technique is not trivial, as changes in the initial conditions, such as the water depth, are amplified by the non-linear wave focusing, which results in a different impact type (Kimmoun et al., 2010; Bagnold, 1939). The variance in impact type results from two sources of variability: the *system variability*, and the *hydrodynamic variability*. Minimization of the system variability is essential to study the hydrodynamic variability (e.g., the growth of free surface instabilities on a wave crest). The system variability (i.e., the water depth variation, piston motion variation, and residual motion) is minimized within the limitations of the experimental facility. The comparison between measurements over several days is limited due to inevitable day-to-day variations present in the current experimental facility (Kimmoun et al., 2010; Bogaert et al., 2010). The day-to-day variations are all variations related to water depth, water quality (i.e., natural accumulation of particles on the free surface), and water temperature that cannot be fully controlled in the current facility. The initial water depth variations are expected to be the most significant source of day-to-day variations, as the water depth in this facility could only be set with limited accuracy (i.e., 0.5 mm). Therefore, a single data set is highlighted, for which the differences in input parameters are carefully reported in section 3.3.1.

3.2.3 FREE SURFACE PROFILE MEASUREMENT

The wave impact upon a wall displays global and local behavior (Bogaert et al., 2010). The global wave is Froude scaled, whereas hydrodynamic variability alters the local wave behavior. The difference in length scales of the global and local waves require separate measurement systems, which are introduced in the following section.

3.2.3.1 Global wave profile

A high-speed visualization camera determines the global wave shape (fig. 3.1). This CMOS camera (Imager HS 4M, LaVision) is equipped with a 35 mm Micro-Nikkor objective with an aperture number of $f^\# = 8$. Two LED floodlights (ProBeam 170w, Noxion) provide background illumination on a diffusion plate, which for the selected aperture results in good image contrast between the background and laser light (see next section). The field of view is approximately 353 mm \times 174 mm at a magnification of $M_0 = 0.06$. The image resolution is reduced to 2016 \times 1000 pixels for a higher camera frame rate (f_{aq}) of 2.5 kHz with an exposure time (Δt_e) of 358 μ s, which is sufficiently low to avoid motion blur.

3.2.3.2 Local wave profile

A stereo planar laser-induced fluorescence (stereo-PLIF) technique measures the local wave shape at the center plane of the wave flume. This system is described in detail by Meerkerk et al. (2020a). The advantage of the stereo camera system is two-fold. For a single camera, free-surface measurements can be obstructed by liquid filaments, which is largely avoided by using a stereo-camera system. Second, the stereo camera system enables the use of a self-calibration procedure, which improves the measurement accuracy and reduces alignment errors (Meerkerk et al., 2020a).

Two high-speed CMOS cameras (Imager HS 4M, LaVision) equipped with 55 mm Micro-Nikkor objectives and a high-pass filter (OG570, Schott) are placed between the impact wall and the concrete block (fig. 3.1). The separation angle (2α) of the stereo camera system is approximately 60° , with an aperture number of $f^\# = 16$ to accommodate the large separation angle. The image resolution is reduced to 1392×1400 for a higher camera frame rate (f_{aq}) of 2.5 kHz with an exposure time (Δt_e) of $363 \mu\text{s}$. The field of view of $150 \text{ mm} \times 150 \text{ mm}$ aligns with the tip of the focused wave.

The cameras are calibrated with a two-plane dot-pattern target (Type 22, LaVision) with its center at $(x, y, z) = (-104, 730, 2) \text{ mm}$. The bottom corner of the impact wall at the center of the flume defines the origin of the coordinate system and the positive x -direction is defined from the wave board towards the impact wall, so that the wave runs with a positive velocity from $x = -L$ to the impact wall ($x = 0$) (fig. 3.1). The calibration procedure requires us to initially image a fluorescent plate to determine a mapping function at the light sheet location. In the following paragraphs, we often refer to the details of the stereo-PLIF technique described in a previous manuscript (Meerkerk et al., 2020a).

A light sheet is created from the beam of a Nd:YLF laser (LDY 304 PIV laser, Litron) and focused at the center plane of the flume. The light sheet illuminates the approaching wave, which contains a fluorescent dye at a low concentration (Rhodamine WT, Sigma-Aldrich at 120 mg m^{-3}). The static surface tension does not change at the current fluorescent dye concentration (Meerkerk et al., 2020a). The dynamic surface tension is, in some cases, altered by the presence of natural surfactants that settle on the free surface over time (i.e., dust and other natural contaminants) (Duncan et al., 1999). The dynamic surface tension is not determined in the current experiments.

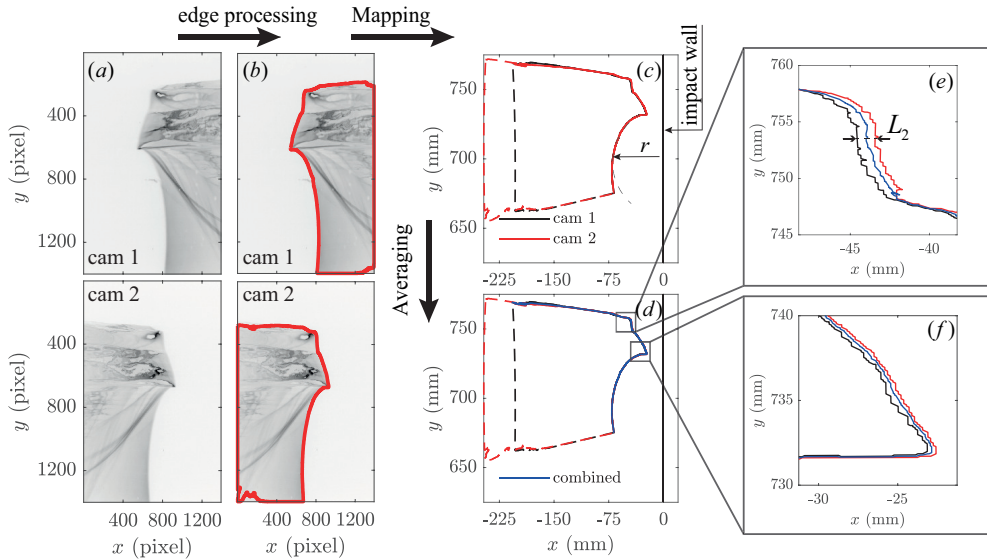


Figure 3.2: Data processing steps for the stereo-PLIF for the present measurements. (a) The original image pair from cameras 1 and 2 (Fig. 3.1). (b) The free surface profile after edge processing. (c) The profiles of both cameras mapped to world coordinates. The valid free surface profiles are indicated by a continuous line, whereas the invalid parts of the free surface reconstruction (i.e., the image borders) are indicated by a dashed line. The impact wall is located at $x = 0$ and the wave approaches the wall (i.e., from negative x which is defined to point towards the wave board). (d) The final combined profile based on the k -nearest neighbor search, with insets (e-f) showing the typical variance of the averaged profile with respect to the separate camera profiles as the distance norm of $L_2 \approx 0.5$ and $L_2 \approx 0.2$ mm for panels e and f, respectively.

The local wave shape is obtained from the image with the following processing steps (fig. 3.2) implemented in Matlab 2020. First, a 3×3 median filter reduces the effects of noise (fig. 3.2a). Then, a multi-step edge detection procedure is applied, which uses Otsu's method (Otsu, 1979). The boundary contour (fig. 3.2b) is traced after morphological operations are applied to close holes inside the wave shape and to remove small elements outside the wave shape (Gonzalez et al., 2009). After that, the contour coordinates are mapped using an updated mapping function. A disparity correction is additionally applied to improve the reconstructed profile's accuracy (Adrian et al., 2011). Then, a circle (fig. 3.2c) is fitted to the edge of the gas pocket (Pratt, 1987). Thereafter, the profiles of both cameras are combined by averaging over the k -nearest neighbor of camera 1 with respect to camera 2, with a limit of $D_l = 2.5$ mm on the point distance (fig. 3.2d) (Friedman et al., 1977). Finally, the combined profile is cropped to remove the image boundaries at the minimum y -coordinate of the circle fit and the minimum x -coordinate of both camera profiles.

The measurement accuracy of the stereo-PLIF system is determined for the initial calibration and a typical wave crest (i.e., free surface profile). First, the initial mapping function is determined with an accuracy of approximately 0.06 mm (e.g., 0.3 and 0.8 pixels for respectively the x and y -coordinate). The camera perspective results in a significant variation of the resolution (S) (Meerkerk et al., 2020a). The resolution over the x (S_x) and y (S_y) coordinate are respectively 4.9 and 13 pixels mm^{-1} . Second, a systematic error is introduced when the free surface profiles from the two cameras are combined. This systematic error is defined as the average Euclidean norm (L_2) between the combined and individual profiles. The systematic error for a typical free surface profile (fig. 3.2 e-f) is approximately $L_2 \approx 0.35$ mm (e.g., approximately 1.7 or 4.6 pixels based on respectively the x and y -coordinate of the initial mapping function). The systematic error is larger at the top of the wave crest ($L_2 \approx 0.5$ mm) where the light sheet skims over the wave surface (see section 3.3.2), which results in an increase of the measurement uncertainty. The measurement accuracy is mainly defined by the systematic error, whereas the error of the initial calibration appears to be negligible.

3.2.4 EXPERIMENTAL PROCEDURE

Nominal identical waves require a repeatable experimental procedure. The steps in the procedure are detailed in this section, which describes the residual motion reduction, water level control, and measurement procedure.

The free surface is disturbed by waves at several moments during a measurement. The waves are for example introduced when the wave board of the flume is zeroed, or when the water level is adjusted. The waves that reflect from the impact wall also disturb the free surface. This residual motion of the free surface is removed with the ARC by enabling it for 7 minutes, which based on previous experiments significantly reduces the free surface fluctuations (Novaković et al., 2020). The ARC is disabled after the allotted time, and the water is left untouched for 7 minutes. However, the longest standing wave (i.e., seiche wave) is not completely attenuated by the bottom friction, which would require an impractically long downtime between measurements (Kimmoun et al., 2010; Novaković et al., 2020). Despite this, the procedure reduces the free surface fluctuations within acceptable limits for the present experiments.

The water level is checked with a ruler before the start of a measurement. Additionally, the water level is monitored with higher precision with the visualization camera (see section 3.3.1). The resolution of the ruler is 0.5 mm, which defines the minimum threshold for the water depth change. The water level is adjusted when the threshold is exceeded, and thereafter the residual motion is reduced according to the experimental procedure described above.

The measurement procedure initiates with the start of the acquisition devices, and wave generation. These are separate systems where the programming timing unit (PTU) of the camera system is used as a master clock during the measurements. The camera and analog acquisition system are both enabled prior to wave generation.

The analog acquisition system is manually enabled and collects data from the wave-gauges and piston position sensor at a frequency of 100 Hz. Additionally, the trigger signals from both the wave generation and the camera acquisition system are recorded. The data of the analog system is matched to the master clock based on the trigger signal of the wave generation system.

The camera acquisition system acquires data at a frequency of 2.5 kHz in a ring buffer, which enables continuous recording. This ring buffer allows a remote signal to trigger the recording of the camera measurement system. The remote trigger signal is sent from a delay generator (digital delay generator DG535, Stanford Research Systems), which in turn is triggered by the wave flume.

The wave generation system is manually activated to generate a single focused wave. The wave generation system sends a trigger signal to both the camera and analog acquisition systems. Finally, the acquisition system is disabled after wave impact and the experimental procedure is repeated.

3.3 RESULTS AND DISCUSSION

3.3.1 SYSTEM VARIABILITY

On a global scale the wave is considered repeatable for the current facility when the system variability is minimal within the practical limitations. In this section the wave-gauge signal, piston motion, and still-water level are analyzed for 12 selected measurements. These 12 measurements are part of a set of 32 measurements, obtained over multiple days. The analyzed measurements were performed on the same day to avoid day-to-day system variability. The water quality (in particular the surface tension) is assumed to be constant, and the water temperature variation ($\Delta T = 0.3^\circ\text{C}$) is considered negligible.

The wave shape and wave height change significantly for small water depth variations (i.e., a water depth variation larger than 0.15% of the initial water depth is significant) (Kimmoun et al., 2010; Novaković et al., 2020). An estimate of the water depth variation is determined from samples ($N = 100$) of the still-water level that were recorded prior to each measurement. A line is fitted through the still-water level, which shows a variation in initial water depth of $\Delta h_0 = 0.08$ mm with a bias of 0.15 mm with respect to the linear fit of the still-water level. The water depth variation is lower than 0.15% of the initial water height. Therefore, the influence of the initial water height on the system variability is negligible for the measurements performed on a single day (Novaković et al., 2020).

The piston motion (x_p) and wave-gauge signal (η_{WG1}) are compared with methods commonly used to quantify the repeatability of focused waves (Bogaert et al., 2010; Hofland et al., 2010; Wang et al., 2018). The height (H) and last zero up crossing period (T) of the highest wave are determined for both the piston motion and free surface elevation (fig. 3.3). For both signals the mean (μ), standard deviation (σ), and coefficient of variation ($c_v = \sigma/\mu$) are reported (tab. 3.1) (Bogaert et al., 2010; Hofland et al., 2010). Additionally, the peak root-mean square error (RMSE) is defined (Wang et al., 2018). Last, the coefficient of variance for the energy of the piston motion signal ($E_s = \int_{t_0}^{t_1} |x(t)|^2 dt$) is computed (Bogaert et al., 2010).

Table 3.1: The system variability is based on repeatability estimates of the piston motion (x_p) and the free surface elevation at wave gauge 1 (η_{WG1}). The free surface elevation without outliers (η_{WG1}^*) is also reported.

Case	Number of measurements	E_s	H			T		
		($\text{mm}^2 \text{ s}$)	(mm)			(s)		
		c_v (%)	μ	σ	c_v (%)	μ	$\sigma \times 10^{-3}$	c_v (%)
x_p	12	0.4	213.1	0.21	0.10	2.1	0.30	0.01
η_{WG1}	12	1.2	227.9	2.1	0.92	1.41	0.74	0.05
η_{WG1}^*	9	1.0	229.1	0.21	0.09	1.41	0.58	0.04

The period of the highest wave is repeatable for both the piston motion and free surface elevation, with an insignificant standard deviation compared to the acquisition frequency (i.e., $\Delta t = 10$ ms). The period of the highest wave is reduced as the wave steepens.

The piston motion is also highly repeatable, with a negligible standard deviation compared to the resolution of the acquisition system (i.e., 0.21 mm is equivalent to 2.1 mV). The variation in the signal power (E_s) is also insignificant (tab. 3.1).

Figure 3.3 shows the free surface elevation signal for the reported experiments, where the insets highlight the small amplitude (b) and large amplitude (c) free surface waves. Colors represent the different repetitions of the experiment. The numbering is kept consistent within the larger experimental campaign for data re-usability. The standard deviation of the peak height is not negligible compared to the free surface elevation (η_{wg}) and outliers (dashed lines) can easily be identified for the highest wave (fig. 3.3 c). The outliers are based on the median absolute deviation (MADe). A significant reduction in the standard deviation and coefficient of variation of the wave height are obtained with only the repeatable waves (η_{wg}^*). A possible source of the wave height variation is a remaining free-surface fluctuation (i.e., a seiche wave) at the start of the measurement (Novaković et al., 2020). The coefficient of variation of the piston motion is low and does not depend on the repeatable and non-repeatable waves. The combined repeatability measures indicate insignificant system variability and, consequently, the global wave is expected to be well repeated (Bogaert et al., 2010; Hofland et al., 2010; Kimmoun et al., 2010).

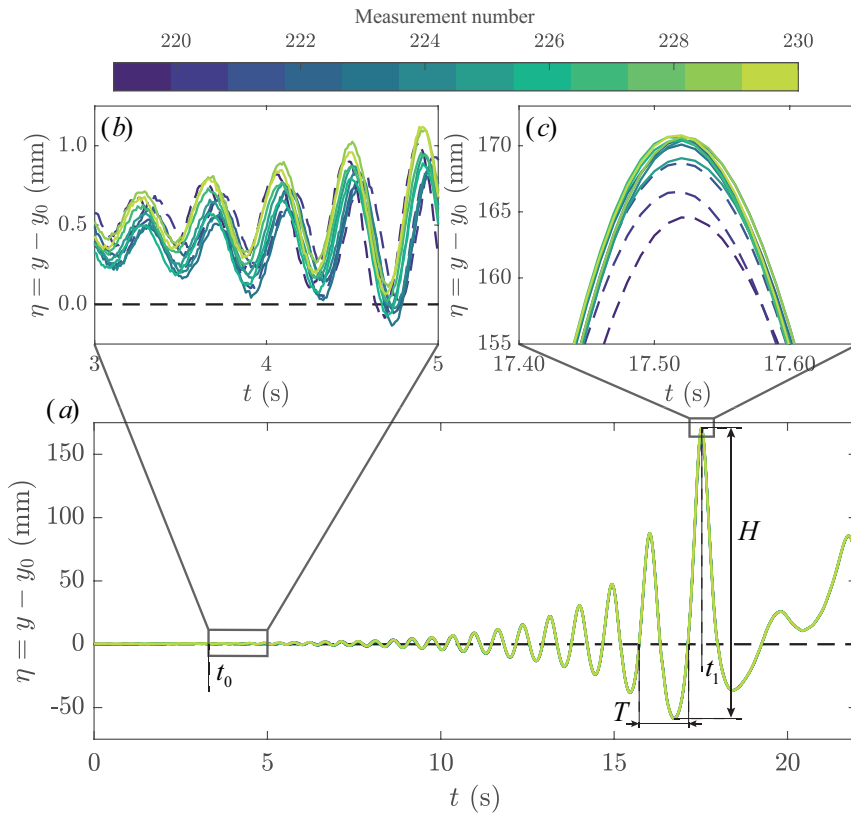


Figure 3.3: (a) The wave elevation signal at wave gauge 1 (WG1 in fig. 3.1) is shown for 12 measurements obtained on the same day with an initial water depth of $h_0 = 500$ mm. The still-water level (y_0) of the wave gauges is subtracted from surface elevation signal (y). The amplitude (H) and period (T) of the highest wave are also defined. The continuous lines show repeatable measurements, whereas dashed-lines indicate outliers identified based on the amplitude of the highest wave. The difference between repeatable and non-repeatable (i.e., outlier) waves is highlighted in panels b and c, where a zoom in of the free surface elevation signal is shown for respectively the short and long waves.

3.3.2 GLOBAL WAVE BEHAVIOR

The analysis of the system variability indicates that the wave generation is repeatable for the 9 selected waves from a set of 12 measurements (tab. 3.1). Now, the images obtained with the visualization camera are analyzed to compare the repeatability of the generated waves. First, the global wave behavior is visually compared. Then, the shape of the gas pocket and the location of the wave tip are determined. Finally, the cross-sectional area of the gas pocket in the plane of observation is determined and an estimate of the local gas velocity at the wave crest is derived.

3.3.2.1 Visual comparison

The qualitative repeatability is determined with a visualization camera by comparing differences in image intensity (L. Frihat M. B. et al., 2017). Here the global wave shape, as obtained with the visualization camera, is compared for two typical measurements (M225 and M228) shown in panels (a) and (b) of figure 3.4. The red (M225) and cyan (M228) highlights show the difference in image intensity between both measurements at two time steps $t = -28.0$, and $t = -16.0$ ms with respect to the time of impact ($t = 0$ ms). The wave crest development for a typical wave (i.e., M225) can be observed at different time steps in the supplemental electronic material (see Movie 3.1).

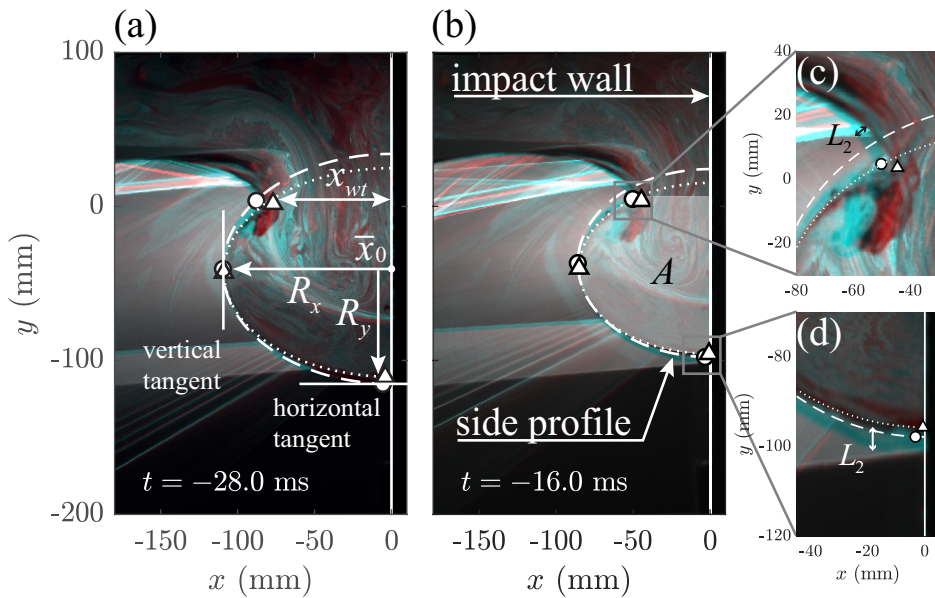


Figure 3.4: (a)-(b) The back-projected side-view images of two nominal identical waves are superimposed at two time steps, where differences in intensity are indicated in red (M225) and cyan (M288). The colors highlight the variance in wave shape. The striations behind the wave crest result from refraction of the light sheet at the wave crest, and are measure of the subpixel variations present on the wave crest. Additionally, the semi-ellipse fit of the gas pocket is shown for M225 (dotted line) and M228 (dash-dotted line). The wave crest (\bar{x}_{wt}), ellipse center (\bar{x}_0), and the ellipse's semi-major and semi-minor axes (R_x, R_y) are defined in window (a). The cross-sectional area (A) of the gas pocket is defined in panel (b). The panels (c) and (d) show the intensity variation between waves, with respectively an averaged free surface variation of $L_2 \approx 5.0$ mm and $L_2 \approx 3.8$ mm.

The free surface is determined at the side-wall of the wave flume, where the width of a color band (i.e., red and cyan areas) is a measure of the differences in global wave shape. The width is estimated at the tip of the wave crest (fig.3.4c) and the bottom of the trough (fig.3.4d). The difference in global wave shape is on average

$L_2 \approx 4.4$ mm for $t = -16.0$ ms at the indicated regions. Although, these results must be interpreted with care, as variations in image intensity arise from multiple sources (e.g., laser-intensity fluctuations, a wetted or unwetted side wall). The overall shape of the global wave is quite similar. However, a more detailed analysis should be performed, as the variability in impact pressure is also related to small variations in gas pocket shape (Hattori et al., 1994).

3.3.2.2 Cross-sectional shape of the gas pocket

Initially, the focused wave resembles a plunging breaker, which is used to define the gas pocket shape. The area of the gas pocket is typically reported at the moment of impact or during the compression cycle, where the gas pocket cross-sectional area is either fitted with a semi-ellipse (Lugni et al., 2010b) or as a semi-circle (Wang et al., 2018; Bogaert et al., 2010). The area underneath a plunging breaker can also be approximated by an ellipse with a constant aspect ratio (New, 1983), but the accuracy of this ellipse fit is a subject of debate for a plunging breaker (Bonmarin, 1989). Here the gas pocket cross-sectional area is fitted with a semi-ellipse constrained to the impact wall.

The parameters of the ellipse (i.e., the semi-major axis R_x , the semi-minor axis R_y , and the center-point \bar{x}_0) are defined in panel (a) of figure 3.4. The ellipse semi-axes are manually determined using the images of the visualization camera, where the ellipse axes tend to correspond to the horizontal and vertical tangent of the gas pocket (fig. 3.4a-b). The ellipse center is defined by the x -location of the wall and additionally the y -location of the vertical tangent. The location of the tangent (i.e., vertical and horizontal) is manually estimated. The manual estimate is improved by detecting the maximum intensity gradient over a line perpendicular to the tangent.

The semi-ellipse fit overlaps with the cross-sectional area of the gas pocket of the visualization camera as shown in panels (a) and (b) of figure 3.4. However, small differences are observed near the wave crest and in the trough of the gas pocket (fig. 3.4). The manual selection accuracy over repeated evaluations is approximately 0.3 mm and 2.2 mm (i.e., equivalent to 0.5 and 5.4 % of the semi-major and semi-minor axes for a typical gas pocket at the moment of impact) for respectively the R_x and R_y axes. The uncertainty in the R_y component is larger due to the reduced image intensity at the horizontal tangent of the gas pocket (fig. 3.4b). This results in a variation of R_y over repeated experiments as shown in figure 3.5.

The semi-major and semi-minor axes are approximated by a linear function (fig. 3.5). The upward motion of the wave trough (i.e., the contact point of the wave and the wall) is defined by the derivative of the semi-minor axis (\dot{R}_y), and is approximately constant at -1.23 m s $^{-1}$. The wave speed is defined by the derivative of the semi-major axis (\dot{R}_x) and is conjectured to change. The wave speed is initially 2.38 m s $^{-1}$ for $-80 \leq t \leq -40$ ms, but it decreases to 2.00 m s $^{-1}$ for $-40 \leq t \leq 0$ ms. The averaged wave speed is 2.18 m s $^{-1}$, which is approximately equal to the shallow water phase speed ($\sqrt{gh_0} \approx 2.21$ m s $^{-1}$). The aspect ratio of the ellipse is nearly constant at $R_x/R_y = 1.6$ for $-60 \leq t \leq -20$ ms, which approximates the

aspect ratio of $\sqrt{3}$ for plunging breakers (New, 1983; Bonmarin, 1989; Chen et al., 1999). The velocity ratio is also relatively constant, which results in a velocity \dot{R}_y of approximately $\sqrt{gh_0/3}$.

The repeatability of the global wave is determined from the ellipse fit. First, the systematic error with respect to the linear fit is defined per measurement, which is on average 0.8 and 3.6 mm for respectively the semi-major (R_x) and semi-minor (R_y) axes. A measure of the wave shape repeatability is the random error, which is on average 1.1 and 1.7 mm for both axis. The higher random error of the semi-minor axis is a result of the detection method. Small variations in gas pocket size are a source of variability in impact pressure (Hattori et al., 1994). However, the random error is negligible (i.e., 2.0 and 4.2 % of a typical gas pocket at the moment of impact); as such the global wave shape appears to be repeatable based on the gas pocket size.

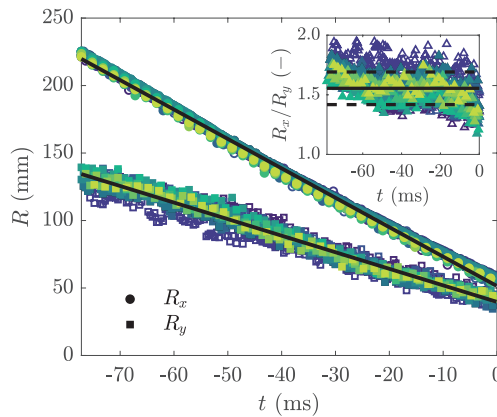


Figure 3.5: The semi-major (R_x) and semi-minor (R_y) axis of the fitted ellipse for the characterization of the observed gas pocket (see fig. 3.4) are shown, where the open markers define the non-repeatable waves of figure 3.3. The semi-minor and semi-major axis are approximated by a linear fit $R_y = -1.23t + 39.7$ and $R_x = -2.18t + 51.4$. The inset shows a nearly constant aspect ratio of $R_x/R_y \approx 1.6 \pm 0.1$ (for $-60 \leq t \leq 20$ ms).

3.3.2.3 Wave tip

The development of the plunging wave tip is determined from the images of the visualization camera. The wave tip is formed when the gradient of the free surface profile is large, which results in a pressure gradient in the fluid that accelerates a liquid jet horizontally (Longuet-Higgins, 1995). The wave tip becomes thinner and longer, while following a ballistic trajectory (Longuet-Higgins, 1995). In the present measurements the wave tip does not follow a ballistic trajectory, as the cross flow at the wave tip results in a drag force that counteracts the gravitational force.

The wave tip trajectory is determined with the detection method previously used for the ellipse axes. The tip coordinate is determined for every fifth time step ($\Delta t = 2.0$ ms), which is sufficiently small to determine the global wave tip behavior.

The wave tip is detected with an accuracy of approximately 0.96 and 0.31 mm for respectively the x and y -coordinate of the wave tip. Figure 3.6 shows the wave tip trajectory for both the x (x_{wt}) and y -coordinate (y_{wt}).

The wave tip trajectory appears to be nearly linear for both coordinates (fig. 3.6). The residual error of the linear fit is 3.6 and 2.1 mm for respectively the x and y -coordinate, which indicates repeatable wave-tip behavior. Furthermore, there is no clear distinction in wave tip behavior between the previously defined repeatable and non-repeatable waves.

The components of the wave tip velocity are $\dot{x}_{wt} = 2.67 \text{ m s}^{-1}$ and $\dot{y}_{wt} = 0.1 \text{ m s}^{-1}$, which results in a rising wave tip as it approaches the impact wall. The ratio of wave tip and global wave velocity $\dot{x}_{wt} / \sqrt{gh_0}$ is approximately 1.22, which is similar to the velocity ratio of a plunging breaker (Hattori et al., 1994). The wave tip trajectory deviates from the linear fit for $-20 \leq t \leq 0 \text{ ms}$, which indicates an acceleration of the wave tip during the final stage before impact. The acceleration of the wave tip is approximately $a \sim 100 \text{ m s}^{-2}$ based on $a \sim (2\Delta x) / \Delta t^2$ with $\Delta x \approx 15 \text{ mm}$ with respect to the linear fit of x_{wt} and $\Delta t \approx 18 \text{ ms}$ for $-19.2 \leq t \leq -1.2 \text{ ms}$ (fig. 3.6).

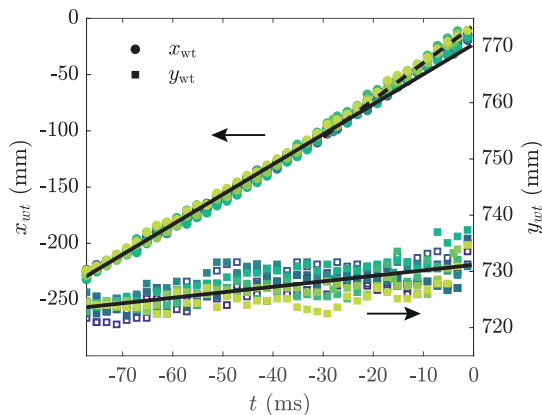


Figure 3.6: The wave tip coordinates (x_{wt}, y_{wt}) obtained with the manual fitting procedure from the visualization camera. The tip coordinate is approximated by a linear function in both $x_{wt} = 2.67t - 22.97$ and $y_{wt} = 0.10t + 731.2$. The closed markers indicate repeatable waves, based on the surface elevation data, whereas the open markers indicate non-repeatable waves.

3.3.2.4 Gas pocket cross-sectional area

Small variations in the gas pocket shape can result in impact pressure variability (Hattori et al., 1994). The gas pocket cross-sectional area is determined to define the global wave shape repeatability and estimate the local gas velocity in front of the wave crest. The variability in impact pressure due to the variation in gas pocket size is expected to be minimal, as the ellipse axis and wave-tip coordinate already

indicate a repeatable global wave behavior. The gas pocket cross-sectional area is defined as the ellipse segment *underneath* the wave crest tip:

$$A = \frac{1}{2} (\pi R_x R_y - A_s), \quad (3.1)$$

with A_s the area of the elliptical segment *above* the wave crest tip. The area of the elliptical segment is defined as follows:

$$A_s = R_x R_y \left[\arccos \left(1 - \frac{h}{R_y} \right) - \left(1 - \frac{h}{R_y} \right) \sqrt{2 \frac{h}{R_y} - \frac{h^2}{R_y^2}} \right], \quad (3.2)$$

with $h = R_y - (y_{wt} - y_0)$ the sector height of the elliptical segment (fig. 3.4). Figure 3.7 shows the calculated gas pocket cross-sectional $A - A(0)$ area, where the value at impact (A_0) is subtracted. The gas pocket cross-sectional area at impact is approximately $4.1 \times 10^3 \text{ mm}^2$ with a standard deviation of 6.5%. The power of the best fit function to the gas pocket cross-sectional area is 1.52 which is approximately $3/2$, as shown in the log-log inset of figure 3.7. Furthermore, the non-repeatable waves, based on the free surface elevation, are indistinguishable from the results for the repeatable waves.

The gas velocity at the wave crest increases as the wave approaches the wall. The incompressible gas velocity at the wave crest (V_g) follows from a control-volume attached to the ellipse

$$V_g = \frac{1}{\Delta x} \dot{A} \sim |t|^{-0.48} \sim |t|^{-1/2} \quad (3.3)$$

where $\Delta x = \dot{x}_{wt} t \sim 1.2 \sqrt{g h_0} t$ is the distance between the wave crest and the wall, and $\dot{A} = 2.64 |t|^{0.52} \sim 1.2 \sqrt{g h_0} |t|^{1/2}$ is the temporal derivative of the cross-sectional area of the gas pocket. The gas can be considered as incompressible for a Mach number ($M = V_g/c$) lower than 0.3. The gas in the cavity is incompressible for $V_g = |t|^{-1/2} \leq 0.3c$ or up to $|t| = (0.3c)^{-2} \approx 0.09 \text{ ms}$ where c is speed of sound (343 m s^{-1} at standard conditions). The gas velocity at the wave crest ranges from $3.5 \leq V_g \leq 15.8 \text{ m s}^{-1}$ for $-80 \leq t \leq -0.4 \text{ ms}$. The global wave does not appear to decelerate through compression of the gas pocket.

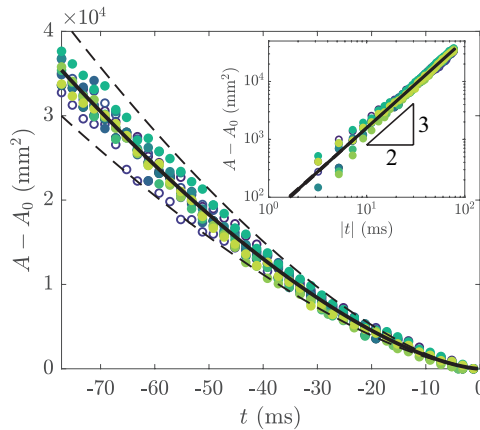


Figure 3.7: The gas pocket cross-sectional area is the area enclosed by the wave tip and the ellipse (fig. 3.4b). The gas pocket cross-sectional area is approximated by a power-law $A(t) - A(0) = 1.74|t|^{1.52}$, which is shown in the log-log inset.

3.3.3 LOCAL WAVE BEHAVIOR

The variation in impact pressure of nominal identical waves is caused by the development of free surface instabilities on the wave crest (Dias et al., 2018; M. Frihat et al., 2016; Lubin et al., 2019). Here, a stereo-PLIF system is used to accurately measure the free surface of the wave crest and to determine both the development of instabilities and the wave tip deflection. The wave crest is determined with a smaller field-of-view than the visualization camera, which results in a higher resolution and accuracy of the free surface measurements. The system enables free surface measurements in the center plane of the wave flume where side-wall effects (i.e., friction (Souto-Iglesias et al., 2015) and wetting (Novaković et al., 2020)) do not directly influence the measurement of the wave shape. First, the visualization camera and stereo-PLIF system are compared. Then, the temporal development of a local wave crest is discussed both in the context of measurement accuracy and wave tip behavior. Thereafter, the free surface profile is compared over several time steps. Finally, the wave tip and the variability due to variations in wave shape are discussed.

3.3.3.1 Global and local measurements

The stereo-PLIF data of two typical measurements (e.g., M225 and M228) are compared with the images of the visualization camera that are obtained simultaneously (fig. 3.8). The stereo-PLIF results are superimposed (continuous line) on the combined side-view images of the visualization camera by matching the origin of both coordinate systems. The ellipse fit (dashed and dotted line) is also included, which shows a qualitative agreement with the stereo-PLIF results.

The wave-crest profile at the center plane (stereo-PLIF data) is similar to that at the side wall (visualization data). The large field-of-view of the visualization camera combined with the relatively small focal length lens results in a perspective view of the wave crest, which emphasizes the spanwise differences of the wave crest (see the supplemental electronic material). For example, a liquid filament is suspended from the wave crest at the side-wall, whereas the filament is absent on the rest of the wave crest (i.e., the spanwise direction). The side-wall effects, such as friction (Souto-Iglesias et al., 2015) and wetting (Novaković et al., 2020), limit the use of side-view measurements for quantitative repeatability studies of the wave tip behavior.

The application of a stereo-PLIF system in the wave flume is not without problems. For example, the liquid exerts a large pressure on the wall when it impacts, which results in vibrations in the camera system. The vibrations can introduce a misalignment in the camera system and a self-calibration procedure is needed to correct for the misalignment.

Additionally, loss of information occurs when a free surface undulation casts a shadow. This effect is observed at the top of the wave crest where the light-sheet skims over the free surface and obstructs the backward side of the wave (fig. 3.8). The wave tip also blocks the inside of the gas pocket as it plunges over the top. A straight line results at the blocked segment, that connects the wave tip and the backward face of the gas pocket (fig. 3.8). The wave tip is accurately determined by the light-sheet cut-off, whereas the accuracy decreases at the wave top.

The stereo-PLIF system enables a quantitative comparison of repeated measurements, whereas the side-view camera only enabled a qualitative comparison. A zoom of the free surface profile shows the difference between two selected measurements M225 and M228 (fig. 3.4 panels c and d). The averaged difference between the free surface profiles as determined by the stereo-PLIF measurements is $L_2 = 2.45 \pm 1.49$ mm over the entire field-of-view. The difference was previously determined to be $L_2 = 4.4$ mm for $t = -16.0$ ms based on the visualization camera. The quantitative difference determined with the stereo-PLIF measurements is lower, even for a later time step. The stereo-PLIF and visualization measurements show that the wave is repeatable on a global scale.

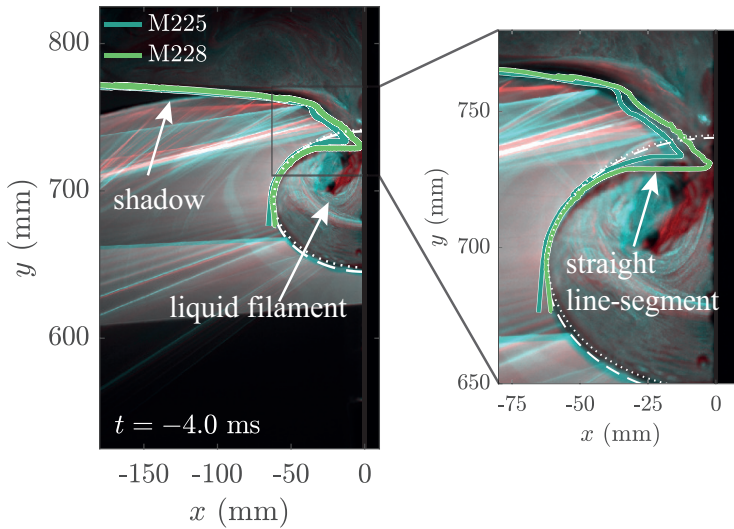


Figure 3.8: The side-view images of two nominal identical waves are superimposed for $t = -4.0$ ms and combined with the free surface profile from the stereo-PLIF measurement (continuous line). The ellipse fit from the visualization camera is also included. The refraction of the light sheet at the wave crest results in striations. These striations present a sub-pixel measure of the wave crest variability. However, they are neglected when comparing the visualization and stereo-PLIF measurements. (b) A zoom on the wave crest shows the difference between both waves and the formation of liquid filaments at the side-wall.

3.3.3.2 Temporal development

Figure 3.9 shows the temporal development of the free surface for a typical case (M225) at two different time steps, which show the local ($\Delta t = 0.8$ ms) and detailed ($\Delta t = 0.4$ ms) free surface behavior. The *local wave behavior* shows the displacement of a small amplitude *liquid jet*, which is initially ejected from the wave crest (e.g., outside of the field-of-view of the stereo-PLIF measurements) as shown in the supplemental electronic material (e.g., see Movie 3.1). The disturbance (i.e., the *liquid jet*) is displaced to the back of the wave crest by the gas flow over the wave crest. The growth and displacement of the disturbance is continuous over time, which is indicative of the temporal consistency of the stereo-PLIF data (e.g., the initial disturbance is physically there).



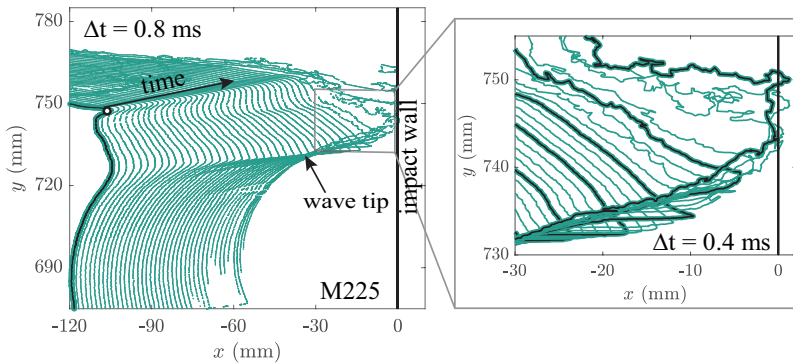


Figure 3.9: The free surface stereo-PLIF data for experiment M225 is consistent over multiple time steps ($-29.6 \leq t \leq 2.8$ ms) at a reduced temporal resolution ($\Delta t = 0.8$ ms). The marker shows the location of the *liquid jet*, that is initially ejected outside the field-of-view of the stereo-PLIF measurement (see supplemental electronic material). The zoom shows the free surface stereo-PLIF data at its actual temporal resolution for $-7.2 \leq t \leq 2.8$ ms with an increased line width for every fourth time step.

The details of the wave crest moments before impact are displayed in panel b (fig. 3.9). Initially, a liquid jet is ejected from the wave crest as the gradient of the free surface profile increases, which results in a large pressure gradient in the fluid (Longuet-Higgins, 1995; Chen et al., 1999). In this measurement a liquid jet is ejected at two times, which results in the initial disturbance (i.e., defined by the marker) and the wave tip. The wave tip of a plunging breaker follows a ballistic trajectory, but here the wave tip is displaced upwards by the air flow from the gas pocket. The gas velocity at the wave crest increases as the wave approaches the wall, which results in a wave tip that is stretched and deflected (Guilcher et al., 2014). The formation of spray (i.e., droplets) and ligaments results in a higher noise level in the stereo-PLIF data, which is observed in the last few time steps of panel b.

3.3.3.3 Local repeatability

In the previous analysis of the system variability several repeatable and non-repeatable waves were identified. The stereo-PLIF data for both the repeatable and non-repeatable waves is presented (fig. 3.10). The waves initially ($t = -28.0$ ms) overlap and the variation increases as the waves approach the wall. The variability concentrates in the vicinity of the wave tip for all waves. Initially, the formation of instabilities is not observed, both in the processed free surface profile and in the original shadowgraph of the stereo-PLIF images. However, at later stages (fig. 3.10c), the wave tip but is deflected differently. This is hypothesized to be caused by an interaction of the gas flow and interface around the wave crest.

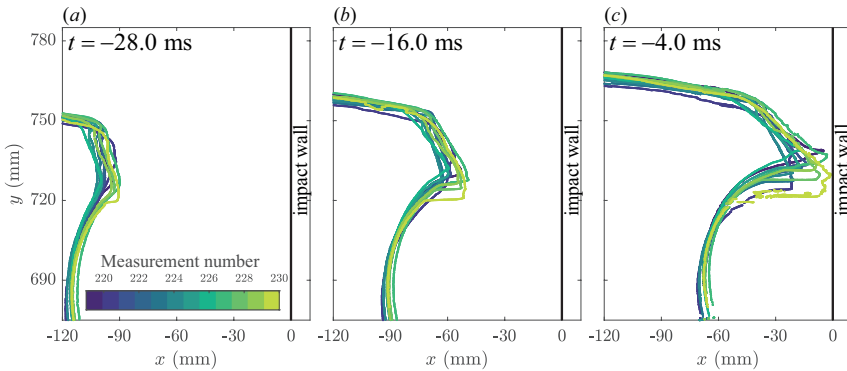


Figure 3.10: The stereo-PLIF data of all 12 measurements for three time steps, additionally a movie of the wave crest development is available as electronic supplemental material (e.g., see Movie 3.2). (a)-(b) Initially all 12 measurements tend to overlap. (c) The overlap between the different measurements reduces significantly as the waves approach the wall. The variation in free surface profile concentrates near the wave tip, which is influenced by an increase in gas velocity.

The variability of the free surface profiles is quantified. First, the difference in wave crest height ($-120 \leq x \leq -115$ mm) is determined from stereo-PLIF data at $t = -28.0$ ms (fig. 3.10 a). The standard deviation in the height of all waves is approximately 1 mm, whereas the nominal identical waves show a standard deviation of approximately 0.9 mm. The difference between both sets (i.e., repeatable and non-repeatable waves) is negligible, which is also confirmed by the initial visual overlap of all waves (fig. 3.9a). However, the variation in free surface profile is more significant at the wave crest (i.e., $730 \leq y \leq 740$ mm) for $t = -28.0$ ms with a standard deviation of approximately 3.5 mm.

A parametric representation of the free surface profiles is determined with an arc-length method. The curve is parameterized with a fixed number of elements ($N = 2500$), which results in a spacing of approximately 0.15 mm. A Euclidean distance metric (L_2) is computed from the difference between parametric curves and their respective averaged free surface profile. The distance metric increases from approximately $L_2 = 1.5$ mm at $t = -28.0$ ms, to $L_2 = 5.1$ mm at $t = -16.0$ ms, and to $L_2 = 8.0$ mm at $t = -4.0$ ms. The Euclidean norm (L_2) confirms the buildup of variability in wave shape as the wave approaches the wall. The variation is most obvious at the wave tip, whereas the global wave (i.e., the wave top and the wave trough) remain similar, which is additionally supported by the movie in the supplemental material.



Movie 3.2

The wave tip variation is further investigated to determine its possible effect on the pressure variability, where the extreme position of the wave tip is defined as the maximum x -location of the stereo-PLIF profile (fig. 3.11). First, the wave tip velocity in the x -direction $\dot{x}_{wt} = 3.31 \text{ m s}^{-1}$ is higher than previously determined from the visualization camera, $\dot{x}_{wt} = 2.66 \text{ m s}^{-1}$. A deviation from the linear fit was already observed for $-20 \leq t \leq 0 \text{ ms}$, which indicated an acceleration of the wave tip. However, the wave tip was, for $-20 \leq t \leq 0 \text{ ms}$, obscured by either the perspective of the visualization camera or the formation of a liquid filament at the side wall. The wave tip velocity in the x -direction is significantly higher $\dot{x}_{wt} \sim 1.5\sqrt{gh_0}$ for $-20 \leq t \leq 0 \text{ ms}$, which is higher than the wave tip velocity of a plunging breaker ($\dot{x}_{wt} \sim 1.2\sqrt{gh_0}$) (Hattori et al., 1994). However, the wave tip velocity in the x -direction is comparable to that of a plunging breaker that impinges on the free surface in front the wave tip (Chen et al., 1999). In the y -direction the wave tip trajectory is altered by the gas flow escaping from the gas pocket, which is obvious from the acceleration in the y -direction for $-5 \leq t \leq 0 \text{ ms}$. The wave tip trajectory in the y -direction is not comparable to that of a plunging breaking, which typically shows a ballistic trajectory (Longuet-Higgins, 1995). The wave velocity at the center plane can increase due to wave focusing of a concave wave crest (Peregrine, 2003; Wang et al., 2018) or Bernoulli suction (Peters et al., 2013), where the air pressure drops due to an increase in velocity at the wave crest.

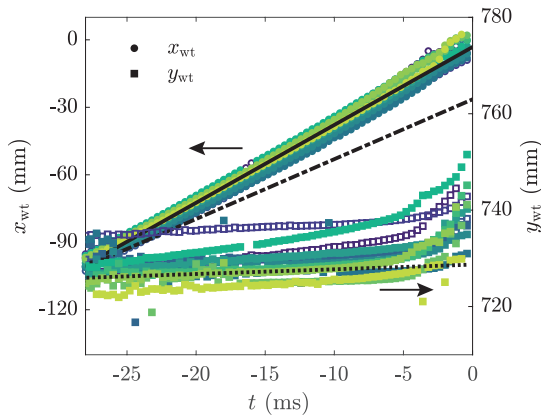


Figure 3.11: The wave tip coordinates for $-28 \leq t \leq 0 \text{ ms}$ obtained from the stereo-PLIF data. The wave tip coordinates are, initially, fitted with a linear function $x_{wt} = 3.31t - 6.36$ (continuous line) and $y_{wt} = 0.10t + 731.2$ (dotted line). The wave tip has accelerated in the x -direction compared to the data from the visualization camera (dash-dotted line). The y_{wt} coordinate deviates from the linear fit of the visualization camera for $t > -5 \text{ ms}$, which shows an acceleration of the wave tip coordinate in the y -direction.

A small amplitude wave grows on the wave crest for every wave impact, which is either caused by the large gradient of the free surface profile or by the Bernoulli suction (i.e., which is equivalent to the growth of a Kelvin-Helmholtz instability) (Longuet-Higgins, 1995; Peters et al., 2013; Ross et al., 2019). However, the growth of a Kelvin-Helmholtz instability is in this study not expected, as there are no small scale disturbances observed on both the reconstructed free surface profiles and the shadowgraphs of the original stereo-PLIF images. Nonetheless, the small amplitude wave is defined as the wave tip, that is the maximum x -coordinate of the wave crest.

The wave tip is observed to grow as it approaches the wall, which results in a thinner and longer wave tip (Longuet-Higgins, 1995). The length change of the wave tip is linear, up to approximately $t = -5$ ms, with respect to the global wave tip velocity $\dot{x}_{wt} \sim 1.2\sqrt{gh_0}$. In this time the tip stretches approximately $L \sim (1.5 - 1.2)\sqrt{gh_0}\Delta t \sim 15$ mm, which is, based on visual inspection, a good estimate of the tip length. The stretched wave tip resembles a liquid sheet.

Villermaux et al. (2002) studied the break up of a liquid sheet formed by the impact of a jet on a circular disk. The liquid sheet expands into the surrounding air, which results in a shear force that destabilizes the sheet by an initial Kelvin-Helmholtz instability. The waves that result from the Kelvin-Helmholtz instability induce an additional motion at the tip of the liquid sheet. This finite motion at the tip of the liquid sheet provides the acceleration required for a secondary Rayleigh-Taylor instability.

A similar type of mechanism is observed to trigger the development of a span-wise instability on the tip of a plunging breaking wave. The wave tip is stretched into a thin liquid sheet, which is destabilized by an initial Kelvin-Helmholtz instability. This is observed as a finite amplitude wave that forms on the wave tip for $t > -5$ ms (fig. 3.12 panels a and b). The finite amplitude wave, combined with the acceleration of the wave tip by the gas flow, results in an acceleration that triggers a Rayleigh-Taylor instability (fig. 3.12c). The wavelength of the span-wise instability (i.e., liquid filaments or fingers) is defined as

$$\lambda_{\perp} \sim (\gamma/\rho_a \dot{x}_{wt}^2)(\rho_a/\rho_l)^{1/3} \quad (3.4)$$

where $\dot{x}_{wt} = 1.5\sqrt{gh_0}$ is the wave tip velocity, γ is the surface tension of the air-water interface (72.3 mN m^{-1}), ρ_a is the gas density (1.23 kg m^{-3}), and ρ_l is the liquid density (998 kg m^{-3}) at standard atmospheric conditions (1 bar, 20°C). The spanwise wavelength of approximately $\lambda_{\perp} \sim 1$ mm agrees well with the visually observed finger spacing (fig. 3.12c).

In previous work the impact pressure variability was shown to depend on the density ratio (ρ_a/ρ_l) and the surface tension. A higher density ratio results in more well-developed (i.e., larger) liquid filaments (Karimi et al., 2015; Karimi et al., 2016). Furthermore, the free surface at the wave crest fragments earlier for lower values of the surface tension (L. Frihat M. B. et al., 2017). The increase in liquid filaments at higher density ratios and the spray formation at lower surface tension values are both captured by the span-wise wavelength of the Rayleigh-Taylor instability in Eq. (3.4). A mechanism for the development of instabilities is presented, where a flapping liquid

sheet develops into liquid-filaments (Lubin et al., 2019). Furthermore, the liquid-filaments are accelerated by the gas flow from the gas pocket and eventually break-up in small droplets due to a capillary instability of the liquid filament (Marmottant et al., 2004).

The variability in wave impact pressure is linked to the variation in wave impact location. However, the formation of liquid filaments decreases the accuracy of the wave tip detection prior to impact (i.e., close to the wall). The variation in wave impact location is, therefore, determined just prior to the formation of a flapping liquid-sheet. The impact location is determined over a small time interval ($\Delta t = 2$ ms) to improve the reliability of the measured coordinate. Figure 3.13 displays the variation in vertical wave tip location for $-6.0 \leq t \leq -4.0$ ms, which is an indication of the variation in wave impact location.

The variation in vertical wave tip location is significant on a global scale with a standard deviation of 4 mm (i.e., 0.5 % of the typical wave height). The membrane surface ($d \sim 1 - 5.5$ mm)(Lafeber et al., 2012a; Souto-Iglesias et al., 2015) of a typical pressure sensor is small compared to the variation in vertical wave tip location. Even for large ($d \sim 9.5$ mm) pressure sensor membranes the integrating effect of the surface area is not sufficient to remove all pressure variability(Y. K. Song et al., 2013). Furthermore, the physical spacing of the pressure sensor, which is typically on the order of 20 mm (Lafeber et al., 2012a; Lugni et al., 2010a), limits the possibility of detecting these small wave tip variations. The variation in vertical wave tip location is similar for the other, not reported, measurements. However, the measurements cannot be combined due to the significant day-to-day variations.

Additionally very close to the wall ($x/h_0 \lesssim 0.18$), the wave tip accelerates to about $1.5\sqrt{gh_0}$ compared to the global wave velocity of $1.2\sqrt{gh_0}$. The pressure sensor membrane is hit with either the wave tip velocity or the global wave velocity, which can result in a pressure difference of approximately 25%. The variation in pressure is similar to previous reported values for nominal identical waves.(Lugni et al., 2010a; Bogaert et al., 2010) The variation in wave tip velocity due to either wave focusing or Bernoulli suction is a source of variability in impact pressure.

The source of impact pressure variation is a combination of *system* and *hydrodynamic* variability, but even for well-repeated waves (i.e., with insignificant *system variability*) a significant wave tip variability is observed. The variability in vertical wave tip location over repeated waves on a single day is shown to be significant compared to typical pressure membrane diameters (i.e., $d_p \approx 1 - 5.5$ mm). Furthermore, this variation is observed over several other days with a similar order of magnitude. The *hydrodynamic* variability is, even when the waves are well repeated, a source of pressure variability. The shear-driven flapping motion of the liquid sheet results in significant variability in impact location, which also triggers a Rayleigh-Taylor type of instability along the spanwise direction of the wave. The presented mechanism is probably one of the many types of instabilities that can occur on the wave crest, but for the reported gas pocket impact it occurs over a significant range of wave shapes. The reported measurements can be used for physical and numerical model validation.

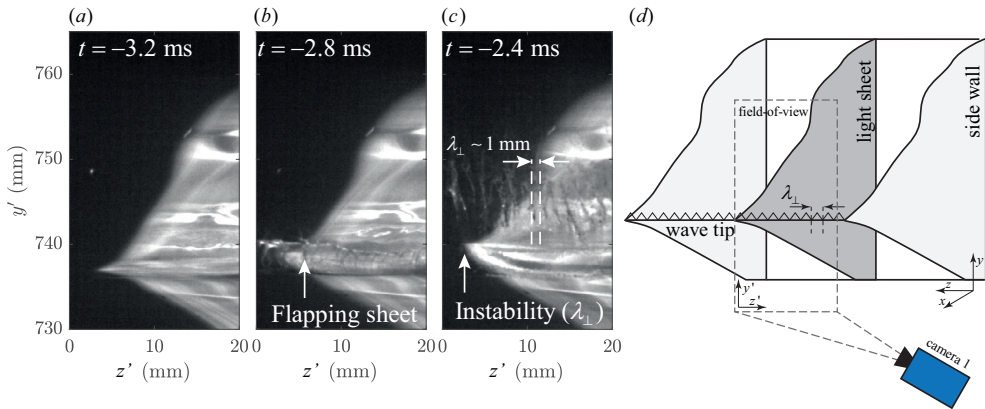


Figure 3.12: The images of camera 1 are back-projected to a plane parallel to the impact wall (a)-(c). (a) A typical wave (M221) approaches the wall and the tip elongates. (b) The elongated wave tip is destabilized by a shear instability. (c) A flapping liquid sheet develops with a spanwise wavelength (λ_{\perp}) defined by the Rayleigh-Taylor instability. (d) The images are acquired with camera 1 of the stereo-PLIF system (fig.3.1). The camera images the wave from the front at an angle with respect to the light sheet. Note the difference in coordinate system compared to that defined in figure 3.1.

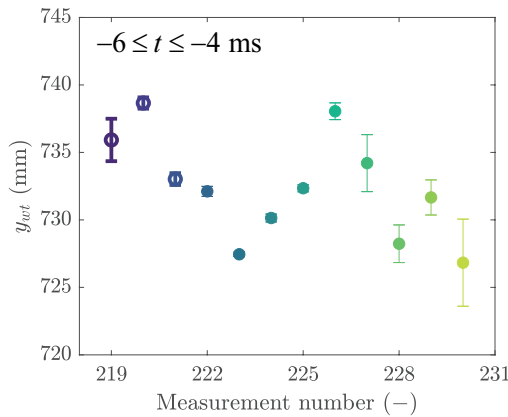


Figure 3.13: The variation in vertical wave tip location (y_{wt}) for $-6.0 \leq t \leq -4.0$ ms. The open markers are non-repeatable waves (i.e., outliers based on the surface elevation measurements) and closed markers are repeatable waves.

3.4 CONCLUSION

Repeated focused wave impacts on a vertical wall are reported. The generation of repeatable focused waves is not trivial. A limited number (i.e., $N = 12$) of the total set of 32 measurements is reported, as the day-to-day variations limit the detailed comparison. Therefore, the experimental variability (i.e., system variability) is reported in detail, which indicates that the wave generation is well-repeated over a single day. Several repeatable waves are identified ($N = 9$) based on the surface-elevation measurements. These repeatable waves are studied and compared to the remaining non-repeatable waves ($N = 3$).

The global wave behavior prior to impact is studied with a visualization camera. The cross-sectional area of a large gas pocket impact is approximated by a semi-ellipse constrained to the impact wall. The aspect ratio of the ellipse is relatively constant $R_x/R_y = 1.6$ ($\sim \sqrt{3}$), which is comparable to that of a plunging breaker (New, 1983). Initially, the global wave behavior is also comparable to that of a plunging breaker, as both have a similar wave velocity ($\sqrt{gh_0}$) and wave tip velocity ($1.2\sqrt{gh_0}$). However, the trajectory of the wave tip does not resemble that of a plunging breaker. The drag at the wave crest, due to the escaping gas velocity, partially counteracts the gravitational force. Furthermore, the wave tip accelerates to a velocity of $1.5\sqrt{gh_0}$ as it approaches the wall ($x/h_0 \lesssim 0.18$).

Moments before impact the wave tip is deflected by the strong gas flow at the wave crest. The wave tip resembles a liquid sheet, that is destabilized by an initial Kelvin-Helmholtz instability. A flapping liquid sheet develops and the acceleration of the tip triggers a Rayleigh-Taylor instability. The spanwise wavelength of the Rayleigh-Taylor instability is well approximated by $\lambda_{\perp} \sim (\gamma/\rho_a \dot{x}_{wt}^2)(\rho_a/\rho_l)^{1/3}$. The Rayleigh-Taylor instability is one of the free surface instabilities that can be a source of wave impact pressure variability. Furthermore, the flapping liquid-sheet is an indication of an instability that results in pressure variability with varying density ratio (ρ_a/ρ_l) and surface tension (γ). The other, not reported, measurements show a similar wave crest development with a flapping liquid-sheet that triggers a Rayleigh-Taylor instability.

In previous work the variability in impact pressure is often attributed to Kelvin-Helmholtz type instabilities at the wave crest (Peregrine, 2003). The current work shows that the variability in impact location is initially drag induced, with a standard deviation in impact location of approximately 0.5% compared to a wave height of 732.4 mm. The variation in impact location is large compared to typical contemporary pressure sensor sizes. A shear-driven flapping liquid sheet develops moments before impact, which delays the impact time and triggers a Rayleigh-Taylor instability that forms equally spaced liquid filaments. However, the variability in impact height already exists before the formation of the liquid filaments. The liquid filaments can impact the pressure sensor, although, it is more likely that the wave tip will directly impact the pressure sensor. The acceleration of the wave tip compared to the wave crest and global wave presents a more likely explanation of the variance in impact pressure.

4

GAS FLOW DYNAMICS OVER A PLUNGING BREAKING WAVE PRIOR TO IMPACT ON A VERTICAL WALL

This chapter presents an experimental study on the gas flow field development over a plunging breaking wave prior to impact on a vertical wall. The variability of wave impact pressure over repeated measurements is well known (Bagnold, 1939). The formation of instabilities on the wave crest are postulated to be the main source of impact pressure variability (Dias et al., 2018). However, the mechanism that results in wave impact pressure variability and the influence of the gas phase in particular are relatively unknown. The velocity field of the gas phase around the wave crest is measured with particle image velocimetry, while simultaneously the local free surface is determined with a stereo-planar laser-induced fluorescence technique. The bulk velocity between the wave crest tip and the impact wall deviates from the mass conservation estimate based on the velocity profile between the wave crest and the impact wall. This is caused by a significant increase of the local gas velocity near the wave crest tip. The non-uniformities in the seeding concentration accumulate near the wave crest tip and reduce the accuracy of the velocity measurements. However, the bulk velocity estimate is significantly improved with a fit of the velocity profile that is based on a potential flow over a bluff body. Additionally, the development of a vortex is observed and quantified for two typical cases with either a disturbance on the wave crest or a smooth wave crest. The circulation development is comparable to the formation and separation of a vortex ring, which results in a saturated vortex that separates from the wave crest (Gharib et al., 1998). Furthermore, the impact location of the wave tip and thereby the impact pressure are altered by the formation of secondary vortices. A secondary vortex locally enhances the lift and alters the trajectory of the wave crest tip.

4.1 INTRODUCTION

Stricter emission regulations result in new use cases of liquefied natural gas (LNG), which can serve as a “transition fuel” until greener options become economically viable. This growth of the LNG market brings about an increased demand for floating liquefaction facilities, storage facilities, and shipping solutions (Aronietis et al., 2016). Additional challenges arise with the widespread use of LNG, such as the requirement for lower filling levels and increased containment capacity (Delorme et al., 2009). The filling levels in LNG containment systems are currently restricted to limit the occurrence of sloshing. Sloshing increases the number of extreme wave impact events that can potentially result in structural damage (Buchner et al., 2007; Peregrine, 2003). The development of containment systems is limited by the scaling involved in the sloshing assessment methodology (Gavory et al., 2009). A fundamental understanding of wave impacts on walls is required before studying increasingly complex phenomena, such as LNG sloshing in containment systems (Ancellin et al., 2018a).

The study of wave impacts on walls has been an active area of research for decades (Bagnold, 1939; Hattori et al., 1994; Blackmore et al., 1984; Bullock et al., 2001; Cuomo et al., 2010; Wang et al., 2018). A wave impact on a wall often results in a high impact pressure, that varies even in carefully repeated wave impact experiments (Bagnold, 1939). The variability of the impact pressure increases with small variations in the input parameters, such as the water depth, the piston motion, and even the surrounding atmospheric conditions (Hofland et al., 2010; Kimmoun et al., 2010). In contrast, the pressure impulse (i.e., the integral of pressure over time) is repeatable and often used to scale and model the pressure induced by wave impacts (Cooke et al., 1995; Almeida et al., 2020). However, the variability of the impact pressure is especially relevant in applications, such as liquid sloshing of LNG (Y. K. Song et al., 2013; Lafeber et al., 2012a), slamming on wave energy converters (Henry et al., 2015; Renzi et al., 2018), and wave induced loads on floating offshore structures (Buchner et al., 2007).

The decades of wave research have resulted in numerous reviews, such as a review on liquid sloshing impacts (Ibrahim, 2020), a review of water wave impacts on vertical walls (Peregrine, 2003), and a detailed review on slamming (Dias et al., 2018). The wave impact process is subdivided into elementary loading processes (ELPs), such as the direct impact, the jet deflection, and the compression of the entrapped or escaping gas (Lafeber et al., 2012b). Each combination of elementary loading processes results in a different wave impact pressure distribution, and wave impact shape (i.e., type). The wave impact types are either defined as a slosh, a flip-through, a gas pocket, or an aerated type of wave impact (Hattori et al., 1994; Peregrine, 2003). A gas pocket type impact is often created by a plunging breaking wave. However, the scaling of wave impact pressures and wave impact types from small-scale to large-scale is not trivial (Ibrahim, 2020; Lafeber et al., 2012a).

Dynamic similarity is generally not easily obtained during wave impact events when scaling from small-scale to large-scale (Ibrahim, 2020). The relevant similarity

parameters change when the wave approaches the impact wall, which warrants the use of ELPs to identify the similarity parameters at each step of the wave impact process (Lafeber et al., 2012b). For example, the global flow, where the wave is not influenced by the presence of the impact wall (i.e., the increase in pressure in the gas pocket and increase in flow from the enclosed gas pocket), can be Froude scaled (Bogaert et al., 2010; Dias et al., 2018). On the other hand, the scaling of the local flow is not straightforward. The local flow is influenced by the strong gas flow over the wave crest and by the surface tension of the gas-liquid interface (L. Frihat M. B. et al., 2017), the gas-liquid density ratio (Karimi et al., 2015; Karimi et al., 2016), the compressibility of the gas (i.e., the speed-of-sound) (Bogaert et al., 2010), the possibility of phase change (Ancellin et al., 2018a; Ancellin et al., 2019; Ancellin et al., 2018b), and the aeration of the liquid (Bredmose et al., 2015; Bullock et al., 2007; Bullock et al., 2001). The scaling of the local flow is not well understood, but especially the formation of ligaments and droplets are thought to be relevant for the variability in wave impact pressures (Dias et al., 2018; Lubin et al., 2019).

The source of impact pressure variability in repeated wave impact experiments is thought to be the instability development on the wave crest. The mechanisms that are responsible for the formation of these instabilities are still largely unknown (Lubin et al., 2019). The shear force induced by the gas flow can result in the variability of the local flow (Lubin et al., 2019; Fortin et al., 2020; M. Frihat et al., 2016; Karimi et al., 2016). Additionally, the wave tip of the plunging breaking wave can be deflected (Abrahamsen et al., 2011; Firoozkoohi et al., 2017). Prior to impact, gas cushioning (i.e., the increase in pressure in front of the wave tip) can also result in deformation of the wave tip (Ross et al., 2019; Hicks, 2018; Peters et al., 2013). The wave tip deflection is shown to depend on the density ratio and the scale of the experiment (Karimi et al., 2015; Karimi et al., 2016). In a previous manuscript the variability of repeated wave impact experiments was accurately determined, and a mechanism for free surface instability development was presented (Meerkerk et al., 2020b). However, the influence of the gas flow on the local flow during repeated wave impact experiments has not been investigated yet.

In the present study, particle image velocimetry (PIV) measurements are combined with accurate free surface measurements at both a local and global scale to further investigate the mechanism of impact pressure variability in repeated wave impact experiments. The wave generation method is repeatable on a global level, whereas the local flow displays significant variation in both the details of the wave crest shape and the impact location (Meerkerk et al., 2020b). The local flow is investigated with both flow field (PIV) and stereo-planar laser-induced fluorescence (stereo-PLIF) free surface profile measurements. The PIV measurements are performed with two field-of-views (FOVs) to obtain both the global and local flow fields with sufficient accuracy. The velocity profile between the wave crest tip and the impact wall is repeatable. However, in Sec. 4.3.2 we will show that there is a mismatch between the bulk velocity based on the velocity profile and the mass conservation estimate. A velocity profile fit that resembles the potential flow over a bluff body is required to accurately determine the bulk velocity. Additionally, two typical vorticity fields are

identified that depend on the shape and smoothness of the wave crest. Interestingly, the difference in wave crest shape also result in a change of the velocity field prior to impact. The change in velocity field (i.e., the formation of a secondary vortex) results in additional lift at the wave crest tip. The formation of a secondary vortex near the wave crest tip is identified as an additional source of wave impact pressure variability.

This chapter is organized as follows: the experimental setup and equipment are introduced in Sec. 4.2. The PIV method is described in detail, whereas references to the other elements of the experimental set-up are presented. Thereafter, the results are introduced and discussed (Sec. 4.3). First, in Sec. 4.3.1, the global gas flow around the wave crest is discussed for a typical case. Then, in Sec. 4.3.2, the velocity profile between the wave crest tip and the impact wall is discussed. Thereafter, in Sec. 4.3.3, the development of a vortex over the wave crest and near the wave crest tip are discussed in the context of wave impact pressure variability. Finally, the findings are summarized in Sec. 4.4.

4.2 EXPERIMENTAL APPROACH

4.2.1 WAVE FLUME

The measurements are performed in the wave flume of the Hydraulic Engineering Laboratory at the Delft University of Technology (fig. 4.1). The flume is 39 m long with a cross-section of $0.79 \times 1 \text{ m}^2$, and the water depth is maintained at $h_0 = 500.0 \pm 0.5 \text{ mm}$ for all measurements. The flume is equipped with a piston-type wavemaker that has a maximum stroke of 2 m. The time between measurements is reduced with an active reflection compensation system, that is only enabled after the impact of the focused wave on the vertical impact wall.

In this work, a plunging breaker with a large gas pocket that impacts on a vertical wall is studied. The large gas pocket wave is generated with a wave focusing technique (Hofland et al., 2010). The wave group with varying phase velocity and wave length is focused on the focal point (x_f). The varying wave lengths of the wave group is clearly visible in the measured free surface elevation profile, that is shown in the inset of figure 4.1. The angle of the wavefront with respect to the impact wall and the impact type are determined by the focal point of the wave groups. A shift of the focal point results in either: a slosh, a flip-through, a gas pocket, or an aerated impact (Hattori et al., 1994). A wave shape is experimentally determined that results in a high impact pressure while enclosing a large gas pocket. The nearly parallel front of the wave crest (i.e. a wave crest aligned with the impact wall) results in a high impact pressure (Bullock et al., 2007). The required wave shape is obtained with a trial-and-error approach, and a normalized focal point of $x_f/h_0 = 0.81$ is obtained.

The current method of wave generation is similar to the *large scale* tests of the Sloshel project (Lafeber et al., 2012a). A similar depth-based Froude number is required to compare the measurements. The effective flume length is therefore scaled

as $\lambda = h_0/h_0^*$ with h_0 the current water depth and h_0^* the reference water depth (Lafeber et al., 2012b). The reduced effective flume length is obtained by mounting a 20 mm thick transparent perspex wall on a rigid construction at a distance of $L = 23.4$ m from the wave board (fig. 4.1). However, exact Froude scaling is not achieved due to practical limitations (e.g., the camera measurement system limits the water depth to 500 mm). The Froude scaled ratio is (1 : 7.3) compared to the (1 : 6) ratio of the Sloshel experiments, which will result in a smaller wave (i.e., with a smaller gas pocket and lower wave impact height) (Lafeber et al., 2012b; Bogaert et al., 2010).

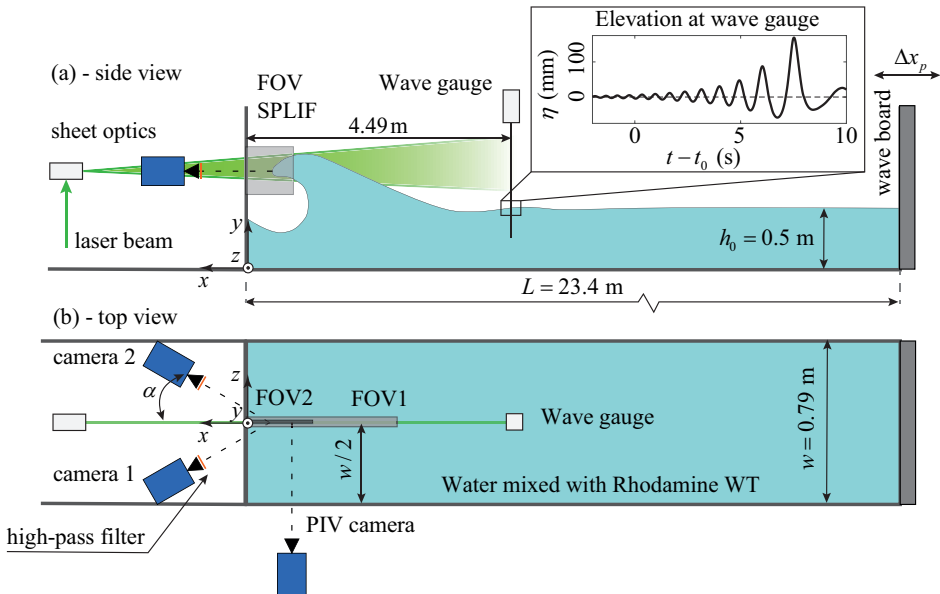


Figure 4.1: Schematic of the experimental facility adapted from a previous manuscript (Meerkerk et al., 2020b). (a) Side-view of the wave flume. The cameras for the stereo-PLIF are positioned on a xz -plane. A vertical light sheet (xy -plane) is created at the center plane of the flume. A wave focusing technique (see inset) is used to generate a large plunging breaking wave that impacts the vertical wall at $x = 0$. The wave board ($x = -L$) generates waves with different wave length, as shown in the inset near the wave gauge, that focus on a single location (x_f) in the wave flume. (b) Top view of the set-up. The PIV camera camera measures the global wave shape and the velocity around the wave crest of the plunging breaker at the center plane of the flume. The velocity field around the wave crest is determined at two levels of magnification, respectively FOV1 and FOV2. The stereo-PLIF system measures wave crest details in a smaller field-of-view at the light-sheet location.

The generation of nominal identical waves with a focusing technique is not trivial, as changes in the initial conditions, such as the water depth result in a different impact type (Kimmoun et al., 2010; Bagnold, 1939; Novaković et al., 2020). The variance in impact type, without biases due to scale, result from two sources of

variability: the *system variability*, and the *hydrodynamic variability*. Minimization of the system variability is essential to study the hydrodynamic variability (e.g., the growth of free surface instabilities on a wave crest). The control parameter variation of the facility (i.e., system variability), such as the water depth, the piston motion, and residual motion are minimized within the limitations of the experimental facility. The wave generation is shown to be repeatable in a previous manuscript (Meerkerk et al., 2020b). However, the comparison between measurements over several days is limited due to inevitable day-to-day variations present in wave flume facilities (Kimmoun et al., 2010; Bogaert et al., 2010).

4.2.2 EXPERIMENTAL METHODS

The gas velocity and local free-surface profile are measured simultaneously with planar particle image velocimetry (PIV) and stereo planar laser induced fluorescence (stereo-PLIF). The stereo-PLIF technique is described in detail by Meerkerk et al. (2020a), and the application of the technique in the current facility is described in (Meerkerk et al., 2020b). In this manuscript the equipment used for the stereo-PLIF measurements is only introduced, and the interested reader is referred to the previous manuscripts for details concerning the data processing of the stereo-PLIF images (Meerkerk et al., 2020b; Meerkerk et al., 2020a). The PIV equipment and processing are introduced and discussed in the following paragraphs.

Illumination of the PIV domain is provided by a high-speed Nd:YLF laser (LDY 304 PIV laser, Litron) with an output of approximately 10 mJ per pulse at a repetition rate of 2.5 kHz. A vertical light sheet is created at the center plane of the flume (fig. 4.1). The light sheet is created by expanding a laser beam with a cylindrical lens of focal length -12.5 mm. Additionally, the beam is focused into a narrow sheet with a cylindrical lens ($f = 1000$ mm), which results in a light sheet thickness of approximately 2.5 mm.

The laser illuminates both the water droplets in the gas (see below) and the incoming wave. The water in the flume contains a low concentration of fluorescent dye (Rhodamine WT, Sigma-Aldrich at 120 mg m^{-3}). The stereo-PLIF cameras are equipped with an optical high-pass filter that only shows the illuminated free surface. The free surface detected with the stereo-PLIF technique is projected onto the PIV plane. The PIV data is masked with the projected stereo-PLIF data in the final step of the PIV processing.

Seeding of the stagnant air in this experiment is not trivial. Small droplets or particles would precipitate onto the free water surface where they would affect the surface tension properties (Belden et al., 2011; Reul et al., 2007; Buckley et al., 2017). The effect of seeding on the gas-liquid surface tension is reduced with water droplet seeding (Buckley et al., 2016). A continuous supply of seeding particles is generated with a commercial ultrasonic humidifier (UHW, Medisana). The device is enabled prior to the experiments to fill up the flume with a fog of small water droplets. The diameter of the droplets (d_p) is determined with a *interferometric particle imaging*

(IPI) technique and is approximately $d_p \approx 10 \mu\text{m}$ (see Appendix B for details). The particle response time is approximately $\tau_p = \rho_p d_p^2 / 18 \nu_f \rho_f = 0.3 \text{ ms}$ based on a particle density of $\rho_p = 998 \text{ kg m}^{-3}$, the density of air $\rho_f = 1.23 \text{ kg m}^{-3}$ at standard atmospheric conditions, and the kinematic viscosity of air of $\nu_f = 15 \times 10^{-6} \text{ m}^2 \text{ s}^{-1}$. The settling velocity of the particles (e.g., $\Delta u = (\bar{\rho} - 1) / \bar{\rho} g \tau_p \approx 3 \text{ mm s}^{-1}$) is small with respect to typical velocities of the wave impact. The tracer particles are estimated to follow velocity fluctuations up to a cut-off frequency of approximately 550 Hz (Mei, 1996; Adrian et al., 2011). Furthermore, the particles are able to adjust to the acceleration expected in the measurements based on the bulk velocity estimate (Buckley et al., 2017; Meerkerk et al., 2020b).

The images are acquired with three high-speed CMOS cameras (Imager HS 4M, LaVision). The stereo-PLIF cameras (i.e., camera 1 and 2 in fig. 4.1) are equipped with 55mm Micro-Nikkor objectives with an aperture of $f^\# = 16$ to accommodate the large separation angle (α) of 60 degrees with respect to the vertical. A high-pass filter (OG570, Schott) is used to maintain the emitted light from the fluorescent dye. The PIV camera is equipped with a 35mm Micro-Nikkor objective with an aperture of $f^\# = 8$ for FOV1 and a 105mm Micro-Nikkor objective with an aperture of $f^\# = 4.6$ for FOV2 (fig. 4.2). The frame rate (f_{aq}) is 2.5kHz with an exposure time (Δt_e) of $363 \mu\text{s}$. The frame rate is obtained at a reduced image resolution of 1157×631 pixels for FOV1 and 1042×849 pixels for FOV2.

The PIV camera is calibrated for FOV1 with a PMMA plate with crosses equally spaced at a distance of 50 mm, whereas for FOV2 a two-plane dot-pattern target (Type 22, LaVision) is used. A third order polynomial mapping function is determined for both field of views to back-project the images to the center plane of the flume (Soloff et al., 1997; Adrian et al., 2011). The error on the mapping function is 0.1 and 0.3 pixels at a scale of 2.1 and 6.3 pixels per millimeter for respectively FOV1 and FOV2.

The images are processed with a PIV algorithm implemented in Matlab (2019B, Matlab). The images are preprocessed with a min-max filter that normalizes the image contrast (Adrian et al., 2011). However, significant variation in image intensity remains due to both the reflection of light from the free-surface and the non-homogeneous seeding of the gas. The variation in image intensity contaminates the correlation peak (Wernet, 2005; Eckstein et al., 2008). Therefore, symmetric phase only filtering (Wernet, 2005) is applied with a symmetric filter to sharpen the correlation peak (see appendix C). The images are processed with a multi-pass and multi-grid interrogation strategy with window deformation. The advantage of the multi-grid approach is the increased dynamic range of the PIV measurements (Adrian et al., 2011). The final multi-pass step results in an interrogation window of $16 \times 16 \text{ px}$ and $8 \times 8 \text{ px}$ at an overlap of 50% for respectively FOV1 and FOV2. The vector spacing is approximately 3.8 and 0.6 mm for the respective field of view's. Outliers are identified with a median test (typically 3% of the vectors in the initial pass) and replaced by interpolation (Westerweel, 1994).

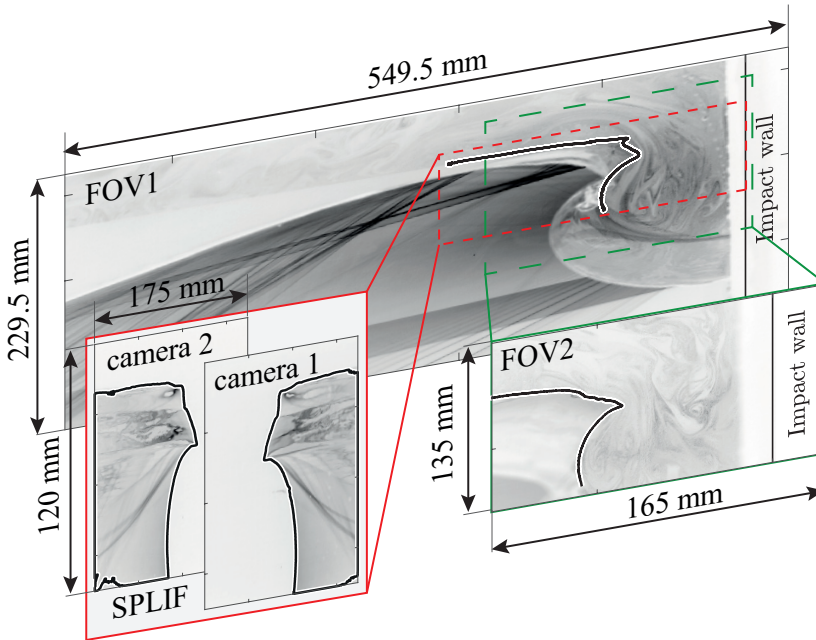


Figure 4.2: The field of view (FOV) of each measurement system is defined. The PIV measurements are performed at two magnifications, which results in a large field of view (FOV₁) and a small field of view (FOV₂) measurement. The stereo-PLIF (SPLIF) measurements are combined with the ellipse fit of the gas-pocket cross-sectional area (Meerkerk et al., 2020b) to mask the PIV images. The stereo-PLIF images of camera 1 and 2 (see fig. 4.1) are combined into a single profile that describes the interface location over a domain of 175 mm × 120 mm.

4.3 RESULTS AND DISCUSSION

In this section the results are introduced and discussed. First, the global gas flow behavior over a plunging breaking wave prior to impact on a vertical wall is discussed and relevant definitions are introduced. Second, the gas velocity between the wave crest and the impact wall is determined, and the velocity profile is estimated from the valid velocity vectors. Third, the vorticity and circulation over the wave crest are determined and discussed. Finally, the variability of two typical wave impacts is studied and a mechanism that increases the variation is discussed.

4.3.1 GLOBAL GAS FLOW

The development of the gas flow over a plunging breaking wave prior to impact on a vertical wall is shown in figure 4.3. This figure shows case M225 one of the two highlighted measurements in this work. These measurements are part of a larger set of $N = 21$ measurements that were collected over two successive days. The panels show the stereo-PLIF data (fig. 4.3 d) and velocity fields superimposed on the

original image of the wave with tracer particles. The gas is expelled from the gas pocket with cross-sectional area $A(t)$ and flows through the throat ($\Delta x(t)$) between the wave crest tip ($\vec{x}_{wt}(t)$) and the impact wall (fig. 4.3a).

Progressive water waves generate a flow of gas over their free surface by moving through the stagnant air (e.g., similar to an obstacle moving through air). The wave crest geometry (i.e., the height and slope) and wave celerity define the gas velocity and possible flow separation (Belden et al., 2011). In most cases, flow separation occurs at the wave crest (e.g., the top of the wave), which results in a vortex (Reul et al., 1999). The vortex often separates from the wave crest and the separated vortex lingers in the air (Belden et al., 2011). Plunging breaking waves also develop a vortex over their wave crest as they plunge towards a free surface (Techet et al., 2005). Additionally, the gas velocity at the wave crest tip is enhanced by the flow from the enclosed gas pocket. However, such experiments are often performed on small amplitude waves. In this section, the gas flow over a plunging breaking wave prior to impact is discussed.

For $t = -24.0$ ms, the velocity from the gas pocket is mostly vertically directed (fig. 4.3 a). The flow structure resembles that of a wall-bounded jet, which is often observed in numerical simulations of wave impacts with a large gas pocket (Guilcher et al., 2018; Behruzi et al., 2017). On the other hand, the mist of water droplets already shows some form of circulation near the tip of the disturbance (fig. 4.3 a). The disturbance on the wave crest acts as a roughness element that triggers flow separation and the development of a shear-layer. Unfortunately, the resolution of the FOV₁ PIV data is not sufficient with a vector spacing of 3.8 mm to directly resolve the flow separation near the wave crest disturbance.

At $t = -18.0$ ms, the resolution of the PIV data is sufficient to detect a vortex at the back-side of the wave crest (fig. 4.3 b). A vortex is consistently formed in all wave impact measurements. The size of the vortex increases over time from panel b to d. Additionally, the velocity in the wall-bounded jet increases shortly before impact of the wave on the vertical wall. The development of the vortex resembles that of a plunging breaking wave impacting on a free surface (Techet et al., 2005). However, here the plunging breaking wave impact on the vertical wall lacks the development of large-scale secondary vortices that were observed by Techet et al. (2005) during the impact of a plunging breaker on a liquid free surface.

4.3.2 LOCAL GAS FLOW

The local gas flow is defined as the flow through the throat (Δx), that is the gap between the wave tip (\vec{x}_{wt}) and the impact wall. The plunging breaking wave forces gas through the throat by reducing the cross-sectional area of the gas pocket ($A(t)$). The rate of change of the cross-sectional area (A) is assumed to be constant over the span-wise direction of the wave, whereas the throat distance (Δx) is expected to vary. Typically, the *global flow* of the wave is repeatable when the *system variability* is minimal. The repeatability of the global flow in this facility has been confirmed

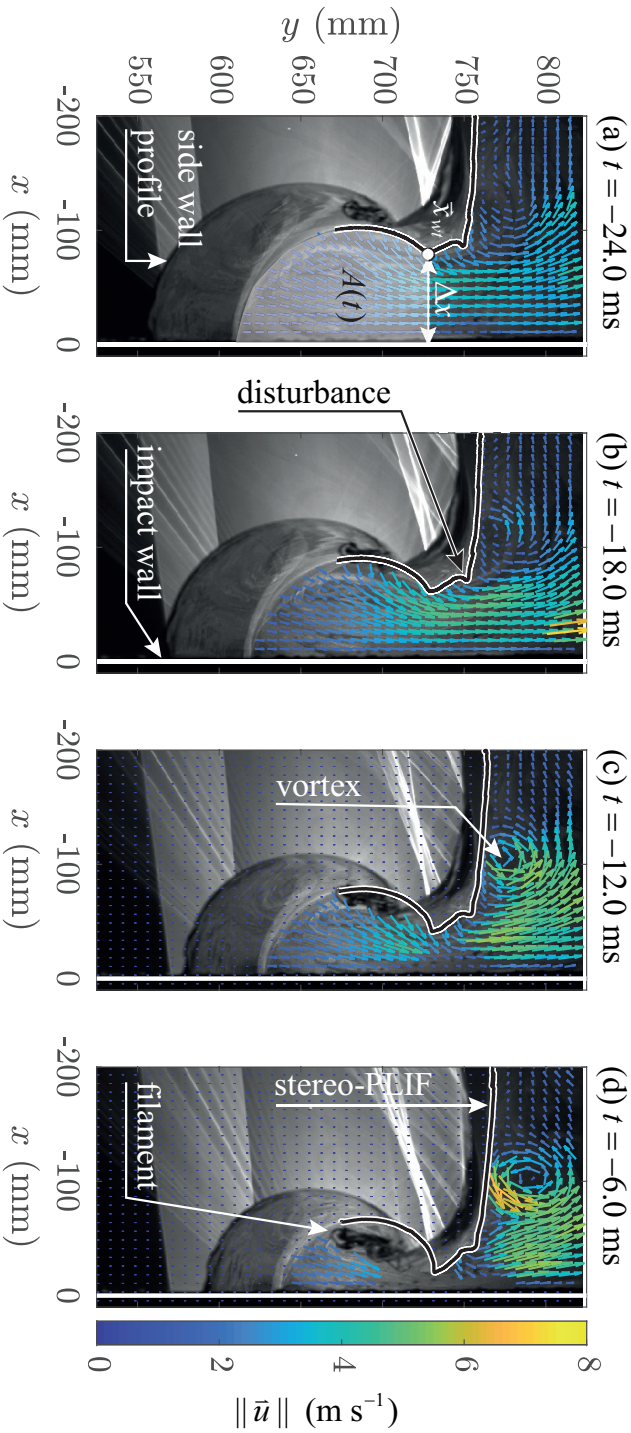


Figure 4-3: A combined visualization of the original PIV image, that shows both the development of the wave and the gas flow. An overlay is added that shows the vector fields obtained with PIV and the local wave crest shape obtained with the stereo-PLIF technique. The flow field develops over the wave crest for a typical measurement with a vertical wall located at $x = 0$. The moment of impact of the wave crest on the vertical wall is defined as $t = 0$ ms. (a) The focused wave approaches the impact wall and a wall-bounded jet develops for $t = -24.0$ ms. The wave tip coordinate (\hat{x}_w^t), the gas pocket cross-sectional area (A), and the distance between the impact wall, and the wave tip (Δx) are identified (i.e., the throat). (b) $t = -18.0$ ms: The gas velocity at the wave crest increases and the flow separates at the location of the disturbance on the wave crest. (c) $t = -12.0$ ms: The gas velocity increases significantly and a vortex is identified. (d) $t = -6.0$ ms: The vortex increases in size and the velocity magnitude inside the wall-bounded jet also increases. Additionally, the *liquid filament* suspended from the wave crest reduces the PIV data quality.

previously (Meerkerk et al., 2020b). The power-law fit of the cross-sectional area was found to be $A(t) - A(t = 0) = 1.74|t|^{1.52}$, which results in a rate of change of $dA/dt = 2.64|t|^{0.52}$ (Meerkerk et al., 2020b). The throat size is determined by the velocity of the wave crest tip, which is here $\Delta x = 2.67t + C$ with C being a constant. The width averaged or bulk velocity in the throat is, with the assumption of constant gas density, defined by mass conservation, as

$$v_b = \frac{1}{\Delta x} \frac{dA}{dt} \approx 0.8|t - \tau_0|^{-0.52} \quad (4.1)$$

with dA/dt the rate of change of the cross-sectional area, Δx the throat size, and t the time to impact (Meerkerk et al., 2020b). A time shift (τ_0) is included in the bulk velocity derivation, as the exact moment of impact is difficult to determine from the stereo-PLIF and visualization images of the wave impact.

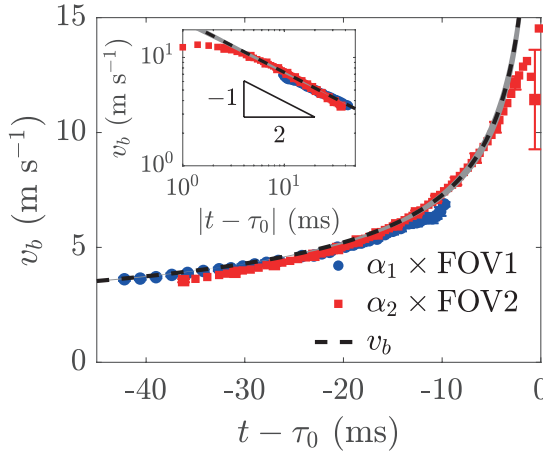


Figure 4.4: The bulk velocity is determined at the y -coordinate of the wave tip (y_{wt}) for both FOV₁ and FOV₂. The bulk velocity is averaged per time step over all recorded measurements (i.e., per FOV), which results in a repeatable bulk velocity with a negligible standard deviation of approximately 2.2% for both cases. A temporal shift of $\tau_0 = 5$ ms and pre-factors (α_1 and α_2) are required to overlap the measured bulk velocity with the bulk velocity based on mass conservation and constant gas density. The pre-factors are approximately 1.54 and 1.64 for respectively FOV₁ and FOV₂. However, the power-law exponent of the PIV measurements is comparable to the exponent derived from mass-conservation for both field of views.

The bulk velocity in the throat is determined for all PIV measurements of both FOV₁ and FOV₂. The bulk velocity is obtained by integrating the velocity profile over three interrogation windows centered at the y -coordinate of the wave tip. The bulk velocity is averaged per FOV over all repeated measurements, which requires the x -coordinates of the wave tip to be matched. The difference between the x -coordinate of the wave tip over repeated measurements is minimal, and the maximum temporal shift over all repeated measurements is only 2.5 ms. The bulk velocity over time is

shown for both FOV₁ and FOV₂ in figure 4.4. The bulk velocity is repeatable for both FOV₁ and FOV₂ with an averaged standard deviation over bulk velocity of 2.2% for both measurements.

The bulk velocity based on mass conservation required a shift in impact time of $\tau_0 = -5$ ms to overlap with the bulk velocity obtained in both FOV's of the PIV measurements (fig. 4.4). Additionally, a pre-factor (α_i) is required to overlap the measured bulk velocity with the bulk velocity based on mass conservation. The pre-factors are 1.54 and 1.61 for, FOV₁ and FOV₂ respectively. The pre-factor is not completely constant over time, but the PIV measurements consistently underestimate the averaged velocity based on mass conservation. However, the power-law exponent of the mass conservation bulk velocity is adequately retrieved, as shown in the inset of figure 4.4. The underestimation of the bulk velocity by the PIV measurements is studied based on a single velocity profile.

The velocity profiles of both FOV₁ and FOV₂ are determined at the y -coordinate of the wave tip for $t - \tau_0 = -15.0$ ms and averaged over all repeated measurements per FOV. The same temporal shift of $\tau_0 = -5$ ms is applied to overlap the mass conservation and measured bulk velocity estimate. The velocity profile is normalized by the wave tip distance (Δx) such that the impact wall is located at $x/\Delta x = 0$ and the wave tip $x/\Delta x = 1$ (fig. 4.5). Note that the velocity profile of FOV₁ is different from that of FOV₂ (fig. 4.5a).

First, the averaged valid velocity data of FOV₁ is shown in 4.5 a. The measurements of FOV₁ are not as repeatable as those of FOV₂ with error bars that are smaller than the marker size (typically 9.5% of the velocity) for $0.3 \leq x/\Delta x \leq 0.75$. However, the velocity decreases close to the impact wall and the wave tip. The velocity at the impact wall ($x/\Delta x = 0$) is lower than expected, as the spatial resolution of FOV₁ is limited. The center of the domain of FOV₁ is slightly misaligned with the center of the impact wall, which results in a small perspective error. The perspective error blocks the view of the tracer particles for approximately $x/\Delta x \leq 0.1$. Furthermore, the detection of accurate velocity vectors in the neighborhood of walls is compromised and errors can easily propagate through the domain (Hochareon et al., 2004). Additionally, loss of correlation occurs, which decreases the velocity at the impact wall for FOV₁. The domain of FOV₂ has been properly aligned with a higher spatial resolution, which does not result in a decrease of the velocity near the impact wall. The measurements of FOV₂ are repeatable with error bars that are smaller than the marker size (typically 2.6% of the velocity) for $0 \leq x/\Delta x \leq 0.75$. On the other hand, the decrease in velocity at the wave tip ($x/\Delta x = 1$) is also observed for FOV₂.

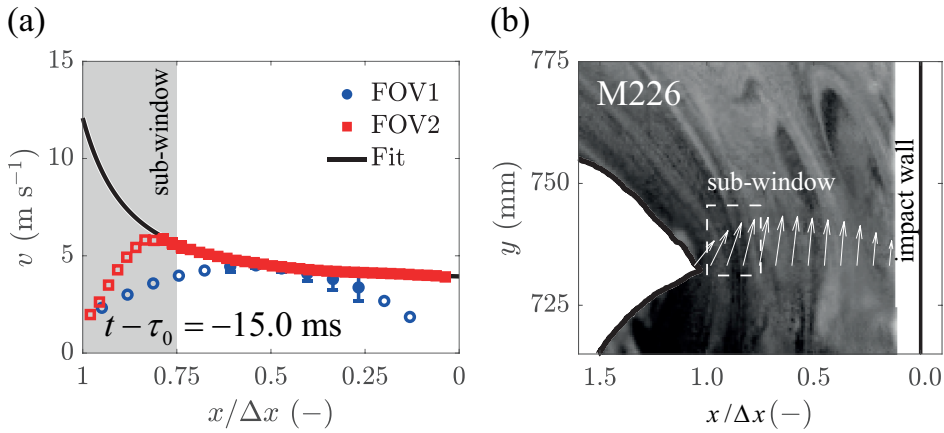


Figure 4.5: (a) The velocity profile between the wave tip ($x/\Delta x = 1$) and the impact wall ($x/\Delta x = 0$) at $t - \tau_0 = -15.0$ ms, where the wave impacts the wall at $x = 0$ for $t - \tau_0 = 0$. The velocity profile resembles that of a potential flow over a bluff body with $v(x/\Delta x) - 1.23 = 2.4[1 + (\frac{-0.44}{x/\Delta x + 1.24})^2]$. (b) A typical image of the seeding concentration at $t - \tau_0 = -15.0$ ms for M226. The velocity profile decreases close to the wave crest ($x/\Delta x = 1$), due to inhomogeneities in the seeding concentration and image intensity.

The velocity is observed to decrease near the wave crest for approximately $0.75 \leq x/\Delta x \leq 1$, which is denoted as the *sub-window* in panel a of figure 4.5. In panel b of figure 4.5 the same sub-window is shown for measurement M226 of FOV₁, which shows a non-uniform seeding distribution near the wave tip. The non-uniform seeding distribution consistently occurs over multiple measurements. The seeding is not only non-uniform, it also shows the displacement of streaks near the tip of the wave crest. The discontinuities in seeding concentration are already introduced at the nozzle of the seeding supply. The acceleration of the gas stretches patches of seeding to streaks, which results in a reduced PIV accuracy near the wave crest tip.

The discontinuities in image intensity that result from the non-uniform seeding result in a decrease of the vector quality (Wernet, 2005). A symmetric phase only filter is already applied to increase the peak detectability as described in appendix C. However, the lack of identifiable seeding particles near the tip of the wave crest still results in a deterioration of the accuracy and a decrease of the magnitude of the velocity vectors. The measured bulk velocity at $t - \tau_0 = -15.0$ ms is, without correction, approximately 4.3 and 4.5 m s⁻¹ for FOV₁ and FOV₂ respectively. The bulk velocity based on mass conservation is approximately 5.2 m s⁻¹, which is significantly higher than the measured bulk velocity for both FOV's.

The velocity profile between the wave crest tip and the impact wall resembles that of a potential flow over a bluff body. The flow between the wave crest tip and the impact wall is in good approximation inviscid and irrotational, which enables a potential flow comparison. The Reynolds number based on the mass conservation bulk velocity at $t - \tau_0 = -15.0$ ms is approximately $Re = v_b L / \nu_g \approx 2 \times 10^4$ for a wall to tip distance of $\Delta x = 50$ mm, and a kinematic viscosity of $\nu_g = 15.06 \times 10^{-6}$ m² s⁻¹

of air at 20 °C and standard atmospheric conditions. Therefore, a fit of the velocity profile is proposed, as:

$$v\left(\frac{x}{\Delta x}\right) - v_{\text{trough}} = U_0 \left[1 + \left(\frac{C_0}{\frac{x}{\Delta x} + C_1} \right)^2 \right] \quad (4.2)$$

with the unknown dimensionless parameters C_0 , and C_1 , the velocity past the potential flow object (U_0), and the upwards trough velocity (v_{trough}) of 1.23 m s^{-1} (Meerkerk et al., 2020b; Lamb, 1993). The potential flow object is fixed on the wave tip, which requires a translation from the laboratory coordinate system to the wave coordinate system. The trough velocity (v_{trough}) is used to defined the wave tip coordinate system. The dimensionless parameters C_0 and C_1 are relatively constant over time with respectively values of -0.47 and 1.2 . On the other hand, the velocity past the potential flow object follows a quadratic relation of approximately $U_0 = 2170t^2 + 191t + 4.7$. The velocity profile obtained in the experiments resembles that of numerical work on a plunging breaking wave impact¹. Furthermore, the bulk velocity determined from the fit of the experimental data is approximately 5.25 m s^{-1} , which falls within the bounds of the mass conservation estimate with a deviation of only 1% compared to the averaged mass conservation estimate at $t - \tau_0 = -15.0 \text{ ms}$.

The gas velocity near the wave crest is significantly higher with a velocity of 12 m s^{-1} compared to the bulk velocity of 5.2 m s^{-1} based on the fit. Recent numerical simulation also show the high velocity near the wave crest (Etienne et al., 2018). A higher velocity near the wave crest can result in an earlier onset of shear instability development (i.e., Kelvin-Helmholtz instability). The earlier onset of shear instabilities are, based on the fit, hypothesized to be the cause of the disturbances on the wave crest geometry, such as those shown in panel b of figure 4.3.

4.3.3 DYNAMICS OF THE CIRCULATION ZONE

The source of variability in peak impact pressure observed during wave impact experiments is still largely unknown. However, the formation of instabilities on the wave crest is hypothesized by other to be the main source of wave impact pressure variability (Dias et al., 2018; Lubin et al., 2019). Does the gas flow induce additional variability apart from the formation of instabilities? In this section the flow field over the wave crest is discussed, which introduces the development of large vortices over the wave crest and of local vortices near the wave crest tip.

The vorticity component that is perpendicular to the measurement domain ($\omega_z = \partial v / \partial x - \partial u / \partial y$) is estimated with a filtered second-order difference method (Adrian et al., 2011). This method is based on an 8-point estimate of the local circulation. The presence of the free surface locally complicates the calculation of the vorticity, as the vorticity can not always be determined with an 8-point estimate (Belden et al., 2011). A free surface that is included in the computation of the vorticity will result

¹ Private communication, R. Remmerswaal, University of Groningen, 2020

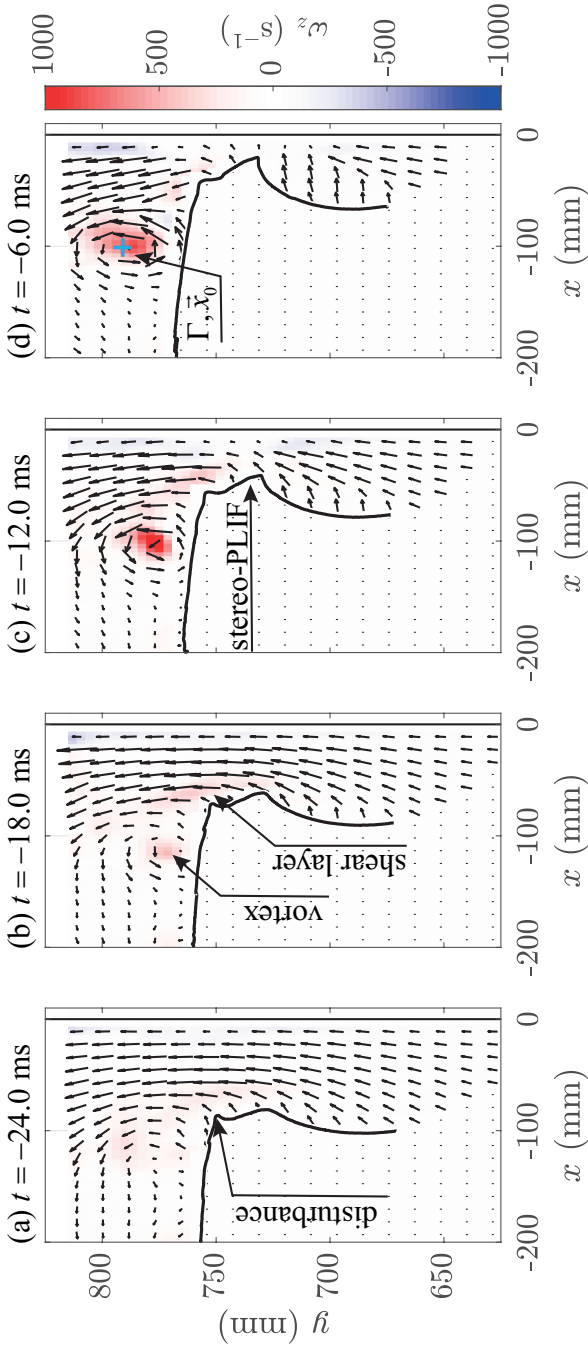


Figure 4.6: The vorticity component perpendicular to the measurements plane (ω_z) is shown for a typical wave (M225) that contains a disturbance on the free surface. The velocity overlay shows every third vector in x and y direction. The time steps in panels (a)-(d) correspond to the velocity fields previously shown in figure 4.3. (a) The velocity and vorticity field do not indicate the existence of a vortex. Although, a hint of a shear-layer that rolls-up into a vortex may be visible. (b) A small recirculation zone is created at the wave crest and a shear layer is visible over the wave crest. (c) The strength of the vorticity in the recirculation zone increases. (d) The recirculation zone grows even further and separates from the wave crest, as the center location of the vortex core remains stationary.

in an artificial shear-layer at or near the surface (Dabiri et al., 1997). Therefore, the vorticity is only calculated with the valid vectors fully in the gas phase. The vorticity development is shown in figure 4.6 for a typical case with a disturbance (M225).

Initially for $t = -24.0$ ms, there is no visible vorticity development over the wave crest (fig. 4.6 a). If a vortex is present at this stage it cannot be resolved because of the limited vector spacing of 3.8 mm. However, a small vortex and shear-layer are visible at $t = -18.0$ ms (fig. 4.6 b). The vortex structure forms on the back of the wave crest close to the disturbance on the free surface (Belden et al., 2011; Buckley et al., 2016). Airflow separation over free surfaces is complex to detect, but it is often linked to wave breaking during wind wave generation (Buckley et al., 2016). The vortical structure grows in size and the vorticity magnitude increases as the wave approaches the wall (fig. 4.6). The vortex grows behind the disturbance, which becomes especially clear for $t = -6.0$ ms in panel d of figure 4.6.

A vortical structure consistently develops at the backside of the wave crest for all measurements. Two typical vortical structures can be identified in the current experiments based on the shape of the free surface, the growth rate and size of the vortex. Measurement M225 is one of the typical examples of the first vortical structure, that separates from the wave crest close to the disturbance on the free surface. On the other hand, measurement M226 is one of the typical examples of the second vortical structure.

Figure 4.7 shows the second typical vortical structure for measurement M226. A clear difference between both waves and the development of the vortex is already present at $t = -24.0$ ms. The wave crest of M226 is smoother than that of M225 and this influences the vorticity development. For example, a small but consistent vortex is already present for $t = -24.0$ ms (fig. 4.7 a) that grows in both size and vorticity magnitude over time (fig. 4.7 b-c). Prior to impact, however, the vortex remains approximately stationary and equal in vorticity magnitude ($t \geq -12.0$ ms). Additionally, a secondary vortex develops near the wave tip (fig. 4.7 d). The circulation (Γ) and center point (\bar{x}_0) of the vortex is further evaluated (fig. 4.6 d). The focus is especially on the typical behavior of the vorticity development for either a smooth wave crest or a wave crest that contains a disturbance.

A vortex identification technique is required to determine the geometric and vortical properties of the vortex (fig. 4.6 b). There are several vortex identification techniques available, many of which are based on derived quantities of the velocity gradient tensor (Chakraborty et al., 2005). Vortex identification techniques that are based on the velocity gradient tensor are not robust if a large vortex is superimposed on a turbulent velocity field (Graftieaux et al., 2001). On the other hand, the resolution of the velocity field determined over FOV_1 is such that the small scale turbulence is not resolved, which inhibits the use of methods that rely on the flow field topology. The *swirling strength criterion* (λ_{ci}) is, therefore, used to identify the existence and center of a vortex (Zhou et al., 1999). The swirling strength criterion is frame independent and only identifies regions of circular motion.

The center of the vortex is defined by the maximum of the swirling strength criterion. The swirling strength criterion also defines the contours of the vortical

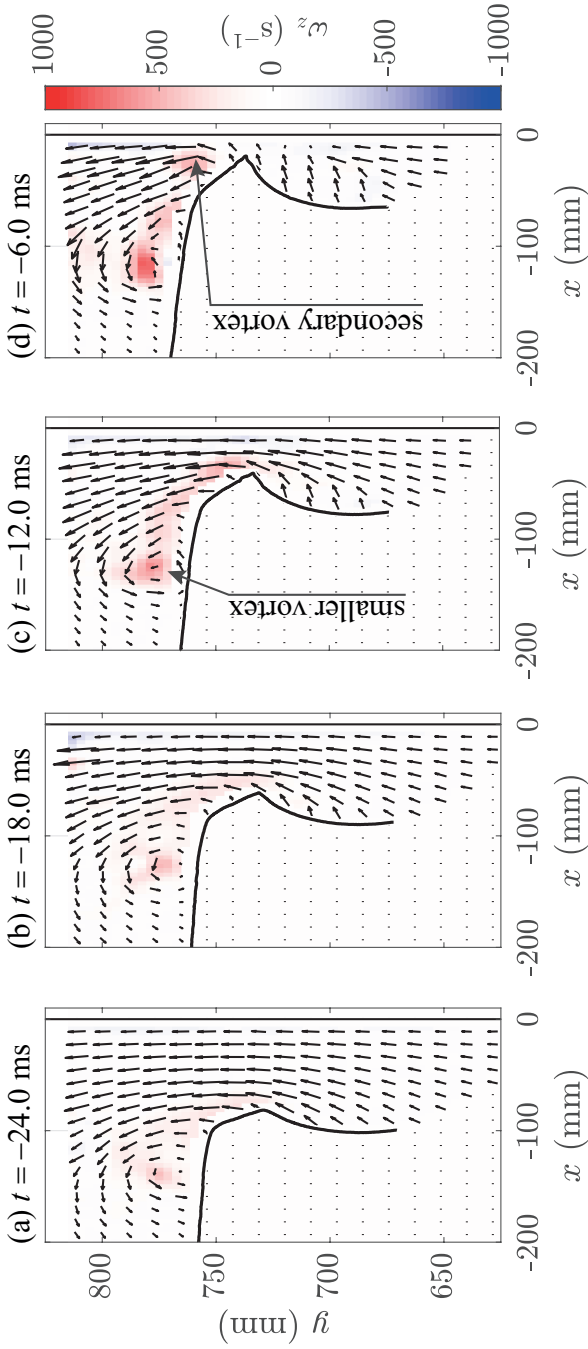


Figure 4.7: The vorticity component perpendicular to the measurements plane (ω_z) is shown for a typical wave (M226) that has no initial disturbance on the free surface. The velocity overlay shows every third vector in x and y direction. (a) If a vortex is present at this stage it cannot be resolved at the current resolution of the PIV measurements. (b) A small recirculation zone is created at the wave crest and a shear layer is visible over the wave crest. (c) The strength of the vorticity in the recirculation zone increases. (d) The recirculation zone grows even further and seems to separate from the wave crest as the center location of the vortex core remains stationary. Additionally, a secondary vortex is formed near the tip of the wave crest.

structure. The contour of the vortical structure is defined by the values of the circulation strength that are higher than a specified threshold (i.e., $\lambda_{ci} > 2.5\lambda_{ci,rms}$). Minor differences were observed for different thresholds, but no qualitative differences were identified. The root-mean square of the swirling strength criterion is only determined over the non-zero components. Thereafter, the circulation (Γ) of the vortex is calculated as,

$$\Gamma = \int_A \omega_z dA = \sum_{i=1}^N \omega_{z,i} dx dy \quad (4.3)$$

where ω_z is the vorticity, and N the number of elements inside the contour of the vortical structure defined by the swirling strength criterion.

The circulation (Γ) is determined for all measurements of FOV₁ (fig. 4.8). However, only the data points for M225 and M226 are displayed, whereas the range of all circulation measurements is indicated by the gray area and its average by a black line. The circulation initially shows a significant growth for about $t > -20.0$ ms, which is comparable with the first observation that the vorticity magnitude increases after $t = -18.0$ ms in figure 4.6 and 4.7. Thereafter, the circulation becomes constant for both measurements, but the circulation magnitude is significantly higher for measurement M225 compared to M226 (i.e., approximately a factor 2).

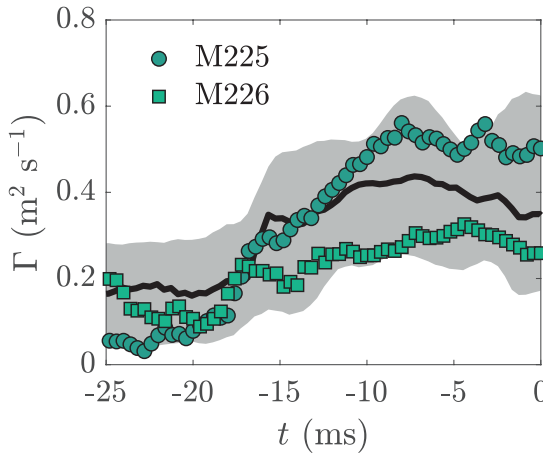


Figure 4.8: The circulation (Γ) is determined by integrating the vorticity field inside the contour that encloses the maximum of the swirling strength criterion (λ_{ci}). The gray area encloses the maximum and minimum of the circulation over all measurements of FOV₁ and the black line indicates the circulation average. Additionally, the circulation of measurement M225 and M226 of respectively figure 4.6 and 4.7 are shown. For both measurements the circulation increases up to a certain limit, after which it remains constant. However, the maximum circulation seems to depend on the wave shape and the corresponding evolution of the flow field.

The saturation of circulation in a vortex is a well-known phenomena (Gharib et al., 1998). An associated time scale (i.e., the formation number) can be defined as $t^* = Ut/L$ with U a typical velocity scale and L a typical length scale. The formation number is a dimensionless measure of the time it takes to create the largest possible vortex, which Gharib et al. (1998) postulates occurs at approximately $t^* = 4$. The circulation can be increased after the maximum formation number, but the vortex core will then shed the accumulated vorticity in its wake (Gharib et al., 1998).

In figure 4.8 the maximum circulation for measurement M225 and M226 is not obtained at a comparable time, whereas the *global* behavior of the plunging breaking wave is similar (Meerkerk et al., 2020b). Typically a length and time scale are easily defined and relatively constant. For example, the length and time scale of the piston by Gharib et al. (1998) are defined by the pistons shape and motion. In the current work, the typical length and time scale are non trivial and probably not even constant over time. However, an estimate of the required length scale is obtained by assuming a formation number of $t^* = 4$ at the maximum circulation of measurement M225. This can be obtained with a velocity over length scale ratio of approximately $U/L \sim 0.5$. A typical velocity scale of the plunging breaking wave is the velocity of the wave tip at 3.31 m s^{-1} , which would imply an unphysical length scale of approximately 6.6 m. Consequently, the circulation data is not displayed against the formation number. However, the largest possible vortex remains interesting, as the vortex is also observed to separate from the wave crest. For example, the vortical structure remains approximately stationary for measurement M225 for $t > -12.0 \text{ ms}$ (fig. 4.6c-d), which overlaps with the circulation limit (fig. 4.8).

The different circulation limits between measurement M225 and M226 and the occurrence of secondary vortices in measurement M226 warrant a detailed investigation of the velocity field over the wave crest tip. However, the resolution of the velocity field of FOV₁ is not high enough for a detailed investigation of the circulation and vorticity near the wave crest tip. Therefore, the development of the wave crest tip and flow field are studied using the water droplets as a visualization tool (fig. 4.9).

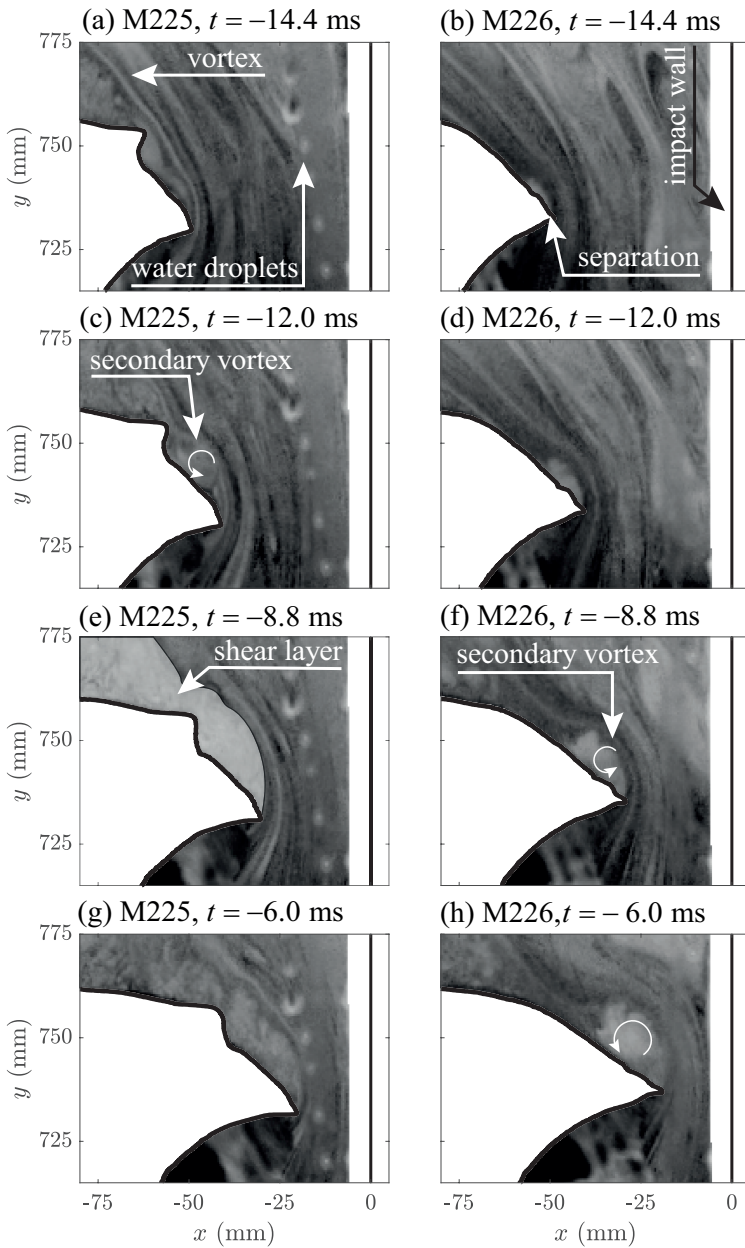


Figure 4.9: A visualization of the velocity field near the wave crest tip for two typical measurements with either a disturbance on the wave crest surface (M225) or a smooth wave crest surface (M226). (a-b) Initially the shear layer that feeds the vortex of measurement M225 is observed, whereas this is outside the shown domain for M226. The impact wall and water droplets on the side wall of measurement M225 are also indicated. (c-d) A separation region near the wave crest tip rolls up to form a secondary vortex for M225. (e-f) The development of the secondary vortex continues for M226, whereas for M225 the vortex breaks down into a shear layer. (g-h) The lift induced by the secondary vortex of M226 results in an upward displacement of the wave tip.

In panel a and b of figure 4.9 the visualizations of respectively measurement M225 and M226 are shown for $t = -14.4$ ms. The disturbance on the wave crest is directly visible for measurement M225, whereas it is absent for M226. Furthermore, a part of the vortex wake is identified in panel a, whereas for measurement M226 the vortex is further downstream and is not visible in the selected window. Measurement M226 displays the development of a small recirculation region near the wave crest tip.

The recirculation region near the wave crest tip develops further for both measurements at $t = -12.0$ ms (fig. 4.9 c-d). A small secondary vortex is already visible for measurements M225, whereas it is still absent for measurement M226. Interestingly, the secondary vortex develops further for measurement M226 at $t = -8.8$ ms, whereas for measurement M225 the development of the secondary vortex is blocked by the upstream disturbance on the wave crest. The secondary vortex is observed to breakdown for measurement M225 at $t = -8.8$ ms and a shear layer develops over the wave crest. The breakdown of the secondary vortex in measurement M225 seems to correspond to the saturation limit of the circulation (fig. 4.8). The secondary vortex remains attached to the wave crest tip for measurement M226 (fig. 4.9 h).

The development of a shear layer after separation of a vortex resembles that of a wing that experiences stall, which results in a decrease of the lift force and an increase in the drag force (Eldredge et al., 2019). Figure 4.10 shows the tip coordinate of respectively M225 and M226 obtained from the stereo-PLIF measurements. The difference between both measurements is clear, especially, prior to impact where the y_{wt} -coordinate of the wave tip displays a difference of approximately 6.8 mm. Initially, for $t < -20$ ms, both measurements show a similar displacement of the wave tip y_{wt} -coordinate. The development of the recirculation zone near the wave crest tip results in an increase of the lift force for $t > -12.0$ ms in measurement M226 (fig. 4.9 d). The lift induced by the secondary vortex result in an additional upward displacement of the thin wave tip.

Wave tip deflection is observed in numerous numerical simulations (see for example Behruzi et al. (2017) and Etienne et al. (2018)). The simulations often initialize the global wave generation with a potential flow model. Thereafter, the computations are performed with both liquid and gas coupling, which - as we show - is essential to model the variability of wave impact pressure. Especially, the development of circulation is important when considering the impact pressure variability, as the vortex at the wave crest tip induces an additional lift force. On the other hand, the small scale variability (i.e., on the order of a typical pressure sensor diameter) may be irrelevant for other applications. Consequently, numerical models that aim to quantify the variability in impact pressure need to model flow separation near the wave crest tip, as this is another source of wave impact pressure variability.

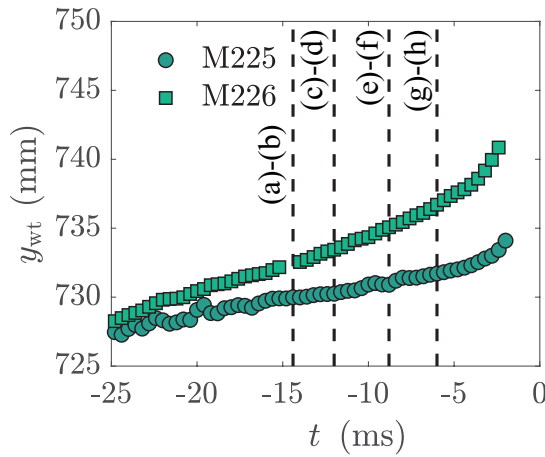


Figure 4.10: The wave tip location for two typical cases M225 with a disturbance on the wave crest and M226 with a smooth wave crest surface. The difference in wave crest shape results in a vortex with a lower circulation for M226, whereas the sharp disturbance on the wave crest of M225 results in a significantly higher recirculation zone. The formation of a secondary vortex near the tip of the wave for M226 results in a change in slope of the y_{wt} coordinate. The circulation zone has a significant influence on the wave tip impact location, and in turn on the variability of the wave impact pressure.

4.4 CONCLUSION

The repeatability of the gas flow over plunging breaking waves is determined prior to impact. Several repeatable focused waves are generated that impact on a vertical wall. The global gas flow behavior is comparable to that of a plunging breaking wave (Reul et al., 1999) and a progressive wave (Belden et al., 2011). A vortex develops over the leeward side of the plunging breaking wave that separates from the breaking wave and remains stationary in the stagnant air (Belden et al., 2011).

The gas flow drives the instability development on the wave crest, which requires an appropriate estimate of the bulk velocity. The bulk velocity was derived previously based on the shape of the global wave (Meerkerk et al., 2020b). However, the integrated velocity profile between the wave tip and the impact wall results in a significantly lower bulk velocity compared to the mass conservation estimate. The high velocity close to the wave crest tip is not resolved, because of the limited resolution of the PIV measurements and the absence of sufficient seeding near the wave tip. A fit of the velocity data that resembles a potential flow estimate over a bluff body results in a significant improvement of the bulk velocity estimate. Consequently, the gas velocity close to the wave tip is approximately 2 times higher than the bulk velocity estimate, which results in an earlier onset of instability development.

Two typical vortical structures are shown to develop over the wave crest for which measurement M225 and M226 are illustrative examples, that either have a smooth

wave crest (M226) or a wave crest with a disturbance (M225). The development of the vortex is different for each typical case. The vortical structure becomes larger if a disturbance is present on the wave crest surface compared to the other typical case. The circulation magnitude is almost double that of a smooth wave crest. On the other hand, the circulation development is similar for both cases, where the circulation remains stationary after an initial growth. The circulation development is typical for a vortex that eventually separates from the wave crest at a specified dimensionless formation number, but in this case a typical formation number cannot be defined (Gharib et al., 1998).

The gas flow directly alters the wave impact pressure variability. For example, a secondary vortex develops near the wave crest tip for the case of an initially smooth wave crest (M226). On the other hand, the disturbance on the wave crest for case M225 blocks the development of a secondary vortex, which results in a shear-layer with minimal lift. The secondary vortex increases the lift near the wave crest tip, which results in an additional deflection of the wave crest tip. The deflection of the wave crest tip is approximately 6.8 mm compared to the other typical case, which is significant on the scale of a typical pressure sensor. Consequently, an additional mechanism for the development of impact pressure variability on globally similar waves is the development of a secondary vortex (i.e., flow separation) over the wave crest tip.

The global characteristics of an air-water wave impact are unaltered by the presence of the gas phase. The global characteristics of the wave impact pressure can be retrieved with pressure impulse models (Cooker et al., 1995). On the other hand, the variability of wave impact pressure is largely driven by local phenomena, such as flow separation and the development of free surface instabilities. Consequently, numerical models that aim to quantify wave impact pressure variability on a local scale require accurate models of the gas phase. Additionally, the wave impact pressure variability that is induced by the tip displacement should also be studied at different atmospheric conditions (i.e., density ratios and ullage pressures) and different global wave shapes.

5

CONCLUSIONS AND PERSPECTIVES

Parts of this section are based on the results presented in previous chapters.

In this thesis, the source of wave impact pressure variability is studied. A newly developed free surface measurement technique is combined with particle image velocimetry (PIV) to provide new insights in the source of wave impact pressure variability. Each chapter of this thesis is based on a publication and is self-containing. Only general conclusions are provided in this chapter, followed by recommendations for future research.

5.1 CONCLUSIONS

Free surface instabilities form on a wave crest prior to impact on a vertical wall. These instabilities are suggested to be the source of wave impact pressure variability. The wave crest defines the location of the impact and thereby the wave impact pressure variability. However, local quantitative free surface measurements are not trivial to obtain.

An established planar laser induced fluorescence (PLIF) measurement technique is combined with a stereo-camera system and a scanning mirror to obtain an instantaneous two-dimensional (i.e., $y(x, z, t)$) free surface measurement technique (stereo-PLIF). Time-dependent two-dimensional stereo-PLIF measurements are obtained over a domain with a height of 100 mm. Free surface fluctuations can be measured with a minimal amplitude of $\eta = y - y_0 \approx 0.2$ mm. The stereo-PLIF measurement technique is versatile in its application, as both the domain size and temporal resolution can be scaled as needed. The free surface measurement technique is used to study the mechanisms that result in wave impact pressure variability due to a plunging breaking wave that impacts on a vertical wall.

A plunging breaking wave is generated at the Hydraulic Engineering Laboratory of the Delft University of Technology. The plunging breaking wave is generated with a wave focusing technique and it encloses a gas pocket just before impact on a vertical wall (fig. 5.1 a to c). The generation of repeatable waves with a wave focusing technique is not trivial, as variations in the initial conditions are amplified by the non-linear wave focusing. These variations in the initial conditions arise from the so-called *system* and *hydrodynamic variability*. The minimization of the *system variability* within the limitations of the experimental facility is essential to study the *hydrodynamic variability*. The *system variability* can be minimized over the course of a single day, but a day-to-day comparison is complicated due to the inherent *system variability*.

In a practical situation, the global wave behavior (i.e., the *global flow*) prior to impact is only repeatable for measurements obtained on a single day. The wave velocity ($\sqrt{gh_0}$) and wave tip velocity ($1.2\sqrt{gh_0}$) are initially similar to that of a plunging breaker. The cross-sectional area of the gas pocket can be approximated by a semi-ellipse constrained to the impact wall, where the aspect ratio of the ellipse remains relatively constant at $R_x/R_y = 1.6$ ($\sim \sqrt{3}$); this is comparable to that of a plunging breaking wave. On the other hand, the wave tip accelerates to a velocity of approximately $1.5\sqrt{gh_0}$ prior to impact on the vertical wall. Additionally, the wave

tip trajectory is altered by the gas that is forced from the cross-sectional area of the gas pocket.

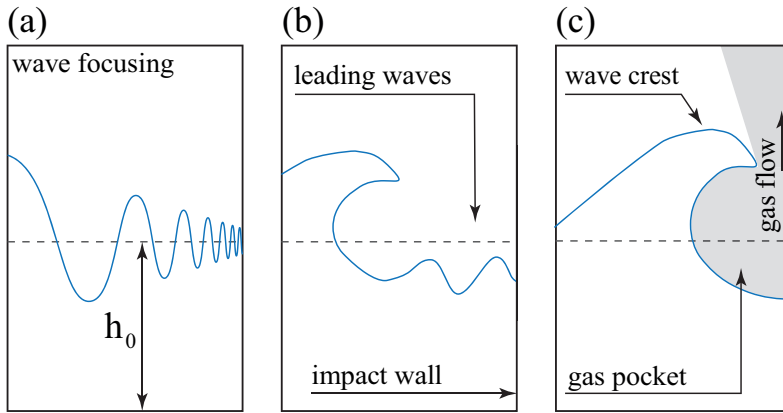


Figure 5.1: A schematic representation of a wave impact process. (a) A wave is generated with a wave focusing technique in the wave flume of the Hydraulic Engineering Laboratory at the Delft University of Technology. The wave group with varying wave length and phase velocity focus on the focal point of the wave flume. (b) A large scale plunging breaking wave is generated with the wave focusing technique. Leading waves are observed to reflect from the wall prior to impact. (c) The globally repeatable plunging breaking wave approaches the impact wall. The wave crest encloses a gas pocket prior to its impact on the vertical wall. The reduction of the gas pocket volume results in a gas flow past the wave crest. (figure continues on facing page)

The global gas flow behavior is also similar over repeated measurements obtained on a single day. A vortex consistently develops over the leeward side (e.g., the backside) of the plunging breaking wave (fig. 5.2 d). The vortex separates from the crest of the breaking wave and lingers behind the wave crest in the stagnant air. The vortex development is comparable to that of a plunging breaking wave. The circulation increases up to separation and thereafter remains stationary. The development of circulation is typical for a vortex that eventually separates (Gharib et al., 1998). A dimensionless formation number often defines the moment of separation (e.g., saturation of the circulation). However, a typical formation number is not easily defined for the current measurements, as both length and velocity scales change simultaneously.

The bulk velocity of the air that is escaping between the wave crest and the impact wall is determined both from the velocity measurements and from mass conservation based on the volume reduction of the air pocket (assuming incompressible flow). However, the bulk velocity determined from the measurements initially appears to be significantly lower than the mass conservation estimate. The PIV measurements are not resolved near the wave crest tip due to the absence of seeding particles and due to the limited PIV resolution. A fit of the measured velocity profile with a

potential flow past a bluff body (i.e., the flow over a cylinder ¹) greatly improves the bulk velocity estimate (i.e., within 2% value derived from mass conservation). The gas velocity near the wave crest tip is approximately a factor 2 higher than the bulk velocity estimate, which results in an earlier onset of instability development (fig. 5.2 d).

The source of impact pressure variability in repeated wave impact experiments is often suggested to be the instability development on the wave crest. Typically, the shear force induced by the strong gas flow over the wave crest is postulated to be the source wave impact pressure variability. In this work, two additional mechanisms for impact pressure variability are identified, that are triggered by wave tip acceleration (fig. 5.2 d.3) and gas flow separation (fig. 5.2 e).

The first mechanism for wave impact pressure variability is the result of an acceleration of the wave crest tip (fig. 5.2 d). The wave tip is deflected by the strong gas flow that is forced from the gas pocket moments before impact on the vertical wall. The wave tip is thereby stretched into a thin liquid sheet (i.e., flapping liquid sheet), that is destabilized by an initial Kelvin-Helmholtz instability (Villermaux et al., 2002) (fig. 5.2 d.1). The wave that travels over the length of the thin liquid sheet, see figure 5.2 d.2, results in an acceleration of the tip of the liquid sheet. The acceleration, see figure 5.2 d.3, triggers the development of an additional Rayleigh-Taylor instability, which results in the formation of equally spaced liquid filaments (i.e., liquid fingers). The spanwise wavelength of the liquid filaments is well approximated by $\lambda_{\perp} \sim (\gamma / \rho_a \dot{x}_{wt}^2) (\rho_a / \rho_l)^{1/3}$ (Villermaux et al., 2002). The liquid filaments develop consistently during all wave impacts but with variable filament lengths. The development of these liquid filaments is an indication of an instability that results in wave impact pressure variability with varying density ratio (ρ_a / ρ_l) and surface tension (γ).

The second mechanism for wave impact pressure variability is the result of flow separation near the wave crest tip (fig. 5.2 e). The local gas flow separates from the wave crest tip prior to impact on the vertical wall and a secondary vortex develops near the wave crest tip for all measurements. However, breakdown of the secondary vortex is observed for wave crests that are initially disturbed. The breakdown results in the formation of a shear layer, which is comparable to a wing that experiences stall. On the other hand, the secondary vortex develops further when the wave crest is initially smooth. The lift induced by the secondary vortex remains, which results in a significant displacement of the wave crest tip. The initial smoothness of the wave crest defines the lifetime of the secondary vortex. The lifetime of the secondary vortex defines the duration of enhanced lift, and thereby the wave impact pressure variability.

¹ The velocity on the surface of a cylinder at an angle of 90 degrees with respect to a uniform potential flow is two times the uniform flow velocity.

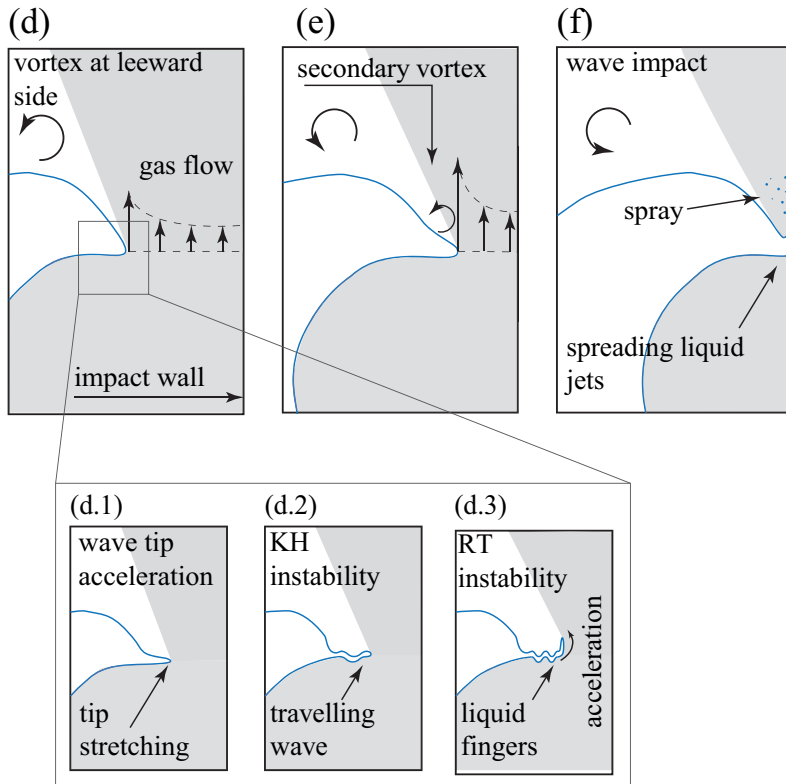


Figure 5.2: A schematic representation of a wave impact process. (d) The wave progresses towards the impact wall. The gas flow significantly increases near the wave crest tip, as the wave tip to impact wall distance decreases. The velocity profile resembles that of a flow past a cylinder in an uniform potential flow. A vortex is additionally generated at the wave crest, which separates when the vortex is saturated (i.e., when the circulation reaches a constant value). Two additional mechanism for wave impact pressure variability are identified; the formation of liquid fingers (d.1 to d.2) and the formation of a secondary vortex (e). (d.1) The wave tip accelerates and the tip stretches into a thin liquid sheet. (d.2) The wave tip is destabilized by an initial Kelvin-Helmholtz instability. (d.3) The traveling wave accelerates the wave tip, which triggers a Rayleigh-Taylor instability. Thereafter, liquid fingers are observed to grow over the spanwise direction of the wave tip. (e) A secondary vortex develops near the wave crest tip with a lifetime that is dependent on the “smoothness” of the wave crest. (f) Finally, the wave impacts on the wall. The impact results in the formation of a spray cloud and the two spreading liquid jets are formed at location of impact as the wave progresses.

In conclusion, the global wave behavior is repeatable for measurements with minimal *system variability*. The global gas flow behavior is also comparable for repeated wave impact experiments. On the other hand, the local flow of both the wave and the gas can be significantly different over repeated wave impact experiment with minimal *system variability*. Two additional mechanism of wave impact pressure variability are identified. The deflection of the wave crest tip by the strong gas flow results in the development of liquid filaments through a Rayleigh-Taylor mechanism with a predictable spanwise wavelength. Additionally, gas flow separation close to the wave crest tip results in the development of a secondary vortex. The lifetime of the secondary vortex depends on the initial smoothness of the wave crest; a smooth wave crest results in a long lifetime of the secondary vortex and a significant displacement of the wave crest tip.

5.2 PERSPECTIVES ON FUTURE RESEARCH

The generation of repeatable waves is not trivial. On the other hand, waves can be generated that are globally repeatable when the *system variability* is minimized. A globally repeatable wave can be obtained over the course of a day, but day-to-day variations were still present. This resulted in variations of the global wave shape over multiple days. In this thesis, measurements are therefore analyzed on a day-to-day basis, which limits the number of realizations in a set of measurements. The number of realizations in a set was approximately limited to 12, due to the required settling time between experiments. A natural next step is to minimize the *system variability* even further so that repeatable waves can be obtained without day-to-day variations. This can be achieved by having better control of the water height, the piston motion, and the atmospheric conditions. The number of measurements that can be obtained on a single day is limited by the number of hours in a working day. Additionally, a computer-controlled measurement facility can be used to perform more measurements on a single day. For example, the *system variability* can be minimized even further in the Atmosphere at Marin, where the atmospheric conditions, the water depth and piston motion are monitored in more detail (Novaković et al., 2020). In such a facility, it would be interesting to investigate if the observed *hydrodynamic variability* also exists for waves that are generated with even lower *system variability*.

In the current work, a wave focusing method is used with small amplitude and short wavelength waves that reflect of the wall prior to impact of the focused wave. The additional waves introduce an initial wave-wave interaction, that is postulated to increase the wave impact pressure variability (Novaković et al., 2020). The wave focusing spectrum can be optimized to reduce and/or negate the initial wave-wave interaction (Novaković et al., 2020; Kimmoun et al., 2010). The advantage of this altered wave spectrum is that it can be easily applied in different experimental facilities. On the other hand, the initial wave-wave interaction is probably not the source of the local wave crest variability. The waves are expected to be smoother

without the presence of an initial wave-wave interaction, which may even enhance the wave impact pressure variability (see chapter 4). The relevance of the initial wave-wave interaction on the wave impact pressure variability should be investigated in more detail.

In chapter 4 it was shown that the formation of secondary vortices results in an additional wave tip deflection, which was introduced as a second mechanism for wave impact variability. The formation of the secondary vortices depends, among other things, on the “smoothness” of the wave crest prior to impact. Interestingly, the non-smooth wave crest (e.g., the formation of a disturbance on the wave crest) was only observed in a sub-set of the presented experimental measurements. The wave shapes in this sub-set were globally similar to the other measurements obtained on that day (i.e., the cases with and without a disturbance). The source of the disturbance should be further investigated. For example, if the initial wave-wave interactions do not result in the additional disturbance; it could be that a Kelvin-Helmholtz instability is triggered earlier than expected. The particle image velocimetry measurements indicated that the velocity near the wave crest tip is almost two times that of the bulk velocity. The condition for the formation of Kelvin-Helmholtz instabilities is thereby satisfied earlier than expected. Nevertheless, the relation between the wave crest shape (e.g., smoothness and angle) and the lifetime of the secondary vortex should be further investigated. A dimensionless parameters, such as the formation number, would be of interest to generalize the findings in this thesis. However, a dimensionless formation number could not easily be defined with suitable length and velocity scales. If such a number can be defined, it would be interesting to determine a possible relation with the lifetime of the secondary vortex and the wave impact pressure variability.

A plunging breaking waves is generated at a water depth of $h_0 = 500$ mm with only a single steering signal. A natural, but time-consuming, next step is to repeat this work for a wider range of wave conditions. For example, the wave crest geometry should be altered to validate the existence of the two mechanisms that increase the wave impact pressure variability for different wave crest geometries. The flapping liquid sheet was observed in additional sets of measurements (not reported in this thesis), but it should also be confirmed for different wave conditions (e.g., different wave crest geometries and wave heights). On the other hand, the formation of equally spaced fingers was already qualitatively reported in literature at different experimental length scales (e.g., λ parameters), for different density ratios (ρ_a / ρ_l), and for different surface tension values (γ). The theoretical prediction that estimate the spanwise wavelength of the liquid fingers should be confirmed for a wider range of conditions. Additionally, the relation between the formation of these spanwise liquid fingers and the gas flow should be further investigated. For example, what is the result of a strong cross flow and/or the formation of secondary vortices on the spanwise wavelength? These measurements could be performed without a wave flume, on a laboratory scale with a dedicated experimental set-up. The measurements in this dedicated experimental set-up can be conducted with minimal *system variability* and with more prevalent experimental techniques.

In chapter 1 it was stated that understanding wave impact variability is essential to minimize the risk of sloshing damage during the transport of liquefied natural gas (LNG). LNG is transported at or near the phase boundary and changes in the pressure may result in phase transition. However, the effect of phase transition on wave impact pressure variability is still largely unknown. Numerical studies hint at an increase of the impact velocity and a decrease of the maximal pressure in the gas pocket (Ancellin et al., 2018a; Ancellin et al., 2019). On the other hand, there is a significant difference between the time scales of the thermal diffusion and the wave impact process, which Ancellin et al. (2018a) expects limits the effect of phase change. However, these numerical studies are all performed without modeling the development of instabilities on the wave crest. The liquid fingers that form on the wave crest create a larger surface area, which is expected to enhance phase transition. On the other hand, the formation of liquid fingers depends on the surface tension, which is expected to be negligible at the moment of phase transition. Nevertheless, the existence of liquid fingers on the crest of an impacting wave is relevant for wave impact pressure variability at atmospheric conditions. However, the effect of phase transition on the formation of instabilities and, thereby, the wave impact pressure variability when the fluid and gas are close to the phase transition point should be further investigated.

The wave tip is deflected by the formation of a secondary vortex, but the tip also observed to accelerate. In chapter 2, the wave tip is shown to experience an acceleration of approximately $a \sim 100 \text{ ms}^{-2}$ between $-20 \leq t \leq 0 \text{ ms}$ where $t = 0$ is the moment of wave impact on the vertical wall. The result of the acceleration on the impact pressure is unknown, as the acceleration can also result in additional wave tip instabilities. However, it would be interesting to further investigate the effect of the acceleration on the wave impact pressure. Additionally, the effect of surface tension and aeration on the acceleration of the wave tip should be further investigated. For example, an increase of the surface tension during droplet jetting can decelerate the jet in specific regimes (Rijn et al., 2019). It would be interesting to investigate if a decrease in surface tension results in an acceleration of the wave tip. Additionally, the combined effect of acceleration and aeration is interesting, as the wave impact pressure is lower for higher amounts of aeration (Bredmose et al., 2015). These measurements are difficult to perform during a wave impact as a decrease of the surface tension also enhances the wave fragmentation. Therefore, it would be interesting to investigate if the results obtained in droplet impact experiments can be extended to wave impact experiments.

A

QUANTIFICATION OF SURFACE TENSION

The change in fluid properties due to the addition of the particular fluorescent dye used for the stereo-PLIF is investigated. The static surface tension is measured with an adapted pendant drop method (Saad et al., 2016). The method minimizes the difference between the parameterized Young-Laplace equation and an experimentally obtained profile to estimate the static surface tension value. The experimental profile is determined from the shadowgraph of a pendant drop.

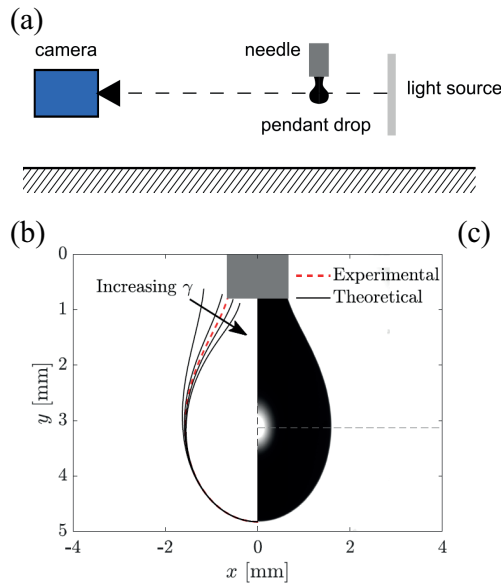


Figure A.1: Image processing to obtain the static surface tension from pendant drop images. (a) The experimental equipment used to obtain the shadowgraphy images. (b) The static surface tension of a water droplet is determined by minimizing the difference between the theoretical and experimental profile. (c) Image used to obtain the experimental profile for the minimization.

The pendant drop is suspended from a blunt tip needle (Fig. A.1a). The droplet volume is controlled with a syringe pump (101 syringe infusion pump, KD Scientific), allowing volume adjustments of $600 \text{ } \mu\text{L s}^{-1}$. The droplet is imaged with a CCD camera (VC-Imager Pro X 4M, LaVision) equipped with a long-distance microscope (QM 1 Long Distance Microscope, Questar). The back light illumination (OSL2 High-Intensity Fiber-Coupled Illuminator, Thorlabs) is uniform over the entire field-of-view of $5 \times 5 \text{ mm}$. The edge is easily obtained with a gradient-based edge detection procedure (Fig. A.1c).

The static surface tension is determined by minimizing the difference between the theoretical and experimental profile (Fig. A.1b). The static surface tension of water-air at $T = 21.3^\circ\text{C}$ is measured as $\gamma = 72.58 \text{ mN m}^{-1}$. The influence of Rhodamine 6G with increasing molar concentration (c_i) has previously been investigated, where it was shown that there is a negligible effect for practical concentrations (André et al., 2015). The influence of Rhodamine WT is investigated over a similar concentration span (Fig. A.2). The static surface tension value is slightly overestimated, but the trend is similar to the previous work. The effect on the static surface tension is limited for the current application of the stereo-PLIF system, as indicated by the filled marker (■) (Fig. A.2). However, the dynamic surface tension needs to be investigated for cases where compression can locally alter the surfactant concentration.

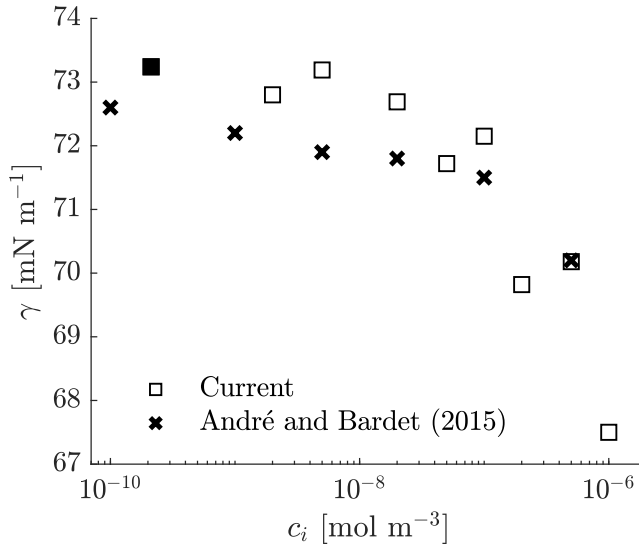


Figure A.2: Surface tension measurements with the pendant drop method. The current measurements show the dependency of surface tension on the addition of Rhodamine WT. This is compared to the dependency of Rhodamine 6G (André et al., 2015). The concentration used in the experiments is indicated by the filled marker (■).

B

INTERFEROMETRIC PARTICLE IMAGING

An *interferometric particle imaging* (IPI) technique is used to determine the tracer particle size (Damaschke et al., 2005; Damaschke et al., 2002; Eckeveld et al., 2018). The particles are generated with a commercial ultrasonic humidifier (UHW, Medisana). The tracer particles are illuminated with a 1 mm thick laser light sheet generated by a high-speed Nd:YLF laser (LDY 304 PIV laser, Litron) with a perpendicular polarization and a wavelength of $\lambda = 532$ nm. Images are acquired with an high-speed CMOS camera (Fastcam APX-RS, Photron) equipped with a 200 mm Micro-Nikkor objective at an f-number of $f^\# = 4$ that results in an aperture for the lens system of $d_a = f/f^\# = 50$ mm. The camera is initially focused on a two-level double sided calibration plate (Type 58, LaVision) to obtain a magnification of $M_0 = 1.2$ at a distance of $z = 424$ mm. After calibration the optical system is slightly defocused to obtain interference images of the particles. The camera is placed at an angle of $\theta_r = 90^\circ$ with respect to the laser light sheet to increase the signal to noise ratio for the selected polarization (Damaschke et al., 2005). There is a direct relation between the number of fringes (N) and the particle size (d_p). For a refractive index ratio ($m = n_l/n_g > 1$) and an aperture size that is small compared to the focal distance ($d_a/z \ll 1$) the relation is (Damaschke et al. (2002)):

$$d_p = \frac{2\lambda z N}{d_a} \left[\cos(\theta_r/2) + \frac{m \sin(\theta_r/2)}{\sqrt{m^2 - 2m \cos(\theta_r/2) + 1}} \right]^{-1} \quad (\text{B.1})$$

with $m = n_l/n_g = 1.33/1$ the ratio of the refractive index of water and air. The particle size is solely determined by the optical choices in the set-up, such as the focal distance and the aperture size. The viewing angle only defines the signal to noise ratio of the measured particle images. However, the IPI technique is not well suited for dense sprays. In the current work, the spray was diluted to obtain usable particle images. The PDF of the particle size is shown in figure B.1, where the distribution has an average particle size of $\bar{d}_p = e^{\mu + \sigma^2/2} \approx 9.8 \mu\text{m}$.

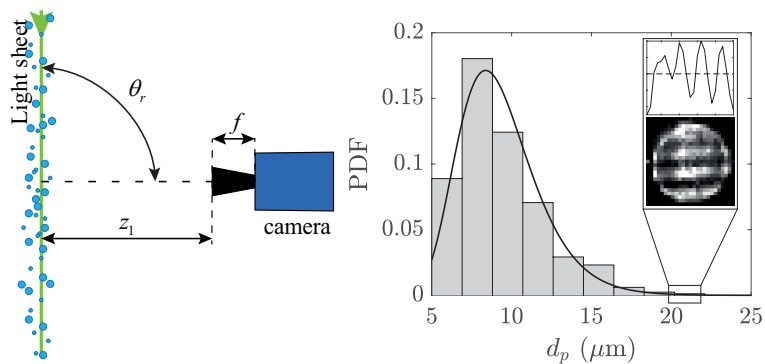


Figure B.1: The probability density function (PDF) of the tracer particle size is shown. A typical log-normal fit is applied to the data with a mean of $\mu = 2.2 \mu\text{m}$ and a standard deviation of $\sigma = 0.27 \mu\text{m}$. The inset shows a typical particle image with a normalized interference pattern.

C

SYMMETRIC PHASE ONLY FILTERING

The symmetric phase only filter is used, with a window function defined by (Wernet (2005)):

$$W(p, q) = \frac{1}{\sqrt{|S_1(p, q)|} \sqrt{|S_2(p, q)|}} \quad (\text{C.1})$$

with $|S_i|$ the real part of the Fourier transform. The Fourier transform of the interrogation window located at coordinates p, q is defined as $S_i(p, q) = |S_i(p, q)|e^{-i\phi(p, q)}$ for camera i . The window function (i.e., filter) is only applied to a single image Fourier transformed of the image pair.

The correlation peak of the symmetric phase only filter is compared to a typical correlation method in figure C.1. A single interrogation window is selected for a typical PIV image. The correlation peak is determined with both a normal cross correlation (fig. C.1 a) and a phase only filtered correlation (fig. C.1 b). The correlation peak is clearly identified for the phase only filtered window, whereas it is unclear in the original image.

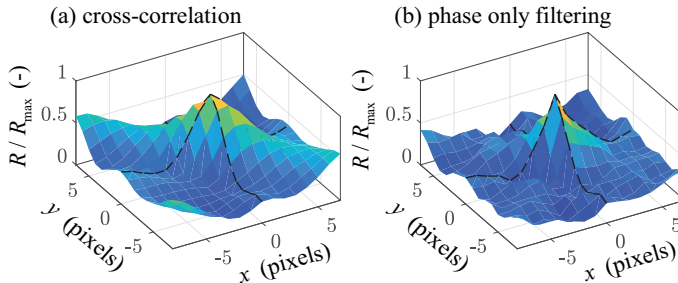


Figure C.1: The correlation peak is determined at a typical location near the wave crest tip for FOV1 at the final pass of the PIV algorithm. (a) The correlation peak is typically determined with a cross correlation PIV algorithm. (b) The correlation peak is determined with a symmetric phase-only filter. The correlation peak is clearly defined when the image data is filtered with a symmetric phase-only filter.

REFERENCES

- Abrahamsen, B. C. and O. M. Faltinsen (2011). "The effect of air leakage and heat exchange on the decay of entrapped air pocket slamming oscillations." In: *Phys. Fluids* 23.10, p. 102107.
- Adrian, R. J. and J. Westerweel (2011). *Particle image velocimetry*. 30. Cambridge University Press.
- Almeida, E. de and B. Hofland (2020). "Validation of pressure-impulse theory for standing wave impact loading on vertical hydraulic structures with short overhangs." In: *Coastal Eng.* 159, p. 103702.
- Ancellin, M., L. Brosset, and J. M. Ghidaglia (2018a). "Numerical simulation of wave impacts with interfacial phase change: An isothermal averaged model." In: *Eur. J. Mech. B. Fluids* 72, pp. 631–644.
- Ancellin, M., L. Brosset, and J. M. Ghidaglia (2018b). "Numerical Study of Phase Change Influence on Wave Impact Loads in LNG Tanks on Floating Structures." In: *Int. Conf. Offshore Mech. Arctic Eng.*
- Ancellin, M., L. Brosset, and J. M. Ghidaglia (2019). "Numerical simulation of wave impacts with interfacial phase change: An interface reconstruction scheme." In: *Eur. J. Mech. B. Fluids* 76, pp. 352–364.
- André, M. A. and P. M. Bardet (2014). "Velocity field, surface profile and curvature resolution of steep and short free-surface waves." In: *Exp. Fluids* 55.4, p. 1709.
- André, M. A. and P. M. Bardet (2015). "Interfacial shear stress measurement using high spatial resolution multiphase PIV." In: *Exp. Fluids* 56.6.
- Aronietis, R. et al. (2016). "Forecasting port-level demand for LNG as a ship fuel: the case of the port of Antwerp." In: *J. Ship Trade* 1.1.
- Bagnold, R. A. (1939). "Interim report on wave-pressure research." In: *J. Inst. Civ. Eng.*, pp. 202–226.
- Behruzi, P. et al. (2017). "Modeling of Impact Waves in LNG Ship Tanks." In: *International Journal of Offshore and Polar Engineering* 27.01, pp. 18–26.
- Belden, J and A. H. Techet (2011). "Simultaneous quantitative flow measurement using PIV on both sides of the air–water interface for breaking waves." In: *Exp. Fluids* 50.1, pp. 149–161.
- Benetazzo, A. (2006). "Measurements of short water waves using stereo matched image sequences." In: *Coastal Eng.* 53.12, pp. 1013–1032.
- Benetazzo, A. et al. (2012). "Offshore stereo measurements of gravity waves." In: *Coastal Eng.* 64, pp. 127–138.
- Blackmore, P. A. and P. J. Hewson (1984). "Experiments on full-scale wave impact pressures." In: *Coastal Eng.* 8.4, pp. 331–346.

- Bogaert, H. (2018). "An experimental investigation of sloshing impact physics in membrane LNG tanks on floating structure." PhD thesis.
- Bogaert, H. et al. (2010). "Sloshing and scaling: results from the sloshel project." In: *Int. Ocean Polar Eng. Conf., 20th, 20-25 June, Beijing, China*.
- Bonmarin, P. (1989). "Geometric properties of deep-water breaking waves." In: *J. Fluid Mech.* 209, pp. 405-433.
- Bredmose, H., G. N. Bullock, and A. J. Hogg (2015). "Violent breaking wave impacts. Part 3. Effects of scale and aeration." In: *J. Fluid Mech.* 765, pp. 82-113.
- Brücker, Ch (1996). "3-D scanning-particle-image-velocimetry: technique and application to a spherical cap wake flow." In: *Appl. Sci. Res.* 56.2-3, pp. 157-179.
- Buchner, B. and T. Bunnik (2007). "Extreme Wave Effects on Deepwater Floating Structures." In: *Offshore Technology Conference*.
- Buckley, M. P. and F. Veron (2016). "Structure of the airflow above surface waves." In: *J. Phys. Oceanogr.* 46.5, pp. 1377-1397.
- Buckley, M. P. and F. Veron (2017). "Airflow measurements at a wavy air-water interface using PIV and LIF." In: *Exp. Fluids* 58.11.
- Bullock, G. N. et al. (2001). "The influence of air and scale on wave impact pressures." In: *Coastal Eng.* 42.4, pp. 291-312.
- Bullock, G. N. et al. (2007). "Violent breaking wave impacts. part 1: results from large-scale regular wave tests on vertical and sloping walls." In: *Coast. Eng.* 54.8, pp. 602-617.
- Chakraborty, p., s. Balachandar, and r. j. Adrian (2005). "On the relationships between local vortex identification schemes." In: *J. Fluid Mech.* 535, pp. 189-214.
- Chan, E. S. and W. K. Melville (1988). "Deep-water plunging wave pressures on a vertical plane wall." In: *Proc. R. Soc. Lond. A-Math. Phy.* 417.1852, pp. 95-131.
- Chen, G. et al. (1999). "Two-dimensional Navier-Stokes simulation of breaking waves." In: *Physics of Fluids* 11.1, pp. 121-133.
- Cobelli, P. J. et al. (2009). "global measurement of water waves by fourier transform profilometry." In: *Exp. Fluids* 46.6, pp. 1037-1047.
- Cooker, M. J. and D. H. Peregrine (1995). "Pressure-impulse theory for liquid impact problems." In: *J. Fluid Mech.* 297, pp. 193-214.
- Cuomo, G. et al. (2010). "Breaking wave loads at vertical seawalls and breakwaters." In: *Coastal Eng.* 57.4, pp. 424-439.
- Dabiri, D. and M. Gharib (1997). "Experimental investigation of the vorticity generation within a spilling water wave." In: *Journal of Fluid Mechanics* 330, pp. 113-139.
- Dabiri, D. and M. Gharib (2001). "Simultaneous free-surface deformation and near-surface velocity measurements." In: *Exp. Fluids* 30.4, pp. 381-390.
- Damaschke, N., H. Nobach, and C. Tropea (2002). "Optical limits of particle concentration for multi-dimensional particle sizing techniques in fluid mechanics." In: *Experiments in Fluids* 32.2, pp. 143-152.
- Damaschke, N. et al. (2005). "Multi-dimensional particle sizing techniques." In: *Experiments in Fluids* 39.2, pp. 336-350.

- Delorme, L. et al. (2009). "A set of canonical problems in sloshing, Part I: Pressure field in forced roll—comparison between experimental results and SPH." In: *Ocean Eng.* 36.2, pp. 168–178.
- Dias, F. and J. M. Ghidaglia (2018). "Slamming: recent progress in the evaluation of impact pressures." In: *Annu. Rev. Fluid Mech.* 50.1, pp. 243–273.
- Douxchamps, D. et al. (2005). "Stereoscopic and velocimetric reconstructions of the free surface topography of antidune flows." In: *Exp. Fluids* 39.3, pp. 535–553.
- Duncan, J. H. et al. (1999). "Gentle spilling breakers: crest profile evolution." In: *J. Fluid Mech.* 379, pp. 191–222.
- Eckveld, A. C. van et al. (2018). "Annular two-phase flow in vertical smooth and corrugated pipes." In: *International Journal of Multiphase Flow* 109, pp. 150–163.
- Eckstein, A. C., J. Charonko, and P. Vlachos (2008). "Phase correlation processing for DPIV measurements." In: *Experiments in Fluids* 45.3, pp. 485–500.
- Eldredge, J. D. and A. R. Jones (2019). "Leading-Edge Vortices: Mechanics and Modeling." In: *Annual Review of Fluid Mechanics* 51.1, pp. 75–104.
- ESA (2020). *Sloshing in space*. www.esa.int.
- Etienne, S., Y. M. Scolan, and L. Brosset (2018). "Numerical Study of Density Ratio Influence on Global Wave Shapes Before Impact." In: *Int. Conf. Offshore Mech. Arctic Eng.*
- Faltinsen, O. M., A. N. Timokha, and O. Rognebakke (19, 2009). *Sloshing*. Cambridge University Press. 606 pp.
- Firoozkoobi, R., B. C. Abrahamsen, and O. M. Faltinsen (2017). "Study of an Entrapped Air Pocket due to Sloshing Using Experiments and Numerical Simulations." In: *Int. Conf. Offshore. Mech. Arctic Eng.*
- Fortin, S. et al. (2020). "Numerical Study of the Influence of Weber and Reynolds Numbers on the Development of Kelvin-Helmholtz Instability." In: *Int. J. Offshore Polar Eng.* 30.02, pp. 129–140.
- Friedman, J. H., J. L. Bentley, and R. A. Finkel (1977). "An algorithm for finding best matches in logarithmic expected time." In: *ACM Transactions on Mathematical Software (TOMS)* 3.3, pp. 209–226.
- Frihat M. and Brosset, L. and J. M. Ghidaglia (2017). "Experimental study of surface tension effects on sloshing impact loads." In: *Proc. Int. Workshop Water Waves Float. Bodies, 32nd, 23–26 Apr., Dalian, China*.
- Frihat, M. et al. (2016). "Variability of impact pressures induced by sloshing investigated through the concept of 'singularization'." In: *Int. Ocean Polar Eng. Conf., 26th, 26 June–2 July, Rhodes, Greece*.
- Gavory, T. and P. E. de Seze (2009). "Sloshing In Membrane LNG Carriers And Its Consequences From a Designer's Perspective." In: *ISOPE*.
- Gellert, W. et al., eds. (1989). *VNR concise encyclopedia of mathematics*. Van Nostrand Reinhold.
- Ghadirian, A. and H. Bredmose (2019). "Pressure impulse theory for a slamming wave on a vertical circular cylinder." In: *J. Fluid Mech.* 867.
- Gharib, M., E. Rambod, and K. Shariff (1998). "A universal time scale for vortex ring formation." In: *Journal of Fluid Mechanics* 360, pp. 121–140.

- Gomit, G. et al. (2013). "Free surface measurement by stereo-refraction." In: *Exp. Fluids* 54.6.
- Gomit, G. et al. (2015). "Large-scale free surface measurement for the analysis of ship waves in a towing tank." In: *Exp. Fluids* 56.10.
- Gonzalez, R. C., R. E. Woods, and S. L. Eddins (2009). *digital image processing using MATLAB*. second. Gatesmark Publishing.
- Graftieaux, L., M. Michard, and N. Grosjean (2001). "Combining PIV, POD and vortex identification algorithms for the study of unsteady turbulent swirling flows." In: *Measurement Science and Technology* 12.9, pp. 1422–1429.
- Gui, L., H. Yoon, and F. Stern (2014). "Techniques for measuring bulge–scar pattern of free surface deformation and related velocity distribution in shallow water flow over a bump." In: *Exp. Fluids* 55.4, p. 1721.
- Guilcher, P. M., Y. Jus, and L. Brosset (2018). "2D Simulations of Breaking Wave Impacts on a Flat Rigid Wall—Part 2: Influence of Scale." In: *Int. Ocean Polar Eng. Conf., 28th, 10–15 June, Sapporo, Japan*.
- Guilcher, P. M. et al. (2014). "2D simulations of breaking wave impacts on a flat rigid wall—part 1: influence of the wave shape." In: *Int. Ocean Polar Eng. Conf., 24th, 15–20 June, Busan, Korea*. International Society of Offshore and Polar Engineers.
- Hattori, M., A. Arami, and T. Yui (1994). "Wave impact pressure on vertical walls under breaking waves of various types." In: *Coast. Eng.* 22.1-2, pp. 79–114.
- Henry, A. et al. (2015). "The Vertical Distribution and Evolution of Slam Pressure on an Oscillating Wave Surge Converter." In: *Int. Conf. Offshore Mech. Arctic Eng.*
- Hicks, P. D. (2018). "LNG-solid impacts with gas cushioning and phase change." In: *J. Fluids Struct.* 80, pp. 22–36.
- Hochareon, P. et al. (2004). "Wall Shear-Rate Estimation Within the 50cc Penn State Artificial Heart Using Particle Image Velocimetry." In: *Journal of Biomechanical Engineering* 126.4, pp. 430–437.
- Hofland, B., M. Kaminski, and G. Wolters (2010). "Large scale wave impacts on a vertical wall." In: *Coast. Eng. Proc.* 1.32, p. 15.
- Hori, T. and J. Sakakibara (2004). "high-speed scanning stereoscopic PIV for 3d vorticity measurement in liquids." In: *Meas. Sci. Technol.* 15.6, pp. 1067–1078.
- Hull, P. and G. Müller (2002). "An investigation of breaker heights, shapes and pressures." In: *Ocean Engineering* 29.1, pp. 59–79.
- Hwung, H. H., C. A. Kuo, and C. H. Chien (2009). "Water surface level profile estimation by image analysis with varying overhead camera posture angle." In: *Meas. Sci. Technol.* 20.7, p. 075104.
- Ibrahim, R. A. (2020). "Assessment of breaking waves and liquid sloshing impact." In: *Nonlinear Dyn.* 100.3, pp. 1837–1925.
- International Energy Agency (2020). *Gas 2020*. Tech. rep. IEA.
- International Gas Union (2020). *Global gas report 2020*. Tech. rep. IGU.
- Jähne, B. and H. Haußecker (1998). "air-water gas exchange." In: *Annu. Rev. Fluid Mech.* 30.1, pp. 443–468.
- Karimi, M. R. et al. (2015). "Effect of ullage gas on sloshing, Part I: Global effects of gas–liquid density ratio." In: *Eur. J. Mech. B. Fluids* 53, pp. 213–228.

- Karimi, M. R. et al. (2016). "Effect of ullage gas on sloshing, Part II: Local effects of gas-liquid density ratio." In: *Eur. J. Mech. B. Fluids* 57, pp. 82-100.
- Kimmoun, O., A. Ratouis, and L. Brosset (2010). "Sloshing and scaling: experimental study in a wave canal at two different scales." In: *Int. Ocean Polar Eng. Conf., 20th, 20-25 June, Beijing, China*.
- KNRM (2019). *Reddingsboot Arie Visser*. www.knrm.nl. Accessed: 2020-09-18.
- Korobkin, A. A., T. I. Khabakhpasheva, and S. Malenica (2017). "Maximum stress of stiff elastic plate in uniform flow and due to jet impact." In: *Phys. Fluids* 29.7, p. 072105.
- Lafeber, W., H. Bogaert, and L. Brosset (2012a). "Comparison of wave impact tests at large and full scale: results from the Sloskel project." In: *Int. Ocean Polar Eng. Conf., 22nd, 17-22 June, Rhodes, Greece*.
- Lafeber, W., H. Bogaert, and L. Brosset (2012b). "elementary loading processes (ELP) involved in breaking wave impacts: findings from the Sloskel project." In: *Int. Ocean Polar Eng. Conf., 22nd, 17-22 June, Rhodes, Greece*.
- Lamb, H. (1993). *Hydrodynamics*. Cambridge university press.
- Lawson, N. J. and J. Wu (1997). "Three-dimensional particle image velocimetry: experimental error analysis of a digital angular stereoscopic system." In: *Meas. Sci. Technol.* 8.12, pp. 1455-1464.
- Liu, H., S. Shah, and W. Jiang (2004). "On-line outlier detection and data cleaning." In: *Computers & Chemical Engineering* 28.9, pp. 1635-1647.
- Liu, J., J. D. Paul, and J. P. Gollub (1993). "Measurements of the primary instabilities of film flows." In: *J. Fluid Mech.* 250.-1, p. 69.
- Longuet-Higgins, M. S. (1995). "On the disintegration of the jet in a plunging breaker." In: *J. Phys. Oceanogr.* 25.10, pp. 2458-2462.
- Lubin, P. et al. (2019). "Discussion on instabilities in breaking waves: Vortices, air-entrainment and droplet generation." In: *Eur. J. Mech. B. Fluids* 73, pp. 144-156.
- Lugni, C., M. Brocchini, and O. M. Faltinsen (2006). "Wave impact loads: The role of the flip-through." In: *Phys. Fluids* 18.12, p. 122101.
- Lugni, C., M. Brocchini, and O. M. Faltinsen (2010a). "Evolution of the air cavity during a depressurized wave impact. II. The dynamic field." In: *Phys. Fluids* 22.5, p. 056102.
- Lugni, C. et al. (2010b). "Evolution of the air cavity during a depressurized wave impact. I. The kinematic flow field." In: *Phys. Fluids* 22.5, p. 056101.
- Lugni, C. et al. (2014). "Hydroelastic slamming response in the evolution of a flip-through event during shallow-liquid sloshing." In: *Phys. Fluids* 26.3, p. 032108.
- MARIN (2020). *The Atmosphere*. www.MARIN.nl. Accessed: 2020-09-24.
- Marmottant, P. and E. Villermaux (2004). "On spray formation." In: *J. Fluid Mech.* 498, pp. 73-111.
- Meerkerk, M. van, C. Poelma, and J. Westerweel (2020a). "Scanning stereo-PLIF method for free surface measurements in large 3D domains." In: *Exp. Fluids* 61.1.
- Meerkerk, M. van et al. (2020b). "Experimental investigation of wave tip variability of impacting waves." Submitted to *Physics of Fluids*.

- Mei, R. (1996). "Velocity fidelity of flow tracer particles." In: *Experiments in Fluids* 22.1, pp. 1–13.
- Moisy, F., M. Rabaud, and K. Salsac (2009). "A synthetic Schlieren method for the measurement of the topography of a liquid interface." In: *Exp. Fluids* 46.6, p. 1021.
- New, A. L. (1983). "A class of elliptical free-surface flows." In: *J. Fluid Mech.* 130, pp. 219–239.
- Novaković, V. et al. (2020). "Study of global wave repeatability in the new Multiphase Wave Lab (MWL)." In: *Submitted to Int. Ocean Polar Eng. Conf., 30th, 12-16 Oct., Shanghai, China.*
- Orfanidis, S. (1995). *Introduction to Signal Processing*. Prentice Hall.
- Otsu, N. (1979). "A threshold selection method from gray-level histograms." In: *IEEE transactions on systems, man, and cybernetics* 9.1, pp. 62–66.
- Peregrine, D. H. (2003). "Water-wave impact on walls." In: *Annu. Rev. Fluid Mech.* 35.1, pp. 23–43.
- Peters, I. R., D. van der Meer, and J. M. Gordillo (2013). "Splash wave and crown breakup after disc impact on a liquid surface." In: *J. Fluid Mech.* 724, pp. 553–580.
- Pratt, V. (1987). "Direct least-squares fitting of algebraic surfaces." In: *ACM SIGGRAPH Computer Graphics* 21.4, pp. 145–152.
- Renzi, E., Y. Wei, and F. Dias (2018). "The pressure impulse of wave slamming on an oscillating wave energy converter." In: *J. Fluids Struct.* 82, pp. 258–271.
- Reul, N., H. Branger, and J.-P. Giovanangeli (1999). "Air flow separation over unsteady breaking waves." In: *Physics of Fluids* 11.7, pp. 1959–1961.
- Reul, N., H. Branger, and J.-P. Giovanangeli (2007). "Air Flow Structure Over Short-gravity Breaking Water Waves." In: *Boundary-Layer Meteorology* 126.3, pp. 477–505.
- Rijn, Cees van et al. (2019). "Particle image velocimetry inside emanating jets to study jet shape and evolution (abstract)." In: *APS Division of Fluid Dynamics*.
- Ross, S. and P. D. Hicks (2019). "A comparison of pre-impact gas cushioning and Wagner theory for liquid-solid impacts." In: *Phys. Fluids* 31.4, p. 042101.
- Saad, S. M. I. and A. W. Neumann (2016). "Axisymmetric Drop Shape Analysis (ADSA): An Outline." In: *Adv. Colloid Interface Sci.* 238, pp. 62–87.
- Savelsberg, R., A. Holten, and W. van de Water (2006). "Measurement of the gradient field of a turbulent free surface." In: *Exp. Fluids* 41.4, pp. 629–640.
- Soloff, S. M., R. J. Adrian, and Z. Liu (1997). "Distortion compensation for generalized stereoscopic particle image velocimetry." In: *Meas. Sci. Technol.* 8.12, p. 1441.
- Song, B. and C. Zhang (2018). "Boundary element study of wave impact on a vertical wall with air entrapment." In: *Eng. Anal. Boundary Elem.* 90, pp. 26–38.
- Song, B. and C. Zhang (2019). "Water column impact on a rigid wall with air cavity effects." In: *Phys. Fluids* 31.4, p. 042112.
- Song, Y. K. et al. (2013). "Experimental study on flow kinematics and impact pressure in liquid sloshing." In: *Exp. Fluids* 54.9.

- Souto-Iglesias, A., G. Bulian, and E. Botia-Vera (2015). "A set of canonical problems in sloshing. Part 2: Influence of tank width on impact pressure statistics in regular forced angular motion." In: *Ocean Eng.* 105, pp. 136–159.
- Su, M. Y. et al. (1982). "Experiments on nonlinear instabilities and evolution of steep gravity-wave trains." In: *J. Fluid Mech.* 124, pp. 45–72.
- Te Chow, V. (1959). *Open-channel hydraulics*. Vol. 1. McGraw-Hill New York.
- Techet, A. H. and A. K. McDonald (2005). "High speed PIV of breaking waves on both sides of the air-water interface." In: *6th International Symposium on Particle Image Velocimetry*, pp. 1–14.
- Tsubaki, R. and I. Fujita (2005). "Stereoscopic measurement of a fluctuating free surface with discontinuities." In: *Meas. Sci. Technol.* 16.10, pp. 1894–1902.
- Turney, D. E., A. Anderer, and S. Banerjee (2009). "a method for three-dimensional interfacial particle image velocimetry (3d-PIV) of an air–water interface." In: *Meas. Sci. Technol.* 20.4, p. 045403.
- Villermaux, E. and C. Clanet (2002). "Life of a flapping liquid sheet." In: *J. Fluid Mech.* 462, pp. 341–363.
- Vinje, T. and P. Brevig (1981). "Numerical simulation of breaking waves." In: *Adv. Water Resour.* 4.2, pp. 77–82.
- Wang, A. et al. (2018). "The impact of a deep-water plunging breaker on a wall with its bottom edge close to the mean water surface." In: *J. Fluid Mech.* 843, pp. 680–721.
- Wei, Y. et al. (2016). "Wave interaction with an Oscillating Wave Surge Converter. Part II: Slamming." In: *Ocean Eng.* 113, pp. 319–334.
- Wei, Z. J. et al. (2015). "Sloshing-induced slamming in screen-equipped rectangular tanks in shallow-water conditions." In: *Phys. Fluids* 27.3, p. 032104.
- Wellander, R., M. Richter, and M. Aldén (2014). "time-resolved (kHz) 3D imaging of OH PLIF in a flame." In: *Exp. Fluids* 55.6.
- Wernet, M. P. (2005). "Symmetric phase only filtering: a new paradigm for DPIV data processing." In: *Measurement Science and Technology* 16.3, pp. 601–618.
- Westerweel, J. (1994). "Efficient detection of spurious vectors in particle image velocimetry data." In: *Experiments in Fluids* 16.3-4, pp. 236–247.
- Whitham, G. B. (1977, 1999). *linear and nonlinear waves*. John Wiley & Sons. 658 pp.
- Wieneke, B. (2008). "Volume self-calibration for 3D particle image velocimetry." In: *Exp. Fluids* 45.4, pp. 549–556.
- Yung, T.-W. et al. (2010). "On the Physics of Vapor/Liquid Interaction During Impact on Solids." In: *Journal of Ship Research* 54.03, pp. 174–183.
- Zavadsky, A., A. Benetazzo, and L. Shemer (2017). "On the two-dimensional structure of short gravity waves in a wind wave tank." In: *Phys. Fluids* 29.1, p. 016601.
- Zhang, S., D. K. P. Yue, and K. Tanizawa (1996). "Simulation of plunging wave impact on a vertical wall." In: *J. Fluid Mech.* 327, pp. 221–254.
- Zhou, J. et al. (1999). "Mechanisms for generating coherent packets of hairpin vortices in channel flow." In: *J. Fluid Mech.* 387, pp. 353–396.

ACKNOWLEDGEMENTS

I owe gratitude to many people for the results presented in this thesis and for much more that this work does not show.

First of all, I would like to thank my daily supervisor and promotor Christian Poelma for guiding me over the past years. Not only did you support me with the scientific challenges of my PhD, but you were also invaluable as a mentor and coach. Your guidance proved to be essential during those moments that I could only “see bears on the road”. Apart from the personal support, your very broad experimental expertise combined with a fundamental understanding of multiphase fluid dynamics guided me through the process. Together, we also supervised numerous bachelor and master projects and these diversions from my actual research were invaluable and much appreciated. I valued - although not at those moments - your direct style of supervision, that you combined with an openness (i.e., open door policy) that I am grateful for. I also appreciate the freedom you gave me in pursuing my hobbies, that - on windy days - often resulted in the question: “what are you doing in the office?” (i.e., why are you not at the beach?).

I also want to express my gratitude to my second promotor Jerry Westerweel. I have always felt that you were available for a discussion about my experimental results, and - even though you may not remember it - for a discussion about my failed bachelor exam on fluid mechanics. I enjoyed our discussions during dinners, courses, and in the car on our way back from the PIV course. That much enjoyed journey also is a fitting description of the many meetings that we had during my PhD project. On those German roads we missed an exit and continued - at high velocity - in the wrong direction. However as always, it is the journey that is important not the destination¹. I valued your guidance and this thesis could have been doubled in size if I had taken the time to implement all your ideas.

During my research project I moved outside the typical fields of interest of the Aero- & Hydro Laboratory. My research required a fundamental and practical understanding of waves and their generation methods. Therefore, I appreciate the discussions with both Peter Wellens and Bas Hofland. Peter, you took the time to read my first manuscript, which resulted in a lively discussion on waves and their definitions. I valued your feedback on my manuscript and the numerous discussions that resulted. I also appreciate that you valued my expertise on free surface measurement techniques. Bas, without you this work could not have been completed. The delayed opening of the research facility at MARIN required us to look for alternatives. I appreciate that we were able to perform our measurements at

¹ Ralph Waldo Emerson, Self-Reliance

the *Hydraulic Engineering Laboratory*. Your positivity is amazing and, although you are not my promotor, you always took the time to both discuss the results of my experiments and contemplate life in general.

I would also like to acknowledge the numerous project partners of the SLING research project. During the course of my work I had the opportunity to visit many places, among which Paris became the most visited city. The numerous project meetings and - of course - dinners were often memorable. For example, we became specialized in playing “Koehandel” and learned that touching screens (e.g., displays for presenting) is strictly prohibited in France. I will never forget the French pronunciation of the English phrase: “do not touch the screen”. I want to thank - in no specific order - Reinier, Rien, Ronald, Utkarsh, Wout, and Yous. The circumstances of the last few months did not allow us to have our final meeting and game of “Koehandel” in person, which I hope we can make up for at a later moment.

A laboratory cannot function without the support staff. I especially want to thank Caroline for the random chats and of course for arranging all the administrative details. My work could not have been completed without the technical help of Jasper, who supplied many quick fixes to my designs. I hope you will one day use the coffee mug that you were gifted at the end of my master thesis. I want to acknowledge the help of Jan during the moments of electrical malaise and for that one moment you helped me mop the floor after I flooded the lab. Edwin, your help with the camera and laser equipment is especially valued. Often the issues with DaVis were resolved if you just came to visit, but sometimes we had to take apart and refurbish complete laser heads. I also want to extend my gratitude to Sander, Arno, Jaap, Pieter, and Frank the lab technicians of the Hydraulic Engineering Laboratory.

I had the honor of organizing an extended lab outing to Copenhagen together with Gem and Saad. The planning of this trip cost us several days and numerous meetings, but I enjoyed it a lot. The trip was well received and I want to thank both of you for this experience. I hope we keep in touch in our future careers! I want to specifically acknowledge Gem for all the professional and sometimes personal discussions. We have a different background and approach problems in our own way, but our approach to life is the same. I enjoyed our collaboration in the lab, which will hopefully result in a beautiful publication.

The (lab) life of a PhD candidate is not always easy and often involves numerous hours behind a screen or in the lab solving problems that you later think could have been easily avoided. The support and distraction of my colleagues was essential for the completion of this work. I specifically want to thank Reinier Bos en Marc Fransen for their support during our - informal - coffee dates. During the course of a PhD project you meet many people both in and outside of your own laboratory. Thank you, Amitosh, Andries, Angeliki, Ankur, Arnoud, Bidhan, Bob, Caroline, Christian, Daniel, Daniele, Edwin, Ellert, Ermano, Ernst Jan, Florian, Gem, Gerrit, Gosse, Greta, Guillermo, Haoyu Li, Henk, Jan, Jasper, Jerke, John, Junaid, Koen, Lina, Luuk, Manu, Mark, Martin, Mathieu, Maurice, Melika, Parviz, Pedro, Pepijn, René, Rob, Ruud, Saad, Sören, Sudarshan, Swaraj, Tariq, Teng, Willian, Wim-Paul, Wout,

Wouter, Xuexue, Yavuz, and Yuk Man. I will never forget all the coffee talks, the coffee at 10, the Christmas events, the Game of Thrones episodes that we watched together, and all the other events.

I am very thankful to the many friends that have supported me both knowingly and unknowingly over the past years. Natuurlijk ben ik ook heel dankbaar voor mijn familie. “De kloek” (mijn moeder) en “die ouwe” (mijn vader) wil ik heel erg bedanken voor alle steun. Jullie begrepen mijn problemen niet altijd, maar jullie steun was onvoorwaardelijk. De Westlandse mentaliteit die jullie mij hebben meegegeven, heeft mij zeker geholpen in het voltooien van dit proefschrift. Daarnaast wil ik ook mijn broertje (Davey) en zusje (Jessie) bedanken. Jullie zijn beiden heel anders, maar ook jullie steun was onvoorwaardelijk. En Jessie, zie dit niet als een volgend doel! Oma, ik had gehoopt dat Opa dit ook mee had kunnen maken. Ik prijs mij gelukkig met deze sterke familieband.

Karina, zonder jou had dit proefschrift er niet geweest. De diepe dalen waren samen met jou toch iets minder diep en zelfs een “intelligente” lockdown was samen met jou een fijne ervaring. Ik kan met woorden niet omschrijven hoe veel steun en liefde je mij hebt gegeven over de afgelopen periode.

Mike van Meerkerk
Delft, June 2021

CURRICULUM VITAE

Mike van Meerkerk

28-10-1991 Born in The Hague, The Netherlands.

EDUCATION

2004-2010 **Secondary education**
VWO, Interconfessionele Scholengroep Westland (ISW), 's-Gravenzande, The Netherlands

2010-2013 **Bachelor Mechanical Engineering**
Delft University of Technology, Delft, The Netherlands

2013-2016 **Master Mechanical Engineering**
Delft University of Technology, Delft, The Netherlands

Thesis: *Droplet behaviour in a cavity mixing-layer*

2016-2020 **PhD-researcher**
Delft University of Technology, Delft, The Netherlands

Thesis: *Variability in wave impacts*

Promotor: Prof. dr. ir. J. Westerweel

Promotor: Prof. dr. ir. C. Poelma

2020-2021 **Hydraulic engineer**
Royal HaskoningDHV, Rotterdam, The Netherlands

2021- present **Advisor/researcher**
Deltares, Delft, The Netherlands

LIST OF PUBLICATIONS

JOURNAL PUBLICATIONS

M. van Meerkerk, C. Poelma, and J. Westerweel, "Scanning stereo-PLIF method for free surface measurements in large 3D domains" *Exp. Fluids*, vol. 61:19, 2020.

M. van Meerkerk, C. Poelma, B. Hofland, and J. Westerweel, "Experimental investigation of wave tip variability of impacting waves" *Phys. Fluids*, 32, 082110, 2020.

M. van Meerkerk, C. Poelma, B. Hofland, and J. Westerweel, "Gas flow dynamics over a plunging breaking wave prior to impact on a vertical wall" (*Submitted to European Journal of Mechanics - B/Fluids*).

CONFERENCE PUBLICATIONS AND CONTRIBUTIONS

M. van Meerkerk, C. Poelma, and J. Westerweel, "Non-intrusive measurement of complex free surfaces using Laser Induced Fluorescence and stereo imaging" *19th International Symposium on Applications of Laser and Imaging Techniques to Fluid Mechanics*, 16-19 July 2018, Lisbon, Portugal.

G. M. Rotte, **M. van Meerkerk**, V. Hengelmolen, M. Nikolaidou, and T. J. C. van Terwisga, "An experimental study on the physics of internal air cavity flows" (*Submitted to Ocean Engineering*)

M. van Meerkerk, C. Poelma, B. Hofland, and J. Westerweel, "Variability in wave impact: simultaneous free-surface and air flow measurements" (*Submitted to the 13th European Fluid Mechanics Conference*).

